Multiscale Modeling of Fracture in Polycrystalline Materials

by

Shang Sun

A dissertation submitted in partial fulfillment
of the requirements for the degree of
Doctoral of Philosophy
(Naval Architecture and Marine Engineering)
in the University of Michigan
2014

Doctoral Committee:

Associate Professor Veera Sundararaghavan, Co-Chair
Assistant Professor Matthew Collette, Co-chair
Professor John Allison
Professor Nick Vlahopoulos

ACKNOWLEDGEMENTS

I would like to express the deepest appreciation to my advisor, Professor Veera Sundararaghavan, who has the attitude and the substance of a genius. He continually and convincingly conveyed a spirit of innovation and exploration in regard to research. His working style is insightful and inspirational. Without his guidance and persistent help this dissertation would not have been possible.

I would like to thank my committee members, Professor Matthew Collette, Professor John Allison and Professor Nick Vlahopoulos for their help and advice.

It is imperative that I thank my wife, Hui Wang, who consistently stimulates and accompanies me on the road of academic adventure. It would not be as much fun and enjoyment in my five years of PhD life without her. I also must thank my whole family for their encouragement and support during my whole life.

Financial support was provided by Office of Naval Research (ONR) grant N00014-12-1-0013, National Science Foundation CAREER award (CMMI-0954390) and fellowship from Naval Architecture and Marine Engineering department.

TABLE OF CONTENTS

LIST OF FIGURES

Figure

LIST OF APPENDICES

Appendix

ABSTRACT

Multiscale Modeling of Fracture in Polycrystalline Materials

by

Shang Sun

Committee: Associate Professor Veera Sundararagahavan, Co-Chair

Assistant Professor Matthew Collette, Co-Chair

Professor John Allison

Professor Nick Vlahopoulos

Efficient multi–scale modeling tools are needed to model microstructure–dependent properties of advanced structural alloys used in aerospace, naval and automotive applications. Crystal plasticity finite element (CPFE) method has emerged as an effective tool for simulating the stress–strain response of aggregates of metallic crystals (the microstructure). However, a macro-scale component such as turbine disk contains millions of grains and resolving macro-scale components using microstructure–level grids is a challenging task even when using current state-of-the-art supercomputers. Of specific interest in the proposed work is the ability to link microstructural codes with macro-scale simulations using novel and computationally efficient multi-scaling techniques.

In this context, a new statistical theory is proposed that takes into account the coupling between grain size, shape and crystallographic texture using probability

functions. The probability function developed in this work, termed "grain size orientation distribution function" (GSODF), encodes the probability density of finding a grain size D along a direction (given by unit vector $\boldsymbol{n}$) in grains with orientation g. The prediction of texture and strains achieved by the statistical approach is verified by comparing against the CPFE approach. The approach is found to be two orders of magnitude faster than CPFE, which allows larger metallic components simulation. Then, a concurrent multiscaling model is pursued with fine meshes are employed to resolve the individual crystals crystals in micro-scale regions where critical features such as stress concentrations dominate. At larger size meshes other than the critical region, statistical theories are employed to approximate the microstructure in terms of probability functions (Orientation density function (ODF)). The concurrent approach is significantly faster than current algorithms for multiscale analysis of localization and failure. The prediction of the concurrent multiscale model is verified with analytical elastic solutions for a wedge-opening load (WOL) specimen. The model is then enriched using the variational multiscale cohesive method for modeling aspects of crack propagation in polycrystalline alloys. Numerical results including mesh convergence, and crack paths for tensile and three point bending experiments are shown. Intergranular and transgranular cracks are successfully simulated with exceptional convergence and efficiency.

The final section of this thesis explores the application of an emerging simulation technique, peridynamics, for modeling discontinuities in polycrystalline microstructures. A state–based theory of peridynamics is used (Silling, 2007) where the forces in the bonds between particles are computed from stress tensors obtained from crystal plasticity. The stress tensor at a particle, in turn, is computed from strains by tracking the motion of surrounding particles. A quasi–static implementation of the theory is developed, hereafter termed 'peristatics'. The code employs an implicit iterative solution procedure similar to a non–linear finite element implementation. Peristatic

results are compared with crystal plasticity finite element (CPFE) analysis for the problem of plane strain compression of a planar polycrystal. The stress, strain field distribution and the texture formation predicted by CPFE and peristatics are found to compare well. One promising feature of peristatics is its ability to model fine shear bands that occur naturally in deforming polycrystalline aggregates. Simulations are used to study the origin and evolution of these shear bands as a function of strain and slip geometry. In the future, combination of peridynamics with statistical descriptors is anticipated for efficient modeling of failure at the macro–scale.

Publications:

S Sun, V Sundararaghavan, A Peristatic Implementation of Crystal Plasticity, International Journal of Solids and Structures, in review, 2014

S Sun, V Sundararaghavan, Modeling Crack Propagation in Polycrystalline Alloys using Variational Multiscale Cohesive Method, Computational Mechanics, in review, 2014

V. Sundararaghavan, S. Sun, Modeling Crack Propagation in Polycrystalline Alloys Using a Variational Multiscale Cohesive Method, 2nd World Congress on Integrated Computational Materials Engineering (Edited by M. Li et. al.), Wiley, New York, p. 225-230, 2013.

S Sun, V Sundararaghavan, A probabilistic crystal plasticity model for modeling grain shape effects based on slip geometry, Acta. Mater., 2012, 60(13-14), 5233-5244

CHAPTER I

Introduction

Efficient multiscale modeling tools are needed to model microstructure–dependent properties of advanced structural alloys used in aerospace, naval and automotive applications. Microstructural features such as texture, grain size and shape distribution play an important role in determining the engineering properties of such alloys. Crystal plasticity finite element (CPFE) method has emerged as an effective tool for simulating the mechanical response of aggregates of metallic crystals (the microstructure) ([3, 4, 5, 6, 7, 8]). In this approach, deformation mechanisms such as dislocation slip and twinning are modeled using constitutive laws based on state variables such as dislocation densities or slip system resistances along various slip systems. Reorientation of grains and evolution of the threshold stress along each slip system due to various hardening mechanisms (self-hardening, latent hardening etc.) are modeled. The grain-level stresses are averaged to obtain the mechanical response (stress-strain curve) and crystallographic texture is post-processed. While CPFE forms a viable approach for modeling a few hundred grains, a macroscale component such as turbine disk contains millions of grains and simulation of such 'macroscale' components is a challenging task even when using current state-of-the-art supercomputers.

Of specific interest in the thesis is to efficiently simulate evolution of microstructural features during macroscale simulations using a novel and computationally ef-

ficient, tightly coupled, multiscaling technique. A statistical approach is proposed here which is based on probabilistic description of microstructure and the method can be used to efficiently model the response of aggregates of several hundred grains. At the same time, crystals are individually resolved at critical regions (such as stress concentrations) where it is important to track the individual microstructural features. This hybrid multiscaling approach is expected to be significantly faster than current algorithms for multiscale analysis of failure and localization.

The use of probabilistic descriptors for modeling evolution of microstructure is an emerging area of research. In this approach, microstructural descriptors are updated rather than actual microstructure (as illustrated in Fig. 1.1 [1]). The simplest descriptor is the orientation distribution function ($\mathcal{A}(\boldsymbol{g})$), which represents crystals volume fractions in orientation space ($\boldsymbol{g}$). Under an applied deformation, ODF is evolved by using conservation laws [9]. Taylor assumption [10] is usually employed in ODF representation to give all crystals the same strain rate along their directions. Sundararaghavan et al. have recently developed higher order probability descriptors [1] that contains crystal neighborhood information that can be used in models to predict interactions between grains. Traditional crystal plasticity models [11, 12] were developed largely without a connection to grain size and shape effects. In the Chapter II, the ODF formulation has been enhanced to include grain size and shape effects.

Incorporation of grain size effect into constitutive models for single slip began with Armstrong (1962) [13] who modified the Hall–Petch equation to correspond to the flow stress on a slip system (the 'micro–Hall–Petch relation'). The interrelationship between grain size and texture was not considered until Weng (1983) [14] employed the mean grain size in the equation for slip system resistance through the micro–Hall–Petch relation. A significant body of work has incorporated grain–size effect within crystal plasticity simulations using either the micro–Hall–Petch relation [15, 16] or using gradient theories [17, 18, 19, 20]. However, these models have only considered

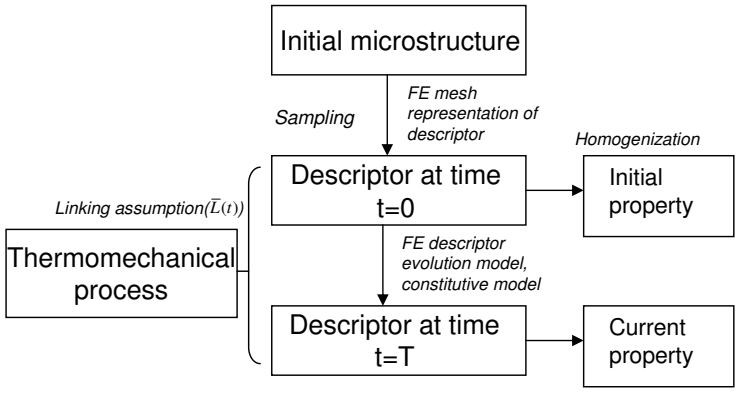

Figure 1.1: *Multiscale modeling using descriptors: The initial microstructure is sampled to obtain the descriptor which is then represented in a FE mesh. The descriptors are directly evolved during macroscale deformation simulations. [1]*

grain size effects in equiaxed grains and have not considered the effect of grain shape pertaining to non-equiaxed grains, high–aspect ratio grains and multimodal grain size distributions. Some attempts have been made in the past to consider the effect of grain shape on anisotropy in yield strength [21, 22, 23]. Bunge et al. (1985) [21] incorporated a micro–Hall–Petch relationship within the Taylor model [10] by modeling individual grains as ellipsoids and by computing the apparent grain size along each active slip direction. The change in shape of the grains during deformation was accounted for, but the work did not incorporate texture evolution. The recent model of Fromm et al. (2009) [24] coupled grain size distribution and texture within a viscoplastic model and found large yield stress anisotropy due to the coupling between grain size distribution and crystallographic texture. However, this study did not factor in the effect of grain shape, i.e., the effect of differences in apparent grain sizes along various slip directions in elongated grains and the evolution of the grain sizes during deformation (eg. flattening of grains during rolling processes). The new statistical modeling approach introduced in the Chapter II can be used to evolve the grain size and orientation distribution function (GSODF) during loading processes. GSODF is the combination of the idea of Bunge et al. (1985) [21] within the statistical model

of Fromm et. al. (2009) [24] in order to achieve a more complete coupling between grain orientation and grain size/shape effects into crystal plasticity. The aim is to develop an extremely efficient approach that can be used to perform simulations in a fraction of the time of a finite element or a Taylor aggregate model.

When failure and localization are considered, individual microstructural features need to be considered instead of statistical models. Examples include computation of stress concentrations at notches where failure is prone to happen or modeling indentation experiments wherein localized loads are applied. In Chapter III, a multiscale approach is proposed to combine the use of statistical approaches with explicit microstructure representation at critical regions with stress concentrations where localization is expected. As an illustrative example, we applied the multiscaling method to compute the stress intensity factor K_I around the crack tip in a wedge–opening load specimen [25]. The approach was verified with an analytical solution within linear elasticity and has been extended to allow modeling of crack tip plasticity. Then this framework was extended to allow modeling of arbitrary crack paths at critical regions within the multiscale approach in Chapter IV.

The prediction of fracture is of great importance in materials and engineering field [26]. The classic finite element cannot consistently capture the kinematics of cracks. Thus, cohesive zone models (CZM) [27] have been developed that are largely used to model crack kinematics and help avoid the ill-posed boundary value problem (BVP). The traction separation law contains the two most important parameters of the CZM, a fracture toughness (or energy) and a cohesive strength. Fracture energy is the energy dissipated during the crack formation. After the fracture energy is reached in the element, the crack is complectly formed. The cohesive strength defines a critical value for the nucleation of a crack. If the local stress state achieves the cohesive strength, the crack starts to grow. Both these parameters can be determined by experiments and thus can be used to predict crack nucleation and growth.

In recent years, cohesive interface models have emerged as attractive methods to numerically simulate fracture initiation and growth by the finite element method (Needleman, 1990, 1992 [28, 29]; Tvergaard et al., 1993, 1996 [30, 31]; William, 1989 [32]; Camocho et al., 1997 [27]; Xu and Needleman, 1994 [33]; Ortiz and Pandolfi, 1999 [34]; Zavattieri and Espinosa, 2001 [35]). Typically, a cohesive interface is introduced in a finite element discretization of the problem by the use of special interface elements, which obey a nonlinear interface traction separation constitutive relation. However, the crack paths are not known in advance and thus, these interface elements are practically needed at every element–to–element interface. This makes the problem both computationally expensive and also results in unsatisfactory mesh convergence properties. There are also other computational methods for capturing fracture in the past two decades by incorporating discontinues displacement, such as Embedded Elements (EFEM) [36] and Extended Finite Element Method (XFEM) [37]. For both methods, the discontinuous displacement in the element are represented by additional parameters in the normal displacement field. These parameters are called *enrichment*. The EFEM is the classified as element enrichment method and XFEM is the nodal enrichment method. Motivated by Remmers [38] et al. work, Song and Belytschko [39] have developed a method where cohesive segments are injected node-wise called the cracking node method. This is the nodal based cohesive method which means discontinuous displacements need to be transferred to the surrounding nodes. XFEM has not yet been extended to including crystal plasticity, and employs elastic or continuum plasticity models. In Chapter IV, the use of variational multiscale method (VMM) (Armero 1996,[40] Garikipati 1998, 2002 [41, 42]) is pursued to embed the cohesive elements selectively in critical regions. In this approach, the displacement discontinuities are represented over unstructured meshes using specially constructed element shape functions that are discontinuous. Rudraraju et al. [43, 44] recently employed variational multiscale cohesive method (VMCM) to study complex crack

geometries in composites and found excellent correlations to experiment. In Chapter IV, VMCM is applied to simulate crack propagation in the polycrystalline microstructure. Detailed computational results of VMCM approach are demonstrated for mesh convergence results and different loading cases, such as tension and three point bending tests. For homogeneous cases, mode I and mode II cracks was simulated. For polycrystalline material, intergranular and inter and transgranular cracks are given.

One particular drawback of standard finite element methods for crystal plasticity is observed during modeling of plastic localization zones. Such localization naturally occurs in deforming polycrystalline aggregates in the form of bands of intense strain (Harren et al. (1988) [45]). The strains in these bands have been recently measured using microscale digital image correlation (DIC) (eg. [2], see Fig. 1.2). In standard finite elements, the element size determines the size of strain localization (Anand and Kalidindi (1994) [46]). Various enhancements of finite element method have been studied in the past to address the issue of mesh dependency. Early approaches involved development of traction-separation softening laws whose slope was made to depend on the element size Oliver (1989) [47]. In the limiting case of zero element size, the localization appears as a sharp discontinuity. Later approaches such as the extended finite element methods (X-FEM, Samaniego and Belytschko (2005) [48]) or variational multiscale methods (VMM, Armero and Garikipati (1996)[40]) directly represented discontinuities on coarse elements by enriching the finite element interpolations using finescale strain functions .

Another approach employs models that possess an intrinsic characteristic length scale. Examples of these ideas are non-local constitutive models ([49, 50, 51, 52]), higher-gradient models ([53]) and more recently, peridynamic models ([54]). In peridynamics, the continuum domain is represented as a set of interacting particles. A state–based theory of peridynamics developed in [55] formulates the forces between particles based on stress tensors obtained from continuum formulations (eg. crystal

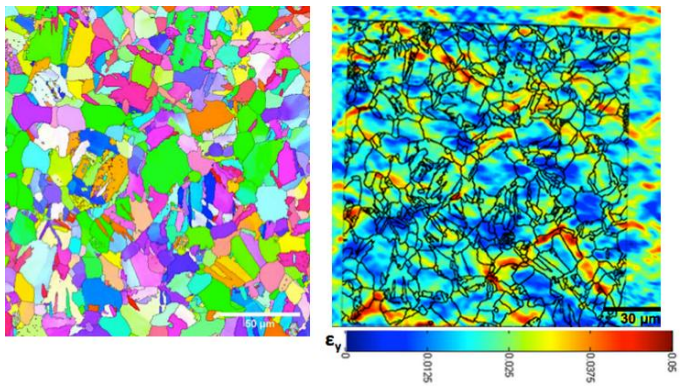

Figure 1.2: *Tensile strain field in a Titanium alloy microstructure as experimentally seen using microscale digital image correlation(Prof. S. Daly [2], personal communication). Strains are seen to localize into shear bands within select grains.*

plasticity). The stress tensor at a particle, in turn, is computed from strains calculated by tracking the motion of surrounding particles. Using an integral form of the linear momentum balance equation, the method can directly model sharp displacement discontinuities ([56]). Chapter V presents the first application of state–based peridynamic theory for crystal plasticity simulations. Current implementations of peridynamic state theory ([57]) employ explicit dynamic solution procedures that require small time steps for convergence. In Chapter V, a implicit quasi–static implementation of the theory is employed, hereafter termed 'peristatics'. Unlike peridynamics, peristatics does not include inertial terms and the solution procedure uses Newton–Raphson iterations similar to a non–linear finite element implementation. Thus, peristatic results can be quantitatively compared to conventional quasi–static crystal plasticity finite element simulations. The governing equations of the peristatic theory and peristatic results for shear band localization in a polycrystal in tension and shear modes were compared in Chapter 5.

Finally, in Chapter 6, conclusions of this work, challenges and future work are discussed.

CHAPTER II

Probabilistic Crystal Plasticity Model for Modeling Grain Shape Effects Based on Slip Geometry

[1]The GSODF, defined as $\mathcal{Q}(\boldsymbol{r}, \boldsymbol{g})$ in this chapter, gives the probability density of finding a grain of orientation $\boldsymbol{g}$ in the microstructure with a grain size $|\boldsymbol{r}|$ in the direction $\frac{\boldsymbol{r}}{|\boldsymbol{r}|}$. In previous work (Sundararaghavan and Kumar (2012) [1]), a finite element approach for representing and evolving microstructure probability density functions during deformation. Using this approach, the GSODF is described as a field variable over interconnected finite element meshes in the $\boldsymbol{r}$ space and $\boldsymbol{g}$ space (the fundamental region of crystal orientations). As the microstructure evolves, the crystallographic reorientations and shape changes of grains are captured by updating the GSODF field over these meshes. A total Lagrangian algorithm has been developed that allows evolution of probability densities while satisfying basic normalization and crystallographic symmetry constraints. For validation of the approach, the predictions of texture and strains achieved by the GSODF approach are compared to a Taylor aggregate model and a finite element model of a planar polycrystalline microstructure that uses the micro–Hall–Petch relationship. Finally, the use of adaptive GSODFs

[1]Reproduced from S. Sun and V. Sundararaghavan. "A probabilistic crystal plasticity model for modeling grain shape effects based on slip geometry", Acta Materialia. 2012. [58]

for determining the overall stress–strain response is investigated in the case of two–dimensional microstructures with bimodal grain size distributions. In contrast to aggregate models (CPFE), the simulation time for GSODF model is significantly smaller (two orders of magnitude faster for problems considered here) which makes multiscale simulations more practical.

2.1 Representation of the GSODF

The Grain size orientation distribution function (GSODF), $\mathcal{Q}(\boldsymbol{r}, \boldsymbol{g})$, gives the probability density of finding a grain of orientation $\boldsymbol{g}$ in the microstructure with a grain size $|\boldsymbol{r}|$ in the direction $\frac{\boldsymbol{r}}{|\boldsymbol{r}|}$. The descriptor inherently includes information about lower order descriptors such as (i) the orientation distribution function (ODF, $\mathcal{A}(g)$) which gives the probability density of finding an orientation $\boldsymbol{g}$ in the microstructure and (ii) the orientation–specific grain size distribution function (GSDF, $\mathcal{O}(\boldsymbol{r}|\boldsymbol{g})$) which gives the probability density of finding grain size $|\boldsymbol{r}|$ in the direction $\frac{\boldsymbol{r}}{|\boldsymbol{r}|}$ *given* that only grains with orientation $\boldsymbol{g}$ are sampled. This can be seen from the Bayesian relationship: $\mathcal{Q}(\boldsymbol{r}, \boldsymbol{g}) = \mathcal{O}(\boldsymbol{r}|\boldsymbol{g})\mathcal{A}(\boldsymbol{g})$. The GSODF satisfies the following conservation equations at all times during deformation:

$$\int \mathcal{O}(\boldsymbol{r}|\boldsymbol{g}) d\boldsymbol{r} = 1, \text{ (with } \mathcal{O}(\boldsymbol{r}|\boldsymbol{g}) \geq 0 \tag{2.1}$$

$$\int \mathcal{A}(\boldsymbol{g}) d\boldsymbol{g} = 1, \text{ (with } \mathcal{A}(\boldsymbol{g}) \geq 0 \tag{2.2}$$

where $d\boldsymbol{g}$ is a differential volume element (the invariant measure) of the orientation space. In addition to the above constraints, the orientation space corresponding to all possible $\boldsymbol{g}$'s must satisfy the crystallographic symmetries of the chosen system (face-centered cubic(fcc), hexagonal close-packed (hcp) etc.). The complete orientation space of a polycrystal can be reduced to a smaller subset, called the fundamental region, as a consequence of crystal symmetries. Within the fundamental region, each

crystal orientation is represented uniquely by the coordinate $\boldsymbol{g}$, the parametrization for the rotation (eg. Euler angles, Rodrigues vector etc.). The ODF ($\mathcal{A}(\boldsymbol{g})$) can be represented as a probability density function over the fundamental region of orientation space.

For simplicity, consider planar polycrystals characterized by a 2-D rotation $\boldsymbol{R}$ that relates the local crystal lattice frame to the reference sample frame. A parametrization of the associated rotation group is

$$\boldsymbol{R} = \boldsymbol{I}cos(g) - \boldsymbol{E}sin(g) \tag{2.3}$$

where g is the angle between the crystal and sample axes, $\boldsymbol{E}$ is the 2-D alternator ($E_{11} = E_{22} = 0, E_{12} = -E_{21} = 1$), and $\boldsymbol{I}$ is the identity tensor. A general planar crystal with symmetry under rotations through π is considered here. Under the symmetry, crystal orientations can be described uniquely by parameters drawn from a simply connected fundamental region $[a, a + \pi)$. For convenience, the choice of fundamental regions to the interval is restricted closest to the origin $(-\pi/2, \pi/2)$. Due to symmetry, the orientation $\pi/2$ is exactly the same as orientation $-\pi/2$. In this work, an FE mesh is used to model the fundamental region and the ODF is defined at the nodal points of this mesh [59, 60]. The probability values between nodal points are obtained as a result of interpolation using FE shape functions. The symmetry constraint on the ODF is enforced in practise by using periodic boundary conditions in the FE mesh wherein node at $g = \pi/2$ is considered a dependent node with field values updated using values at $g = -\pi/2$. The FE grid for the fundamental region will be referred to as $M(g)$. Note that other approaches based on spectral expansions [61, 62] of ODFs are also possible, although these are global representations (compared to FEs that have local basis functions that can efficiently capture sharp textures).

The orientation–specific grain size distribution function ($\mathcal{O}(\boldsymbol{r}|\boldsymbol{g})$) is also repre-

sented over a FE grid (named mesh $M(r|g)$). For a 2-D microstructure, the region $\boldsymbol{r}$ can be taken to be a semi–circle spanning sampling directions from $-\pi/2$ to $+\pi/2$. The radius of the semi–circle is taken to be equal to the maximum possible grain size sampled from the microstructure. The GSODF, $\mathcal{Q}(\boldsymbol{r}, \boldsymbol{g})$, is represented using meshes $M_{r|g}$ defined at every node point in another FE discretized fundamental region (mesh M_g). The approach is illustrated in Fig. 2.1 for a planar microstructure The GSDF $\mathcal{O}(\boldsymbol{r}|\boldsymbol{g})$ is described over mesh $M(r|g)$ and the ODF $\mathcal{A}(\boldsymbol{g})$ is described over mesh $M(g)$. From this representation, GSODF can be retrieved using the Bayesian relationship: $\mathcal{Q}(\boldsymbol{r}, \boldsymbol{g}) = \mathcal{O}(\boldsymbol{r}|\boldsymbol{g})\mathcal{A}(\boldsymbol{g})$. Grain size distribution can be assessed based on ASTM grain size standard E–112 using the Heyn intercept method [63]. In this method, parallel lines at different orientation angles are superposed over the microstructure. The histogram of the intercept length distribution, i.e. intercept length vs. number of test lines possessing the intercept length, is normalized to obtain the grain size distribution function (see Fig. 2.4, Section 2.5).

2.2 Probability update in FE spaces

The probabilities are evolved from time $t = 0$ from an initial GSODF that satisfies the conservation equations Eqs. 2.1–2.2 using a Lagrangian FE approach [1, 9]. The initial orientation $\boldsymbol{g}_o$ of a crystal reorients during deformation and maps to a new orientation $\boldsymbol{g}_t$ at time t. Simultaneously, the FE mesh of fundamental region M_g deforms with nodes located at $\boldsymbol{g}_o$ moving to new locations $\boldsymbol{g}_t$. It is assumed that the mapping from $\boldsymbol{g}_o$ to $\boldsymbol{g}_t$ is invertible.

The ODF $\mathcal{A}(\boldsymbol{g}_t)$ represents the probability density of crystals with orientation $\boldsymbol{g}_t$ at time t. The evolution of ODF is given by the conservation equation 2.2 as:

$$\int \mathcal{A}(\boldsymbol{g}_o, t = 0) d\boldsymbol{g}_o = \int \mathcal{A}(\boldsymbol{g}_t) d\boldsymbol{g}_t = 1 \tag{2.4}$$

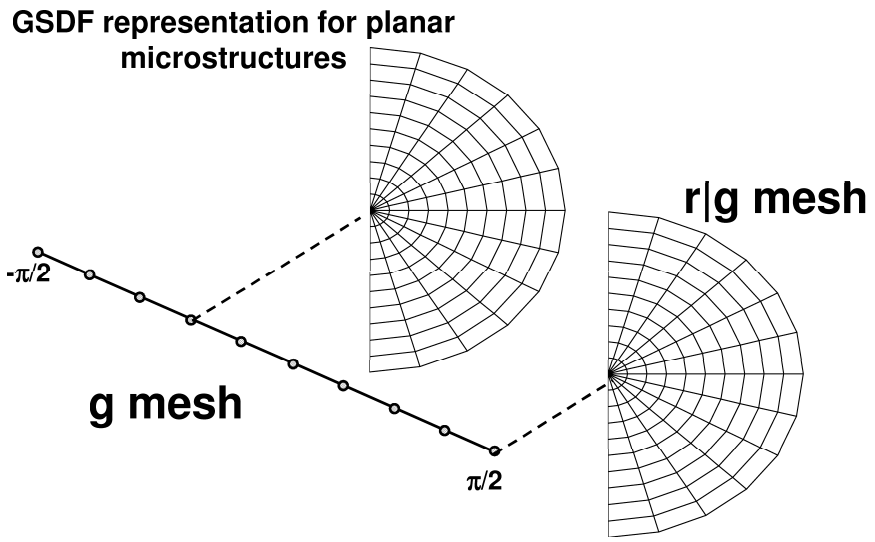

Figure 2.1: *The GSODF, $\mathcal{Q}(\boldsymbol{r},\boldsymbol{g})$, is represented in the mesh structure shown here. The semi–circle mesh $M_{r|g}$ is defined for every node point in another FE discretized fundamental region (mesh M_g). The approach is illustrated for a planar microstructure (with fundamental region mesh M_g being a line between $-\pi/2$ to $\pi/2$). The GSDF $\mathcal{O}(\boldsymbol{r}|\boldsymbol{g})$ is described over mesh $M(r|g)$ and the ODF $\mathcal{A}(\boldsymbol{g})$ is described over mesh $M(g)$.*

where $d\boldsymbol{g}_o$ represents the volume element in the undeformed (initial) ODF mesh (M_{g_o}), which becomes volume element $d\boldsymbol{g}_t$ at time t. A Jacobian $J(\boldsymbol{g}_o,t) = \det(\boldsymbol{W})$ gives the ratio of elemental volumes such that $d\boldsymbol{g}_t = J(\boldsymbol{g}_o,t))d\boldsymbol{g}_o$, where $\boldsymbol{U}$ is the reorientation gradient given as $\boldsymbol{U}(\boldsymbol{g}_o,t) = \frac{\partial \boldsymbol{g}_t}{\partial \boldsymbol{g}_o}$. Using the Jacobian, a map of the current mesh (at time t) to the reference mesh (at $t=0$) can be made:

$$\int (\mathcal{A}(\boldsymbol{g}_o,t=0) - \hat{\mathcal{A}}(\boldsymbol{g}_o,t)J(\boldsymbol{g}_o,t))d\boldsymbol{g}_o = 0 \tag{2.5}$$

The quantity written as $\hat{\mathcal{A}}(\boldsymbol{g}_o,t)$ is the volume density $\mathcal{A}(\boldsymbol{g}_t)$ plotted over the corresponding orientation ($\boldsymbol{g}_o$) in the initial mesh. Thus, $\hat{\mathcal{A}}(\boldsymbol{g}_o,t)$ gives the Lagrangian representation of the current ODF in the initial mesh M_{g_o}. If the integrand is continuous, a localized relationship of the following form can be used to update the ODF

at any time t:

$$\hat{\mathcal{A}}(\boldsymbol{g}_o, t) J(\boldsymbol{g}_o, t) = \mathcal{A}(\boldsymbol{g}_o, t = 0) \tag{2.6}$$

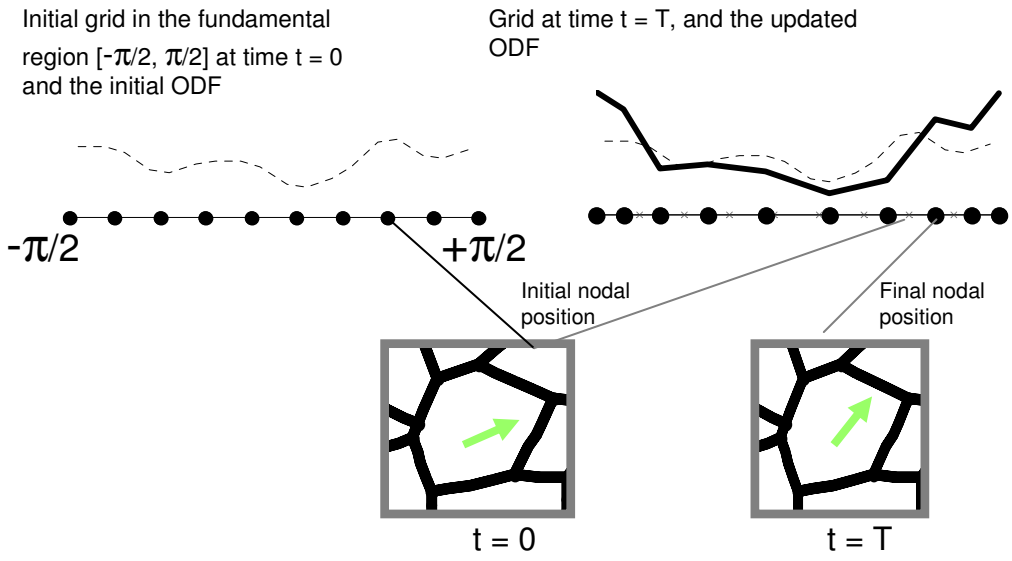

Figure 2.2: *Probability update scheme in FE space: During deformation, the nodal points ($\boldsymbol{g}$) of the FE mesh are moved to reflect reorientation ($\Delta\boldsymbol{g}$) of crystals. The new ODF is obtained using Eq. 2.6 that ensures that the normalization constraint (Eq. 2.4) is met in the reoriented mesh.*

Fig. 2.2 gives an idea of how the approach works for a 1–D fundamental region that is represented using two–noded FEs with linear interpolation. Here, the Jacobian is simply the ratio of element lengths, i.e. current length divided by the initial length. If the element length decreases over time, the probability density has to increase based on Eq. 2.6 to maintain normalization of the ODF. Note that the integrand in Eq. 2.5 needs to be continuous for the localization relationship to be valid. Thus, it is implied that $J(\boldsymbol{g}_o, t)$ needs to be continuous. For computer $J(\boldsymbol{g}_o, t))$, a reorientation velocity $\boldsymbol{v} = \frac{\partial \boldsymbol{g}_t}{\partial \boldsymbol{g}_o}$ is calculated from the elasto-plastic constitutive model (described in section 2.3). Consequently, $\boldsymbol{v}$ needs to be continuously differentiable (at least piecewise) in the fundamental region. This is a restriction on the constitutive model. Note that the differentiability of $\boldsymbol{v}$ will also ensure invertibility of the map from $\boldsymbol{g}_o$ to $\boldsymbol{g}_t$.

A similar approach is used to update the probability densities $\mathcal{O}$ in the meshes

$M_{r|g}$. The evolution of geometrical probability density $\mathcal{O}$ is given by conservation equation 2.2 as:

$$\int (\hat{\mathcal{O}}(\boldsymbol{r}_o, t|\boldsymbol{g}) J(\boldsymbol{r}_o, t|\boldsymbol{g}) - \mathcal{O}(\boldsymbol{r}_o, t=0|\boldsymbol{g})) d\boldsymbol{r}_{o_g} = 0 \tag{2.7}$$

where $d\boldsymbol{r}_{o_g}$ represents the volume element in the undeformed (initial) mesh ($M_{r|g}$) and $J(\boldsymbol{r}_o, t|\boldsymbol{g}) = \det(\frac{\partial \boldsymbol{r}_t}{\partial \boldsymbol{r}_o}(\boldsymbol{g}))$ is the Jacobian for a volume element initially at location $\boldsymbol{r}_o$ from orientation $\boldsymbol{g}$. A localized relation of the following form is used to compute the geometrical probability density at time t:

$$\hat{\mathcal{O}}(\boldsymbol{r}_o, t|\boldsymbol{g}) J(\boldsymbol{r}_o, t|\boldsymbol{g}) = \mathcal{O}(\boldsymbol{r}_o, t=0|\boldsymbol{g}) \tag{2.8}$$

2.3 Crystal plasticity constitutive model

Classical single-crystal plasticity theory [64] is used to model the deformation within each grain. The theory is based on the notion that plastic flow takes place through slip on prescribed slip systems. For a material with $\alpha = 1, \ldots, N$ slip systems defined by ortho-normal vector pairs ($\boldsymbol{m}_0^\alpha$,$\boldsymbol{n}_0^\alpha$) denoting the slip direction and slip plane normal respectively at time $t = 0$, the constitutive equations relate the following basic fields (all quantities expressed in crystal lattice coordinate frame): the deformation gradient defined with respect to the initial undeformed crystal $\boldsymbol{F}$ which can be decomposed into elastic and plastic parts as $\boldsymbol{F} = \boldsymbol{F}^e \ \boldsymbol{F}^p$ (with $\det(\boldsymbol{F}^p) = 1$), the Cauchy stress $\boldsymbol{\sigma}$ and the slip resistances $s^\alpha > 0$. In the constitutive equations to be defined below, the Green elastic strain measure $\bar{\boldsymbol{E}}^e = \frac{1}{2}\left(\boldsymbol{F}^{eT}\boldsymbol{F}^e - \boldsymbol{I}\right)$ defined on the relaxed configuration (plastically deformed, unstressed configuration) is utilized. The conjugate stress measure is then defined as $\bar{\boldsymbol{T}} = \det\boldsymbol{F}^e(\boldsymbol{F}^e)^{-1}\boldsymbol{\sigma}(\boldsymbol{F}^e)^{-T}$. Kinematics of single crystal slip is illustrated in Fig. 2.3.

The constitutive relation, for stress, is given by $\bar{\boldsymbol{T}} = \boldsymbol{\mathcal{C}}^e\left[\bar{\boldsymbol{E}}^e\right]$ where $\boldsymbol{\mathcal{C}}^e$ is the

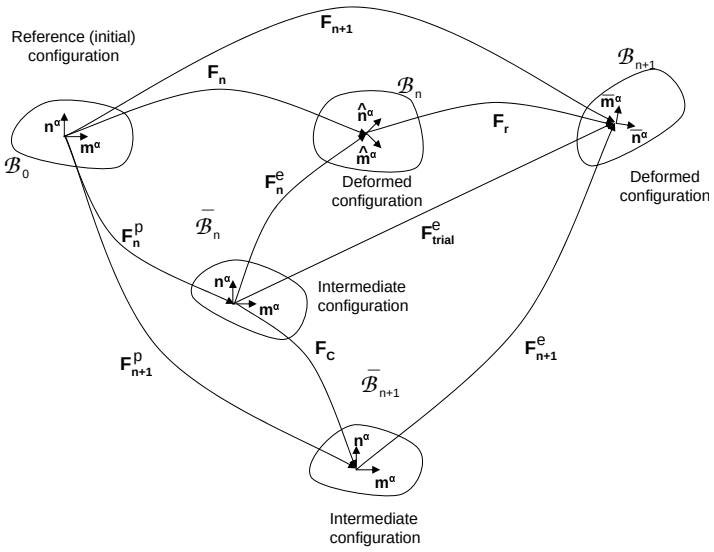

Figure 2.3: *Schematic of the various material configurations, for a single crystal, used in the integration of the constitutive model. The slip systems* $(\boldsymbol{m}^\alpha, \boldsymbol{n}^\alpha$ *are known on the reference (initial) configuration. Also,* $\hat{\boldsymbol{m}}^\alpha$, $\bar{\boldsymbol{m}}^\alpha$ *are the slip directions (different from* $\boldsymbol{m}^\alpha$ *because of crystal re-orientation) in the deformed configurations* $\mathcal{B}_n$ *and* $\mathcal{B}_{n+1}$*, respectively.*

fourth-order anisotropic elasticity tensor. It is assumed that deformation takes place through dislocation glide and the evolution of the plastic velocity gradient is given by:

$$\boldsymbol{L}^p = \dot{\boldsymbol{F}}^p (\boldsymbol{F}^p)^{-1} \;=\; \sum_\alpha \dot{\gamma}^\alpha \boldsymbol{S}_0^\alpha sign(\tau^\alpha) \tag{2.9}$$

where $\boldsymbol{S}_0^\alpha \;=\; \boldsymbol{m}_0^\alpha \otimes \boldsymbol{n}_0^\alpha$ is the Schmid tensor and $\dot{\gamma}^\alpha$ is the plastic shearing rate on the α^{th} slip system. The resolved stress on the α^{th} slip system is given by $\tau^\alpha = \bar{\boldsymbol{T}} \cdot \boldsymbol{S}_0^\alpha$.

A rate independent algorithm is employed to solve the single crystal model. The resolved shear stress τ^α is taken to attain a critical value s^α (the slip system resistance) on the systems where slip occurs. These active systems have a plastic shearing rate $\dot{\gamma}^\alpha > 0$. There is no plastic shearing rate ($\dot{\gamma}^\alpha = 0$) on inactive slip systems where the resolved shear stress does not exceed s^α. The evolution of slip system resistance

given by the following expression [14]:

$$\dot{s}^{\alpha}(t) = \sum_{\beta} h^{\alpha\beta}\dot{\gamma}^{\beta}(t), \text{ with } s^{\alpha}(0) = (\tau_0^{\alpha} + \frac{k_0^{\alpha}}{\sqrt{\langle D^{\alpha}(0)\rangle}}) \tag{2.10}$$

$$\text{where, } h^{\alpha\beta} = (h_o^{\beta} + \frac{k_1^{\beta}}{\sqrt{\langle D^{\beta}(t)\rangle}})(q + (1-q)\delta^{\alpha\beta})(1 - \frac{s^{\beta}(t)}{s_s^{\beta}})^{a} \text{ (no sum on } \beta) \tag{2.11}$$

Here, τ_0^{α} corresponds to the flow stress of slip system α of an infinitely large grain with zero plastic strain ($\gamma^{\alpha} = 0$) and k_0^{α} is the Hall–Petch constant of slip system α at zero plastic strain. The slip system hardening term ($h^{\alpha\beta}$) includes latent hardening through parameter q. In this term, h_o^{β} is the hardening coefficient of slip system β in an infinitely large grain, the constant k_1^{β} captures the dependence of the Hall–Petch coefficient on the plastic strain of slip system β and s_s^{β} is the saturation resistance of slip system β. Note that $\langle D^{\beta}(t)\rangle$ in Eq. 2.11 is the average grain size measured along slip direction of β^{th} slip system in the relaxed configuration (plastically deformed, unstressed configuration) at time t.

The algorithm for computing the plastic shear increment $\Delta\gamma^{\beta}$ from this model be found in the appendix A. Subsequently, the plastic part of the deformation gradient is updated using Eq. (2.9), the elastic part computed from $\boldsymbol{F} = \boldsymbol{F}^{e}\ \boldsymbol{F}^{p}$. The conjugate stress measure, $\bar{\boldsymbol{T}}$ is then computed from $\bar{\boldsymbol{T}} = \boldsymbol{\mathcal{C}}^{e}\left[\bar{\boldsymbol{E}}^{e}\right]$ and converted to Cauchy stress and the Piola-Kirchhoff-I stress, $\boldsymbol{P} = (\det\boldsymbol{F})\boldsymbol{\sigma}\boldsymbol{F}^{-T}$ for further use. The slip resistances are also updated at the end of the time step using Eq. 2.10. Finally, the tangent modulus $\frac{\partial\boldsymbol{\sigma}}{\partial\boldsymbol{F}}$ for use in the weak form is computed using a fully implicit algorithm described in appendix B.

2.4 Computation of Jacobians

At time t during deformation, the new positions ($\boldsymbol{g}_t$) of nodes in the fundamental region mesh ($M(g)$) are computed using the reorientation velocities $\boldsymbol{v}$ obtained from

the constitutive model. The expression for $\boldsymbol{v}$ is obtained by taking a derivative of relation Eq. 5.10:

$$\boldsymbol{v} = \frac{1}{2} E.\Omega \tag{2.12}$$

where $\boldsymbol{\Omega}$ is the spin tensor defined as $\boldsymbol{\Omega} = \dot{\boldsymbol{R}}^e \boldsymbol{R}^{eT}$. Here, $\boldsymbol{R}^e$ is evaluated through the polar decomposition of the elastic deformation gradient $\boldsymbol{F}^e$ as $\boldsymbol{F}^e = \boldsymbol{R}^e \boldsymbol{U}^e$. The reorientation velocity $\boldsymbol{v} = \frac{\partial \boldsymbol{g}_t}{\partial t}$ is computed at each nodal point in the mesh and the change in orientation $\Delta \boldsymbol{g}^{'} = \boldsymbol{g}_t^{'} - \boldsymbol{g}_o^{'}$ is then calculated and stored at the nodal points in the fundamental region. The Jacobian $J(\boldsymbol{g}_o, t) = \det(\frac{\partial \boldsymbol{g}_t}{\partial \boldsymbol{g}_o})$ is then calculated using FE shape functions as:

$$J(\boldsymbol{g}_o, t) = \det(\frac{\partial \boldsymbol{g}_t}{\partial \boldsymbol{g}_o}) \tag{2.13}$$

In order to retrieve the average grain sizes $\langle D^\alpha(t) \rangle$ at time t for use in Eq.2.11, the evolution of GSDF ($\mathcal{O}(\boldsymbol{r}|\boldsymbol{g})$) can be computed using the plastic deformation gradient $\boldsymbol{r}_t = \boldsymbol{F}^p(\boldsymbol{g}, t)\boldsymbol{r}_o$. However, the Jacobian in this case is simply equal to one ($J(\boldsymbol{r}_o, t|\boldsymbol{g}) = \det(\boldsymbol{F}^p(\boldsymbol{g}, t)) = 1$) and from Eq. 2.8, the probability distribution remains unchanged on the nodal locations during deformation. The slip direction $\boldsymbol{m}_o^\alpha$ in the deformed mesh relates to the direction $\boldsymbol{m}^*$ in the undeformed mesh through the equation:

$$\boldsymbol{m}^* = \boldsymbol{F}^{p^{-1}} \boldsymbol{m}_o^\alpha \tag{2.14}$$

Since the probabilities along $\boldsymbol{m}^*$ in the undeformed mesh are same as those along $\boldsymbol{m}_o^\alpha$ in the deformed mesh, the average grain size at time t can be retrieved directly using the formula:

$$\langle D^{\boldsymbol{m}_o^\alpha}(t) \rangle = \langle D^{\boldsymbol{m}^*}(0) \rangle / |\boldsymbol{m}^*| \tag{2.15}$$

where $|\boldsymbol{m}^*|$ is the Euclidean norm of $\boldsymbol{m}^*$(the stretch factor). Hence, only the average grain sizes along all possible directions (e.g. along a unit circle in 2D) at time t=0 ($\langle D^{\boldsymbol{m}^*}(0) \rangle$)is needed for the update procedure. In other words, the probabilities

$\mathcal{O}(\boldsymbol{r}|\boldsymbol{g})$ over mesh $M(r|g)$ need not be evolved with time. This significantly enhances the computational efficiency of the algorithm.

The average stress for the microstructure is obtained by averaging the single crystal stresses $\boldsymbol{\sigma}$ over the ODF as follows:

$$< \boldsymbol{\sigma} >= \int \hat{\boldsymbol{\sigma}}(\boldsymbol{g}_t)\mathcal{A}(\boldsymbol{g}_t)d\boldsymbol{g}_t = \int \hat{\boldsymbol{\sigma}}(\boldsymbol{g}_o, t)\mathcal{A}(\boldsymbol{g}_o, t=0)d\boldsymbol{g}_o \tag{2.16}$$

where, $\hat{\boldsymbol{\sigma}}(\boldsymbol{g}_o, t)$ is the stress ($\boldsymbol{\sigma}(\boldsymbol{g}_t) = \boldsymbol{\sigma}(\boldsymbol{g}_o + \Delta\boldsymbol{g})$) plotted over the corresponding orientation ($\boldsymbol{g}_o$) in the initial ODF mesh. From this equation, one can conclude that, if the reorientations ($\Delta\boldsymbol{g}$) and the initial texture ($\mathcal{A}(\boldsymbol{g}_o, t = 0)$) are known, then the average stress (or any other average property) for the polycrystal can be evaluated. A total lagrangian approach is used where the fundamental region mesh for $\boldsymbol{g}$ remain unchanged and the reorientations are stored at the nodal points. If the reorientations are used to move the nodal locations of the ODF grid, new orientation spaces are obtained, which are also valid fundamental regions. Several ideas from the finite element community are used to solve the GSODF evolution problem. For example, linear shape functions are used to interpolate the probabilities and calculate the Jacobians. Integrations are performed using gauss points to compute integrals (Such as Eq. 2.16), interpolations are performed using shape functions to transfer reorientations from nodes to integration points, smoothing is performed to transfer the computed jacobians from integration points to nodes. The overall algorithm for the GSODF update is given in Table 2.1.

2.5 Numerical examples

The deformation response predicted by the GSODF–based method has been quantified through deformation analysis of a planar polycrystalline microstructure. A specific crystal geometry with two slip systems at orientation $-\pi/6$ and $+\pi/6$ is

Table 2.1: Algorithm for GSODF evolution

(1) Initialize mesh M_g and load probabilities $\mathcal{A}(g)$ and average grain sizes as a function of sampling angle $\langle D^{\alpha)}(\boldsymbol{g}, t=0)\rangle$ computed from the sampling algorithm. Read in the macroscopic velocity gradient $\boldsymbol{L}$.
(2) Apply time increment Δt and compute the current deformation gradient $\boldsymbol{F}$(at $t=0$, $\boldsymbol{F}=\boldsymbol{F}^e=\boldsymbol{F}^p=\boldsymbol{I}$, where $\boldsymbol{I}$ is the identity tensor).
(3) Update Probabilities:
(3.1) Compute the stretch along the slip directions using Eq 2.14.
(3.2) Compute and store $\langle D^{\boldsymbol{m}_o^\alpha}(t)\rangle$ using Eq. 2.15.
(3.3) Call constitutive model to compute stresses and reorientation velocities at nodes in the fundamental region.
(3.4) Compute the Jacobians using Eq. 2.13 and update ODF using Eq. 2.6.
(3.5) Compute average stress using Eq. 2.16.
(4) Go to step (2) if time $t < t_{final}$.

considered. This model leads to continuity in both reorientation velocity (v) and its gradient (∇v) over the orientation space as demonstrated in [60]. The imposed macroscopic velocity gradient $\boldsymbol{L}$ is given as:

$$\boldsymbol{L} = \eta \begin{bmatrix} 1 & 0 \\ 0 & -1 \end{bmatrix} \tag{2.17}$$

Here η is a constant strain rate taken to be 0.01 for tensile and -0.01 for compressive loading. The elastic constants are taken to be $\mathcal{C}_{11} = 2\ GPa$ and $\mathcal{C}_{12} = \mathcal{C}_{44} = 1\ Gpa$. The parameters in the hardening law are taken to be as follows: $\tau_0^\alpha = 10$ MPa, $k_0^\alpha = 30$ MPa$\sqrt{mm}$, $h_o^\alpha = 10$ MPa, $k_1^\alpha = 10$ MPa$\sqrt{mm}$, $s_s^\alpha = 200$ MPa, $q = 1.4$ and $a = 2$.

The GSODF of a given microstructure is obtained by sampling it using 200 lines each at 50 different angles from -90 to $+90$ degrees. The grain size histogram, for one grain along a particular sampling direction, is obtained by measuring the intercept lengths ($\boldsymbol{r}$, as illustrated in Fig.2.4). Histograms for grains that have orientations close to the nodal points in the M_g mesh (within an error of $\pm\delta\boldsymbol{g}$, $\delta\boldsymbol{g} = 0.2$ rad

being a smoothing parameter) are used for computing the GSODF. The GSODF probabilities are then computed by normalizing the measured histograms.

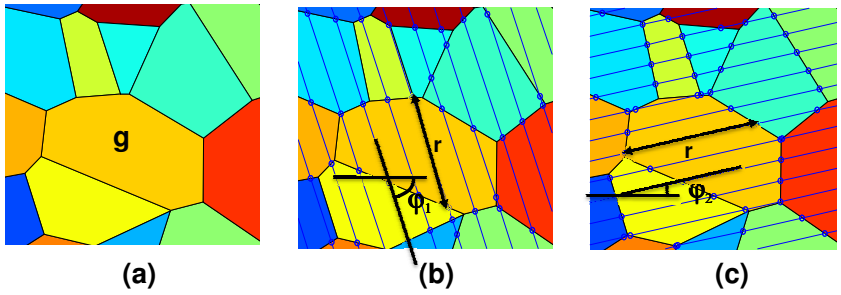

Figure 2.4: *Illustration of the sampling approach for GSODF: (a) For every grain orientation* $\boldsymbol{g}$*, the grain sizes are measured by sampling lines along various angles as shown in (b) and (c).*

The stress–strain response and texture evolution predicted by the GSODF algorithm in Table 2.1 is compared against two different approaches. In the first approach, called the 'Taylor aggregate model', each grain is imposed with the same macroscopic deformation gradient and the stresses and reorientations are tracked within each individual grain. In the second model, the crystal plasticity finite element ('CPFE') model, the deformation gradient is enforced on the external boundaries and intragranular strains are computed through finite element analysis [8]). In the Taylor aggregate and CPFE model, the GSDF is separately sampled for every individual grain while the average grain sizes are evolved in a way similar to the GSODF model (using Eqs. 2.14 and Eq. 2.15). Note that in the CPFE model, each grain has an inhomogeneous distribution of plastic strains and thus, an grain-averaged plastic deformation gradient is computed for use in Eq. 2.14.

In the GSODF model, the GSDF is computed for each orientation (rather than for each individual grain as in the Taylor aggregate or CPFE models). In other words, two grains of the same orientation but with different grain shapes will be represented using the same averaged grain size distribution function. In the case of microstructures with constant grain shapes/sizes, the GSODF model contains the

same information as the Taylor-Aggregate model. In this case, the GSODF algorithm must give the same stress–strain curve or texture evolution as the Taylor aggregate model. Thus, to test the algorithm, a representative volume element (RVE) of size $10 \times 10\ mm^2$ containing 81 equally sized square grains is considered (shown in Fig. 2.5(a)). The initial orientations are randomly assigned and the corresponding ODF is shown in Fig. 2.5(b). The initial ODF corresponds to a finite element grid with nine line elements (and 10 nodes) in the fundamental region $(-\pi/2, \pi/2)$. The GSDF corresponding to node 5 of the ODF mesh is also indicated. For a square grain, there is only one possible intercept length along the horizontal and vertical directions whereas a variety of intercept lengths are possible along other directions. Thus, the resulting GSDF in Fig. 2.5(c) shows a sharp peak at 0^o and $\pm 90^o$ angles at an intercept length of $1.11mm$ (which corresponds to the side–length of the square grain).

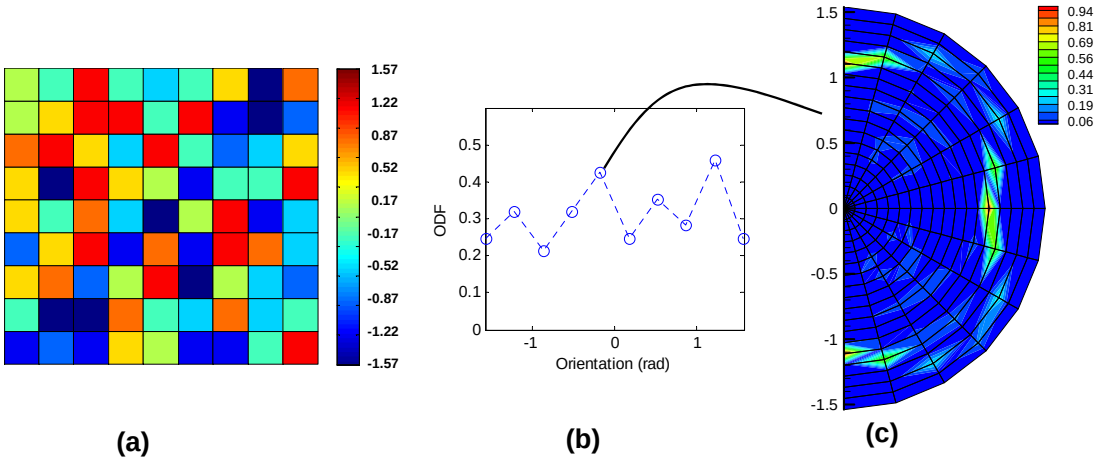

Figure 2.5: *(a) The initial microstructure with square grain shapes colored by grain orientation (b) The ODF (C) The GSDF at node* $\boldsymbol{g} = 0.1745$.

The stress–strain response predicted by the three methods for this microstructure are indicated in Fig. 2.6(a). The GSODF and the Taylor aggregate models give the same response as expected. The finite element approach (with each grain modeled as one four noded quadrilateral element) gives a softer response since it is less constrained than the Taylor model. The texture evolution for a grain initially oriented

at 70^o is also shown. The overall stress–strain response predicted by the GSODF and FEM approaches are directly compared in Fig. 2.6c and d and show good correlation. In the case of the GSODF model, the stress contour (in Fig. 2.6c) is obtained based on the stresses predicted for each grain orientation in the ODF mesh. Unlike GSODF model that assumes all grains have the same deformation gradient (Taylor model), the CPFE model explicitly takes into account equilibrium across grain boundaries and leads to inhomogeneity in the evolution of grain shapes as seen in Fig. 2.6d. In this example, a uniformly discretized fundamental region is sufficient to represent the smooth ODF. However, when one considers sharply textured specimens, non–uniform discretizations have to be used where node density is increased adaptively around dominant orientations in the microstructure. A L^2 norm error of the difference between the sampled probability distribution and finite element interpolated probability distribution (e.g. Ref. [65]) may be used as a convergence measure when adaptively meshing the probability spaces.

With the validity of the GSODF model established, we investigated three different microstructural effects related to GSDFs, (i) the effect of initial grain shape, (ii) the effect of initial grain size (Hall-Petch effect) and (iii) the effect of time evolution of grain shapes/sizes on the overall stress–strain response. The effect of initial grain shape is modeled by altering the aspect ratio of the square grains. The aspect ratio (L_x/L_y) is defined as the ratio of lengths (L_x, L_y) of individual grains in the x– and y– directions. The area of the grain itself is kept constant during the study, which ensures that the initial texture is the same for all the aspect ratios investigated. Fig. 2.7a reveals the relationship between yield stress and the logarithm of the grain aspect ratio. The predicted stress is minimum for square grains (aspect ratio of one) and increases as the grain aspect ratio changes following a parabolic relationship. The effect of grain size (Hall Petch effect) is shown in Fig. 2.7b. In this case, the grain size (L_x) of the square grains are increased while keeping the grain orientation (texture)

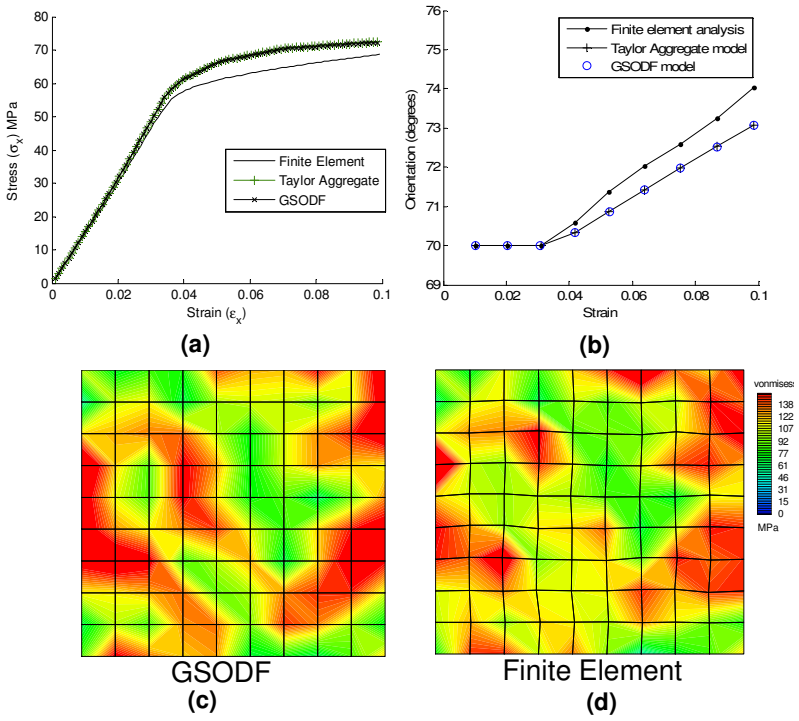

Figure 2.6: *(a) Comparison of stress–strain response for uniaxial tension predicted by the FE, Taylor aggregate and the GSODF model. (b) Evolution of crystal orientation predicted by GSODF and FE analysis (for a crystal initially oriented at 70^o) (c,d) Comparison of the Von Mises stress distribution predicted by the GSODF and finite element models.*

unchanged. The relationship of the logarithm of yield stress and the logarithm of grain size shows a slope close to -0.5 as expected from the Hall–Petch relationship.

The results in Fig. 2.8 indicates the important role of initial grain size and shape on the stress–strain response. In addition to the effect of initial grain size and shape, the effect of change in grain size and shape during loading is also investigated. In the first case, the evolution of the GSDF during deformation is switched off. This ensures that the Eq. 2.11 only uses the initial grain size to predict the stresses during loading. In the second case, GSDF evolution is included and the updated grain size computed at each timestep is employed in Eq. 2.11. The stress–strain response from the two cases are shown in Fig. 2.8. The stress–strain response predicted using only the initial GSDF is softer than the one predicted when the GSDF evolved with time.

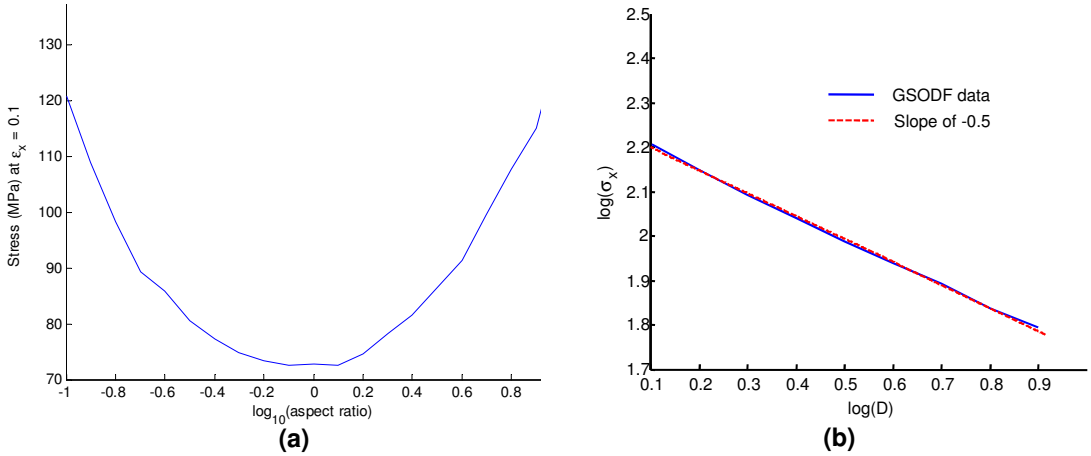

Figure 2.7: *(a) Variation of stress (σ_x) as a function of aspect ratio of grains (while keeping the ODF unchanged). (b) Variation of stress with grain size (Hall Petch relation) in logarithmic scale.*

However, the difference is less apparent at smaller strains and is significant only at larger strain levels. The GSDF at orientation $\boldsymbol{g} = 0.1745$ at $t = 0$ and the evolved GSDF at $t = 27$ sec are also shown in Fig. 2.8b and c respectively. The GSDF at $t = 27sec$ clearly shows the lengthening of grains along the x–direction during tensile loading.

The above studies using a square–grained microstructure indicate that the effects of both initial grain shape and grain size are quite important for crystal plasticity models. On the other hand, the evolution of GSDF itself does not significantly affect the initial yield stress but may become a consideration at large strain levels. As explained previously, the GSODF model includes grain size information for each orientation (rather than each individual grain as in the case of Taylor or CPFE models). This leads to significant loss of information when considering bimodal grain size distributions. Consider the microstructure shown in Fig. 2.9a that includes both high aspect ratio and low aspect ratio grains[2]. The overall GSDF for orientation $\boldsymbol{g} = 0.1745$ shown in Fig. 2.9b, averages out the contribution of the different grain

[2]The microstructure is generated using Voronoi tessellation [8]. Edges in the microstructure are not cropped to ensure that the GSDF line sampling is unbiased.

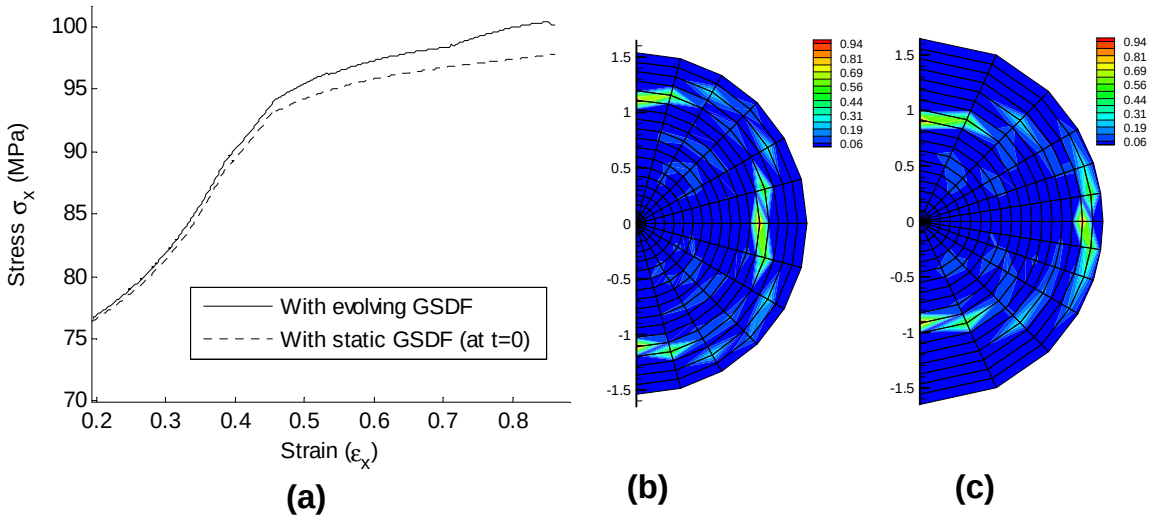

Figure 2.8: *(a) Comparison of stress–strain profile predicted by using only the initial GSDF and the one predicted when the GSDF is evolved with time. (b) The GSDF at orientation* $\boldsymbol{g} = 0.1745$ *at* $t = 0$*. (c) The evolved GSDF at* $t = 27$ *sec.*

shapes. In order to effectively model such microstructures, an adaptive approach is suggested where the overall GSODF is split into two different GSODFs, one for high aspect ratio grains and another for low aspect ratio grains. In Fig. 2.9c, the GSDF of only the high aspect ratio grains (with $L_{max}/L_{min} > 2.8$) is shown. The GSDF of low aspect ratio grains is shown in Fig. 2.9d. In the adaptive approach, two independent simulations are performed: one with GSODF for low aspect ratio grains and another with GSODF for high aspect ratio grains. The results from the two different GSODF simulations are averaged based on the corresponding volume fractions to obtain the overall stress for the microstructure ($< \boldsymbol{\sigma} >$) as follows:

$$< \boldsymbol{\sigma} >=< \boldsymbol{\sigma}^H > v_f^H + < \boldsymbol{\sigma}^L > (1 - v_f^H) \tag{2.18}$$

where, $< \boldsymbol{\sigma}^H >$ and $< \boldsymbol{\sigma}^L >$ are the average stresses predicted by the GSODF models for the high and low aspect ratio grains, respectively; and v_f^H is the volume fraction of high aspect ratio grains in the microstructure. The adaptive GSODF model is also

well suited to solving microstructures with multiple phases, for example, the high aspect ratio grains may constitute beta phase grains in a alpha–beta Titanium alloy microstructure.

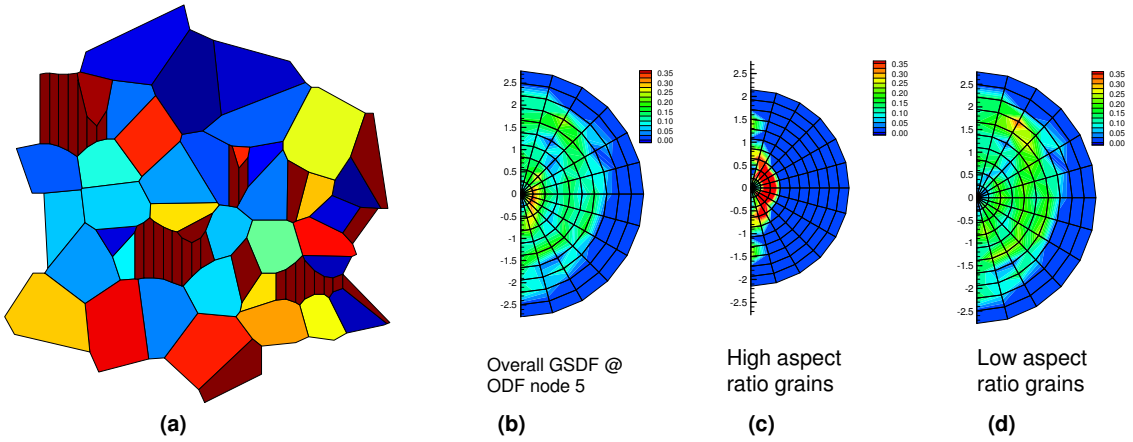

Figure 2.9: *(a) Initial microstructure with bimodal grain distribution. High aspect ratio grains ($L_{max}/L_{min} > 2.8$) are colored dark brown (b) Initial GSDF at $\boldsymbol{g} = 0.1745$ (c) The GSDF of high aspect grains and (d) The GSDF of all other grains at $\boldsymbol{g} = 0.1745$.*

Finite element simulation for the microstructure reveals high stresses in high aspect ratio grains as seen in Fig. 2.10a. The stress–strain response of these high aspect ratio grains as predicted by the GSODF model is shown in Fig. 2.10b. As seen from this figure, the stresses in the high aspect ratio grains are significantly larger than the low aspect ratio (equiaxed) grains. The averaged stress–strain response of the aggregate is also shown which is calculated based on Eq. 2.18. A comparison of the results from an average GSODF model versus the adaptive GSODF model and the Taylor aggregate model is shown in Fig. 2.11a. In the elastic regime, all three models give the same response. However, as expected, the results from the adaptive GSODF model is closer to the stress response predicted by the Taylor aggregate model in the plastic regime. The response for a cyclic loading case is also shown in Fig. 2.11b. Here, one complete deformation cycle with tension for 0.9 secs followed by compression for 1.8 secs and tension for another 1.8 secs is simulated. The adaptive GSODF

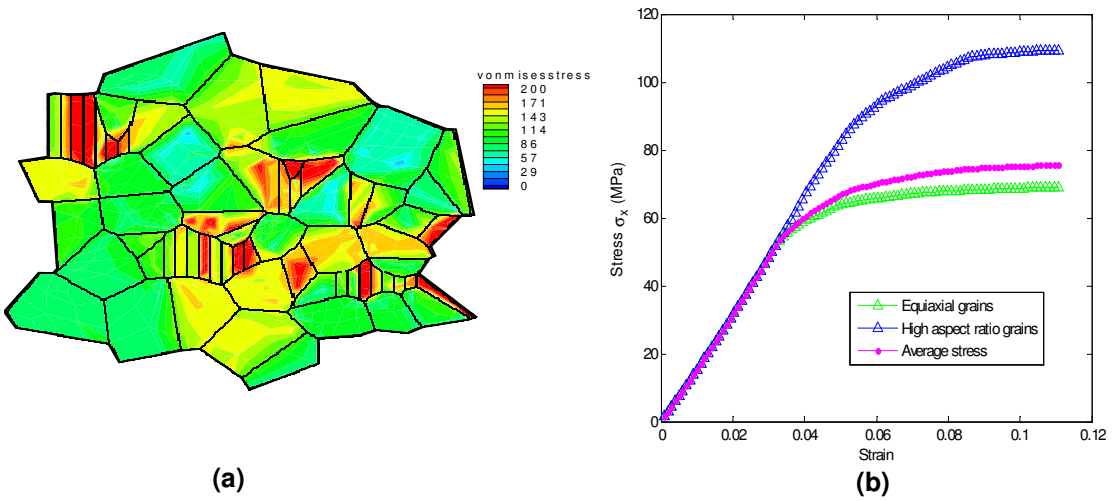

Figure 2.10: *(a) Von Mises stress distribution of the microstructure shows higher stresses in the high aspect ratio grains (b) Difference between the stress–strain response of high aspect ratio grains and equiaxial grains from GSODF model. The average stress–strain response of the aggregate is also shown.*

model is seen to more closely follow the response predicted by the Taylor–aggregate model.

The texture predicted by the GSODF model for the high aspect ratio grains at a strain of $\epsilon_x = 0.1$ is shown in Fig. 2.12a. From [60], it is seen that texture from tension process leads to an orientation sink at zero degrees and source at $\pm\pi/2$; with the basin of the sink spanning all of orientation space. Thus, the ODF will evolve exponentially with strain and eventually approach the asymptote which is a delta function, $A(r) = \delta(r - \pi/2)$. As seen in Fig. 2.12a, there is tendency for crystals with angles close to the origin to reorient farther away (sink) and an associated increase in the ODF close to the ideal orientation of $\theta = \pm\pi/2$ (source) as expected. The texture evolution predicted by the GSODF models and the Taylor aggregate model for a grain initially oriented at -0.799 rad is compared in Fig. 2.12b. Again, an adaptive GSODF model results in prediction of textures that are closer to that predicted by the more computationally expensive Taylor model.

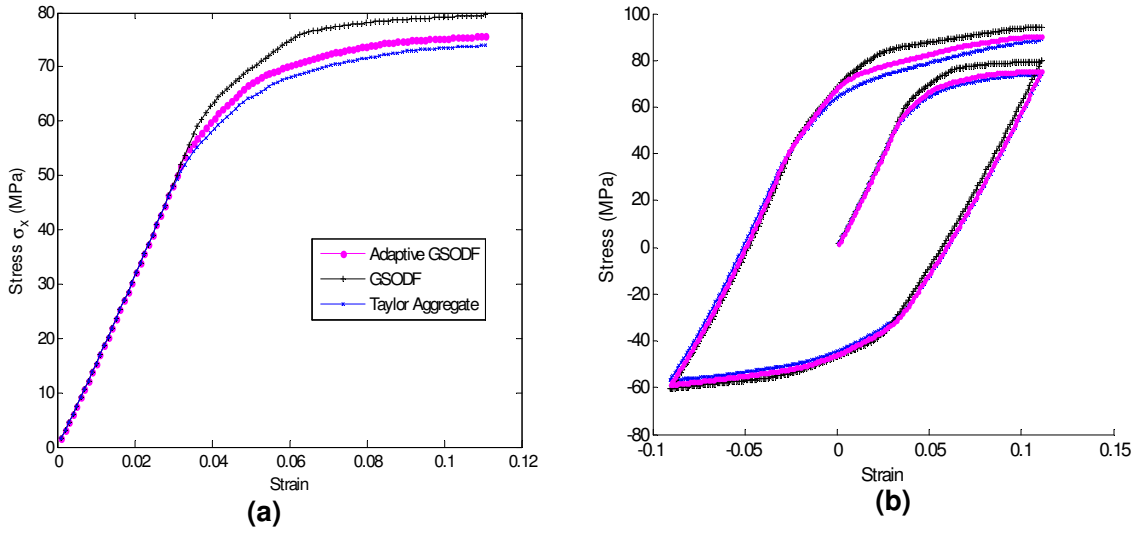

Figure 2.11: *(a) Comparison of stress–strain response predicted by adaptive GSODF model against the Taylor aggregate and GSODF model. (b) Comparison of response to cyclic deformation.*

Finally, a comparison of simulation times for the CPFE, Taylor aggregate and GSODF models is shown in Fig. 2.13. The simulation times are computed based on the first ten time steps ($\Delta t = 0.1$ sec) of each method and normalized with respect to the simulation time for the most expensive approach (i.e. the CPFE simulation). Note that the adaptive GSODF approach uses two different GSODFs to represent the bimodal microstructure. The evolution of these GSODFs are solved as two independent problems. Consequently, the computational time is also doubled compared to a single GSODF problem. However, the net simulation time is still significantly smaller than the Taylor or FE aggregate approaches. Also, the use of two independent GSODFs to represent the bimodal microstructure implies that probabilities are not transferred across the two GSODFs when grain shapes change. This assumption is admissible within the Taylor model where grain interactions are neglected and ultimately, volume averaging is employed. However, source and sink terms in the probability spaces do need to be considered when modeling additional physics such as grain fragmentation, recrystallization and twinning. Extension of the approach to model these effects will be considered in future work.

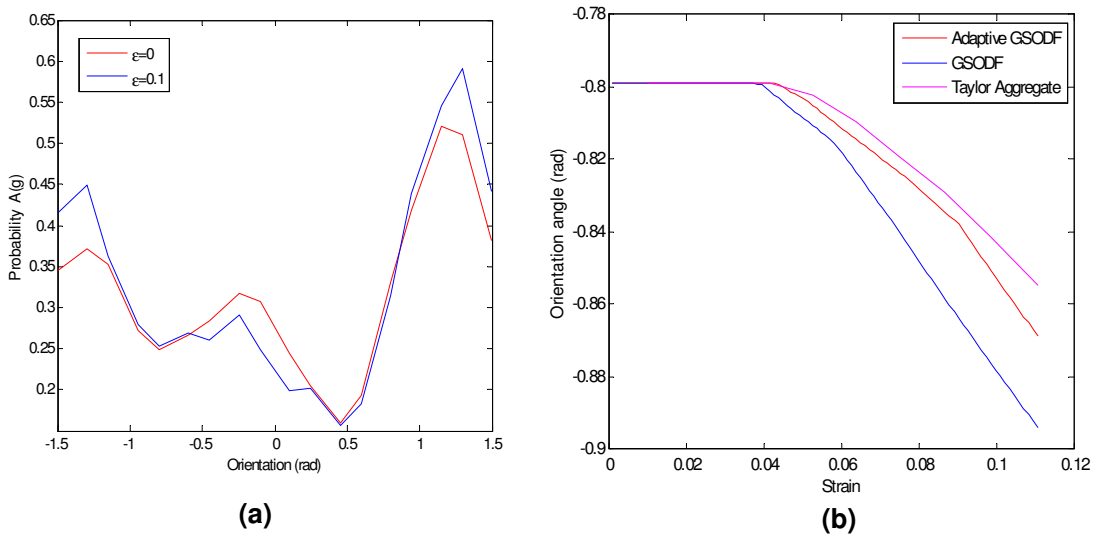

Figure 2.12: *(a) ODF evolution of the high aspect ratio grains. (b) Evolution of crystal orientation predicted by Taylor, GSODF and adaptive GSODF methods (for a crystal initially oriented at* $-0.799rad$*)*

From Fig. 2.13, it is clear that probabilistic methods (GSODF or adaptive GSODF methods) are significantly faster than FE and Taylor aggregate models. This is because of the use of only a few nodes in orientation space versus the use of complete microstructural meshes in the case of aggregate models. The simulation time for the GSODF model is independent of the size of the RVE since the statistics are represented over the same mesh for all cases. In contrast, as the number of elements in the RVE increases, the computational expense in aggregate models increase as $O(N^2)$. Note that both in the case of aggregate models or GSODF models, remeshing is required at large strains. Element distortion is significantly more of an issue for aggregate models where the entire microstructure needs to be remeshed at large strains. In the case of GSODF models, the nodal points in the orientation space may begin to overlap and interpenetrate at large strains, and remeshing (of the simpler orientation space) may be needed at large strains. The total Lagrangian approach used in this work is found to be adequate up to a strain of 1.25 for the case of the square–grained microstructure.

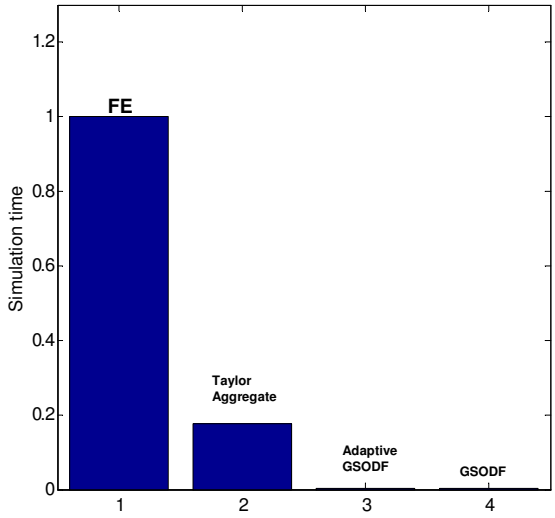

Figure 2.13: *Comparison of simulation times (normalized) for various methods. Probabilistic methods are significantly faster than FE and Taylor aggregate models.*

2.6 Conclusions

In this chapter, a new statistical theory that takes into account the coupling between grain size, shape and crystallographic texture during deformation of polycrystalline microstructures is introduced. The effect of grain shape is modeled by including the apparent grain size as seen by various different active slip systems in the grain within the constitutive law for the slip resistance. The coupling between the crystallographic texture and grain shape is considered by employing the 'grain size orientation distribution function' (GSODF) that encodes the probability density of finding a grain size D along direction $\boldsymbol{n}$ within grains of orientation g. The grain size orientation distribution function (GSODF) is sampled and represented in a finite element mesh. During elastoplastic deformation, the evolution of grain size D (in direction θ) and the orientation g is tracked by directly updating the GSODF probabilities using a Lagrangian probability update scheme. The GSODF model includes grain size information for each orientation (rather than each individual grain as in the case of Taylor or CPFE models). The GSODF model is identical to Taylor-aggregate

model if all grains have the same grain shape.

For distinctly bimodal microstructures, two GSODFs can be employed for different grain shapes which leads to results close to Taylor–aggregate model at a fraction of the computational cost. The role of grain shape (grain aspect ratio) is investigated in the case of two–dimensional microstructures and is found to be a significant factor in determining the overall plastic response. The yield stress approximately followed a parabolic relationship with logarithm of aspect ratio of grains with the minimum yield stress achieved in the case of a grain aspect ratio of one. The overall constitutive model reproduced the Hall Petch effect with the yield stress following an inverse square root relationship with the grain size. On the other hand, the evolution of GSDF itself does not significantly affect the initial yield stress but is found to be a consideration at large strain levels. In contrast to aggregate models (Taylor or CPFE), the simulation time for GSODF model is significantly smaller and is independent of the size of the microstructure. The improvement in computational efficiency achieved by GSODF models is most useful when performing multiscale design of industrial forming processes (eg. recent work in [66]) with bimodal or multimodal microstructures with varying grain shapes. Further, the nodes in the orientation space can be adaptively refined to ensure sharp probabilities can be captured. For example, a single crystal close to a crack tip can be modeled using a GSODF which is a delta function in the orientation space. Such sharp probability distributions can be generated by refining the element sizes in the orientation space. Farther from the notch tip, the experimentally measured ODF can be modeled within a regularly spaced grid. Adaptive methods to mesh and remesh the GSODF will be a subject of future study in this area, as will be methods to extend the simulation presented here to 3D orientation spaces (fcc, hcp) and to perform multiscale process simulations.

CHAPTER III

Multiscale Analysis of Single Edge Notch under Shear

3.1 A hybrid multiscale formulation of crystal plasticity

While crystal plasticity finite element (CPFE) method has emerged as an effective tool for simulating the mechanical response of aggregates of few hundred metallic crystals, simulation of 'macroscale' components that contain millions of grains is a challenging task even when using current state-of-the-art supercomputers. Of specific interest in this chapter is to efficiently simulate evolution of microstructural features during macroscale simulations using a novel, computationally efficient, tightly coupled, multiscaling technique. The statistical approach proposed in the previous chapter which is based on probabilistic description of microstructure is used at macroscale integration points to model the response of aggregates of several hundred grains. At the same time, crystals are individually resolved at critical regions such as stress concentrations where it is important to track the individual microstructural features. The configuration of the multiscale model is shown in Fig. 3.1. Here, the entire computational region is divided into two levels: macroscale and microscale. At the microscale level, aggregates of grains are explicitly modeled (that can be measured from experimental techniques such as electron backscatter diffraction). During defor-

mation, the microstructure evolution at the macroscale is captured by evolving the ODF. The evolution of ODF $\mathcal{A}$ was previously described in section 2.2 and will reiterate in section 3.4. The whole orientation space is divided into 9 parts from $-pi/2$ to $pi/2$. The transition from microscale to the macroscale is managed through adaptive meshing methods where element lengths can vary from micrometers at the critical regions to as large as several centimeters at the scale of the macroscale component.

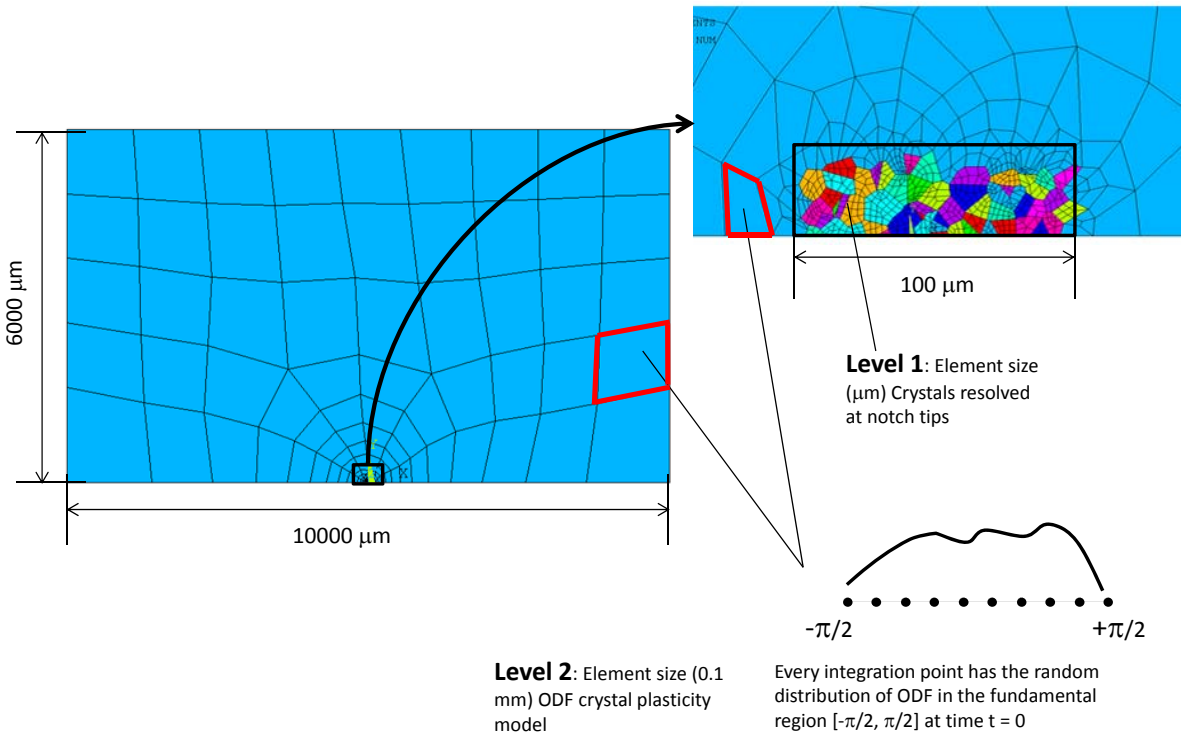

Figure 3.1: *The configuration of multiscale model. The whole model is divided into two levels, macroscale level and microscale level. The macroscale elements have the size in mm, represent number of grains using ODF, while microscale elements are in size of µm. Microscale elements represent grains explicitly with orientation shown in different colors.*

3.2 Elasto-plastic constitutive model

The classical single-crystal plasticity theory employed here is the same as section 2.3. However, the grain size effects are not included and only the ODF is employed

rather than the GSODF. The slip system resistance has thus been modified in this Chapter as:

$$\dot{s}^{\alpha}(t) = \sum_{\beta} h^{\alpha\beta}\dot{\gamma}^{\beta}(t), \text{ with } s^{\alpha}(0) = \tau_0^{\alpha} \tag{3.1}$$

$$\text{where, } h^{\alpha\beta} = h_o^{\beta}(q + (1-q)\delta^{\alpha\beta})(1 - \frac{s^{\beta}(t)}{s_s^{\beta}})^a \text{ (no sum on } \beta) \tag{3.2}$$

A rate independent algorithm same as section 2.3 is employed to solve the single crystal model.

3.3 Kinematics

The equilibrium equation is expressed in the Lagrangian framework as:

$$\nabla_0 \cdot \langle \boldsymbol{P} \rangle + \boldsymbol{f} = \boldsymbol{0} \tag{3.3}$$

where ∇_0 is the divergence described in the initial reference configuration ($t = 0$) and $\boldsymbol{f}$ denotes the body forces. The polycrystal Piola-Kirchhoff-I stress, $\langle \boldsymbol{P} \rangle$ is defined as:

$$\langle \boldsymbol{P} \rangle = \det\boldsymbol{F}\langle \boldsymbol{\sigma} \rangle \boldsymbol{F}^{-T} \tag{3.4}$$

For any kinematically admissible test function $\tilde{\boldsymbol{u}}$, the weak form of the virtual work equation with applied surface traction $\boldsymbol{\lambda}$ can be written as:

$$\mathcal{G}(\boldsymbol{u}_{n+1}, \tilde{\boldsymbol{u}}) \equiv \int_{\mathcal{B}_0} \langle \boldsymbol{P} \rangle \cdot \nabla_0 \tilde{\boldsymbol{u}} dV - \int_{\partial\mathcal{B}_0} \boldsymbol{\lambda} \cdot \tilde{\boldsymbol{u}} dA - \int_{\mathcal{B}_0} \boldsymbol{f} \cdot \tilde{\boldsymbol{u}} dV = 0 \tag{3.5}$$

The Newton-Raphson iterative scheme with a line search procedure is employed to solve the weak form while using a formulation that uses a combination of triangle

and quadrilateral elements:

$$\frac{\partial \mathcal{G}(\boldsymbol{u}_n, \tilde{\boldsymbol{u}})}{\partial \boldsymbol{u}_n}\Delta\boldsymbol{u} = \int_{\mathcal{B}_0} \frac{\partial \langle \boldsymbol{P} \rangle}{\partial \boldsymbol{F}} \frac{\partial \boldsymbol{F}}{\partial \boldsymbol{u}_n} \cdot \nabla_0 \tilde{\boldsymbol{u}} dV \Delta\boldsymbol{u} = \mathcal{G}(\boldsymbol{u}_n, \tilde{\boldsymbol{u}}) \tag{3.6}$$

The linearization process of PK–I stress at time τ can be found in Appendix B.

The average stress and tangent modulus at the macroscale level are obtained by averaging over the ODF as given in Eq. 2.16. At the microscale, the tangent modulus and stress are exactly computed in the elements within individual crystals.

3.4 Constitutive model in macroscopic regions

At the macroscale, each integration point models the response of aggregates of several hundred grains probabilistically using an orientation distribution function (ODF). The ODF, $\mathcal{A}(\boldsymbol{g})$, gives the probability density of finding an orientation $\boldsymbol{g}$ in the microstructure. The ODF satisfies the following conservation equation at all times during deformation as Eq. 2.2. The evolution of ODF is given by the conservation Eq. 2.2 as Eq. 2.4. Using the Jacobian, a map of the current mesh (at time t) to the reference mesh (at $t = 0$) can be made as Eq. 2.5. If the integrand is continuous, a localized relationship of the following form can be used to update the ODF at any time t, as Eq. 2.6.

During deformation, it is assumed that every orientation is subject to the same macroscopic deformation gradient $\boldsymbol{F}$. Once the stress $\boldsymbol{\sigma}$ at each orientation is computed using the single crystal model in section II, the stress $< \boldsymbol{\sigma} >$ at the macroscale is obtained by averaging over the ODF as Eq. 2.16. The average tangent modulus for the macrostructure is obtained in a similar way: $< \frac{\partial \boldsymbol{\sigma}}{\partial \boldsymbol{F}} >= \int \frac{\partial \hat{\boldsymbol{\sigma}}}{\partial \boldsymbol{F}} \mathcal{A}(\boldsymbol{g}_o, t = 0) d\boldsymbol{g}_o$.

3.5 Numerical results

Due to the difference in the hardening law when comparing with section 2.5, the parameters in the hardening law are taken to be as follows: $\tau_0^\alpha = 10$ MPa, $h_o^\alpha = 10$ MPa, $s_s^\alpha = 200$ MPa, $q = 1.4$ and $a = 2$. Two slip systems in the crystal are also in the $-\pi/6$ and $+\pi/6$ direction. In the 2-D elastic stiffness matrix, $\mathcal{C}_{11} = 2\ GPa$ and $\mathcal{C}_{12} = \mathcal{C}_{44} = 1\ GPa$. The calculation is done under plane stress conditions.

The single edge notch configuration (also called Wedge-Opening Load (WOL) specimen) is depicted in Fig. 3.2. The calculation is only performed using one half of the model for simplicity, although a complete model will be developed later to account for the nonsymmetric microstructure around the crack tip. A 5000 N shear force p is applied on the left edge. The $a/w = 0.5$, $h/w = 0.6$, a is the notch length, w is the width of the specimen, $2h$ is the height of the specimen, b is unit breath, for plane stress problem, $b = 1m$. Values of $a = 50mm$ and $w = 100mm$ are shown in Fig. 3.1. All the figures are plotted using non-dimensional variables, $\frac{K_I b\sqrt{w}}{p}$ and r/w. The solution leads to a stress singularity at the notch tip. There is a wealth of literature of the use of special elements to capture this crack tip singularity, the most popular of which are the quarter point elements that capture the $1/\sqrt{r}$ dependence of crack tip singularity in linear elasticity or the $1/r$ dependence in perfect plasticity. However, the singularity of the crack tip solution in crystal plasticity is not known analytically, which makes the design of such elements non–trivial. For simplicity, conventional finite elements (combination of three noded triangular and four noded rectangular elements) are employed in these simulations. Meaningful values of crack tip stress intensity factors can be obtained using this approach using computational procedures demonstrated in Chan (1970) [25].

Only mode I crack is considered here. The stress intensity factor calculation is

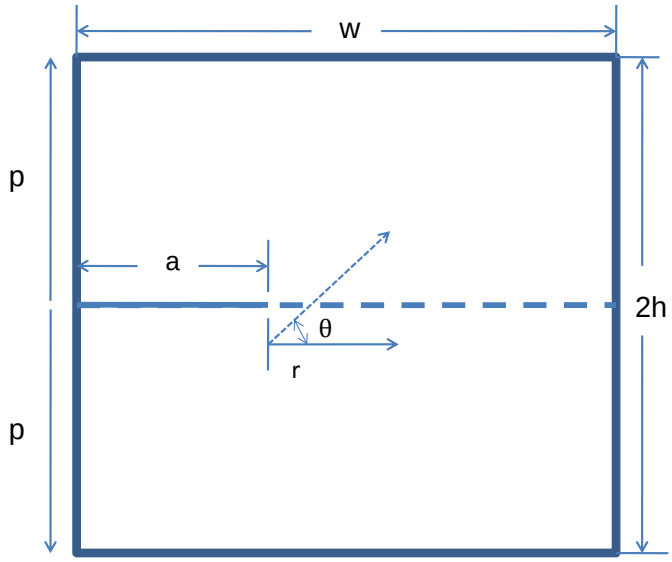

Figure 3.2: *The single edge notch configuration with width w, hight 2h, shear force p is applied on the left edge. Only upper half of the model is modeled due to the symmetry.*

following Chan's paper [25]. Stress intensity K_I^* from displacement–based method:

$$K_I^* = \left[\frac{2\pi}{r}\right]^{\frac{1}{2}} \frac{Gv^*}{f(\theta,\nu)} \tag{3.7}$$

$f(\theta,\nu) = \sin(\frac{\theta}{2})\left[2-2\nu-\cos^2\frac{\theta}{2}\right]$, v^* is the computed nodal displacement in y direction. The K_I^* is obtained by substituting a calculated nodal point displacement v^* at point (r,θ). If the v^* were the exact theoretical value, then the value of K_I^* will also be exact. The above equation is for plane strain situation, for plane stress cases, ν is just needed to be replaced by $\nu/(1+\nu)$ for $f(\theta,\nu)$.

The stress intensity factor K_I^* from stress–based method is also used for comparison:

$$K_I^* = \frac{(2\pi r)^{\frac{1}{2}}\sigma_{yy}^*(r,\theta)}{f_{yy}(\theta)} \tag{3.8}$$

$f_{yy}(\theta) = \cos(\theta/2)\left[1+\sin(\theta/2)\sin(3\theta/2)\right]$. This theoretical result is obtained from the collocation method described in [67].

J integral for the plane structure is:

$$J = \int_{\Gamma} \left(W dy - \boldsymbol{T} \cdot \frac{\partial \boldsymbol{u}}{\partial x} ds \right) \tag{3.9}$$

The Γ is an arbitrary curve surrounding the crack tip. W is the strain energy density, while $\boldsymbol{T}$ is the traction vector defined by the out normal along Γ, $T_i = \sigma_{ij} n_j$, and $\boldsymbol{u}$ is the displacement vector. The integral is evaluated counterclockwise around the crack tip. the J value is as twice as the half plane's J value. Strain energy density W is getting from PK–I stress returned from Eq. 3.4 and deformation gradient $\boldsymbol{F}$, $W = \int_{\Omega_0} \boldsymbol{P} : \delta \boldsymbol{F} dV$. To get the value for the W, the applied load has to be discretized to small steps and do. In this work, the shear force on the left boundary of the model is applied in 20 steps to get the W.

3.5.1 Linear elastic simulations

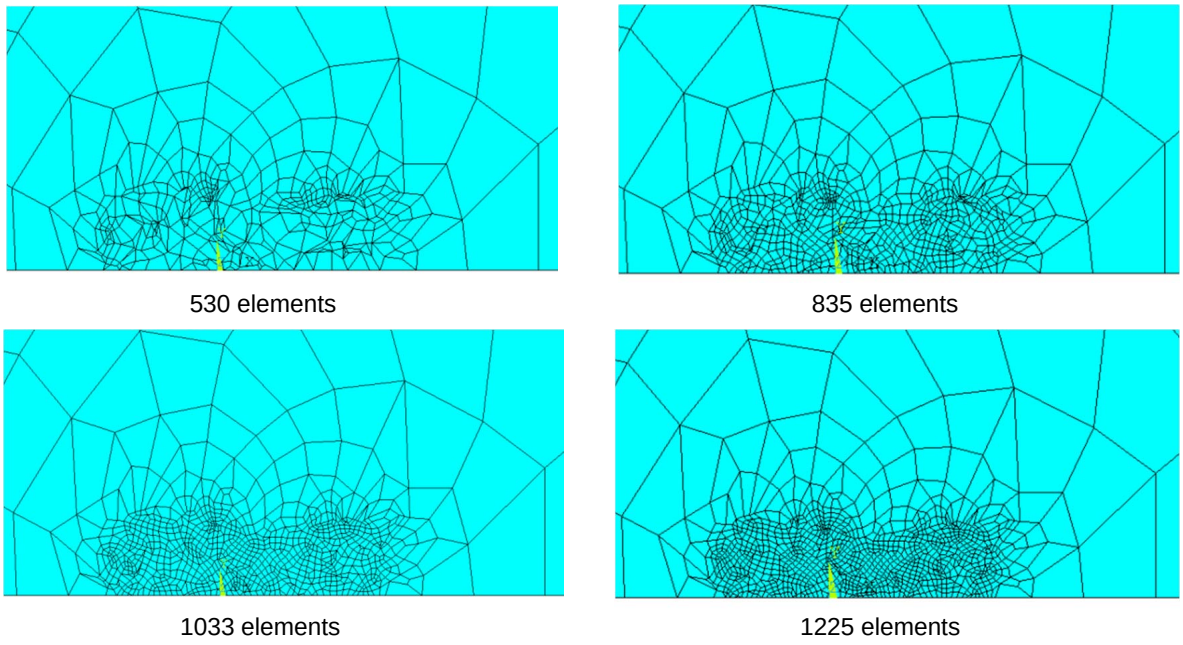

Figure 3.3: *Grids show of* 530, 835, 1033 *and* 1225 *elements for* 62 *grains.*

The first few tests are performed by setting the plastic shearing strain to zero $\Delta\gamma =$

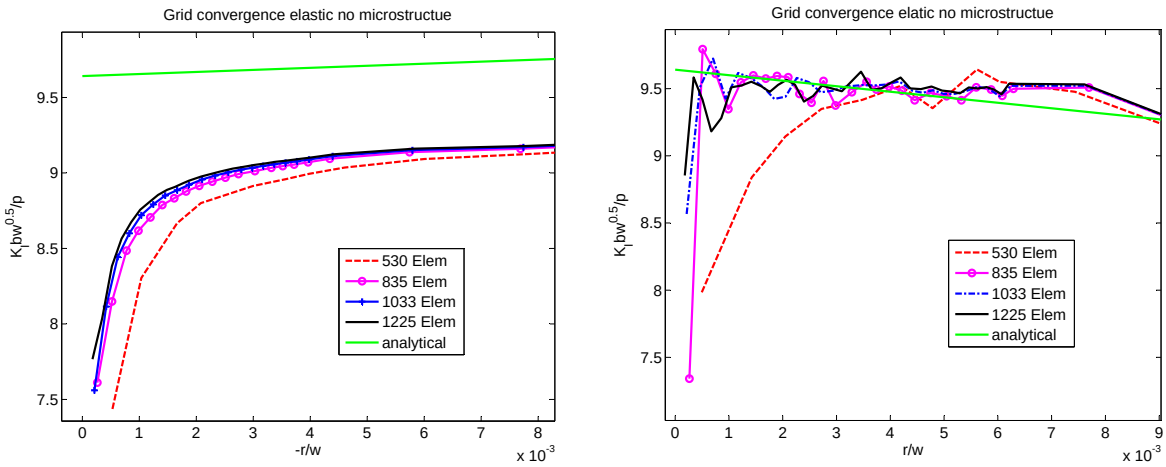

(a) (b)

Figure 3.4: *Grid convergence test with* 530 *elements,* 835 *elements,* 1033 *elements and* 1225 *elements for* 62 *grains on elastic all ODF model. Analytical line is from the collocation method. (a) Non-dimensional K_I from displacement method. (b) Non-dimensional K_I from stress method. Both results show that convergence start from* 835 *elements.*

0 which leads to a fully elastic model. Note that every grain still has its own elastic properties along a direction as given by its crystal orientation. In the convergence results shown below, the stress intensity factor K_I getting from displacement on the crack surface($\theta = \pi$) and from stress σ_{yy} on the $\theta = 0$ plane (away from the crack in the positive x– direction) are shown.

First, a convergence test is performed on different meshes by progressively refining the element size in the microstructure, see Fig. 3.3. In this simulation, a fully isotropic model is employed without any microstructure. The test shows good convergence with increasing number of elements as shown in Fig. 3.4 and the results are similar to those reported in the finite element model of [25]. Analytical result is from [67].

A similar convergence test is performed by altering the number of grains in the vicinity of the crack tip (and 835 elements in each case, see Fig. 3.5). The zero grain case corresponds to the isotropic elastic case (that corresponds to a fully random ODF). This corresponds to an isotropic stiffness matrix with $\mathcal{C}_{11} = 2.25\ Gpa$, $\mathcal{C}_{12} =$

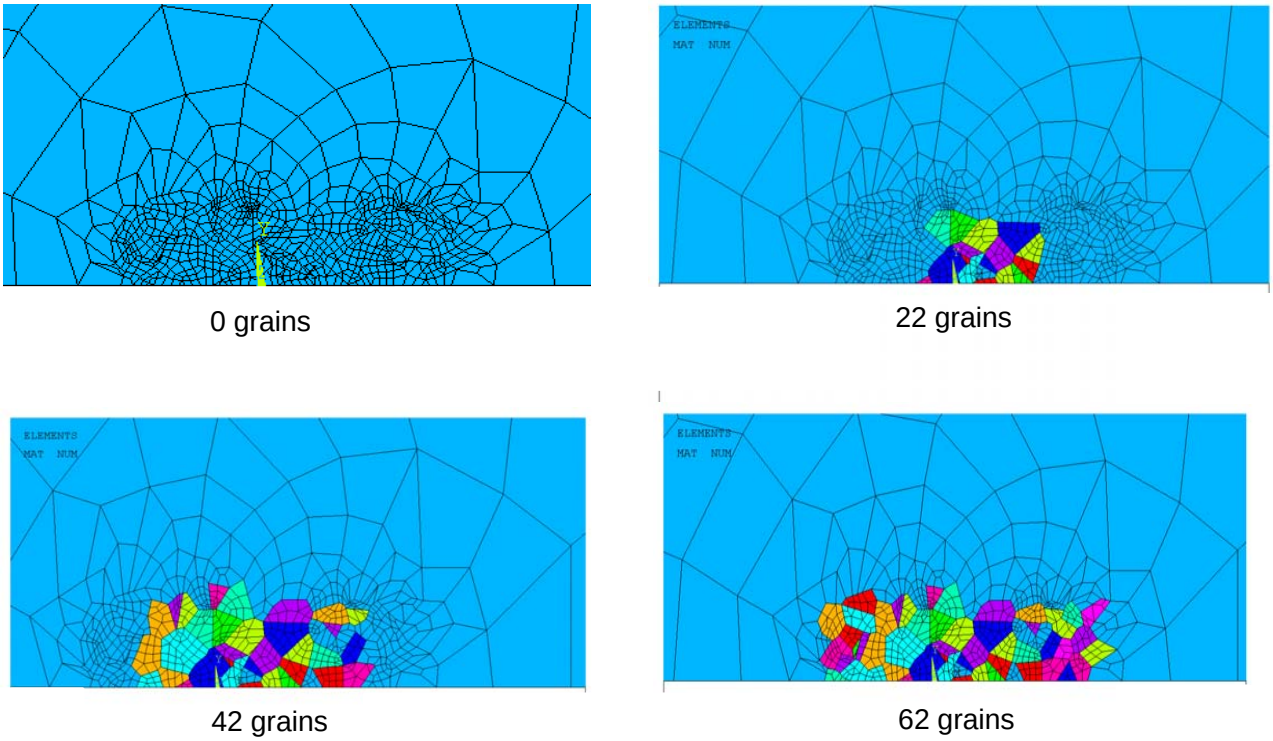

Figure 3.5: *Grids with increasing number of grains near the crack tip (*22*,* 42 *and* 62 *grains) with* 835 *elements. Different numbers of grains are used to test the critical area needs to be covered by crystals.*

0.75 Gpa and $\mathcal{C}_{44} = 0.75$ Gpa. The grain convergence study allows one to choose the size of the critical region that needs to be modeled using microstructural grids. From the results shown in Fig. 3.6, there is the trend towards convergence with increasing number of grains. As the number of grains increase from 42 to 62, little additional accuracy is realized. This implies that a 42 grains case is sufficient to address this particular problem. Beyond this point, the ODF model may be employed without losing accuracy. Further, a quick comparison of the zero grain case (isotropic solution) with the 62 grains case result in Fig. 3.6 clearly depicts the role of microstructure in determining the stress concentration at the crack tip. When r/w is smaller than 6×10^{-3}, stress concentrations is deviated from the isotropic case. While r/w is larger than 6×10^{-3}, the microstructure does not play a significant role and the result converges to the isotropic solution. The detailed comparison between an all ODF

model with elasticity (zero grains) and one with microstructure explicitly modeled in Fig. 3.7. The model with explicit microstructure has more prominent values near crack tip. The all ODF model has the exact same result when comparing with isotropic result can also been seen in Fig. 3.7. Fig. 3.8 additionally depicts the resolved shear stress in the two slip systems for the elastic model as overlaid on the grains showing significant variability in stresses from grain to grain - again stressing the need for a microstructure model at critical regions.

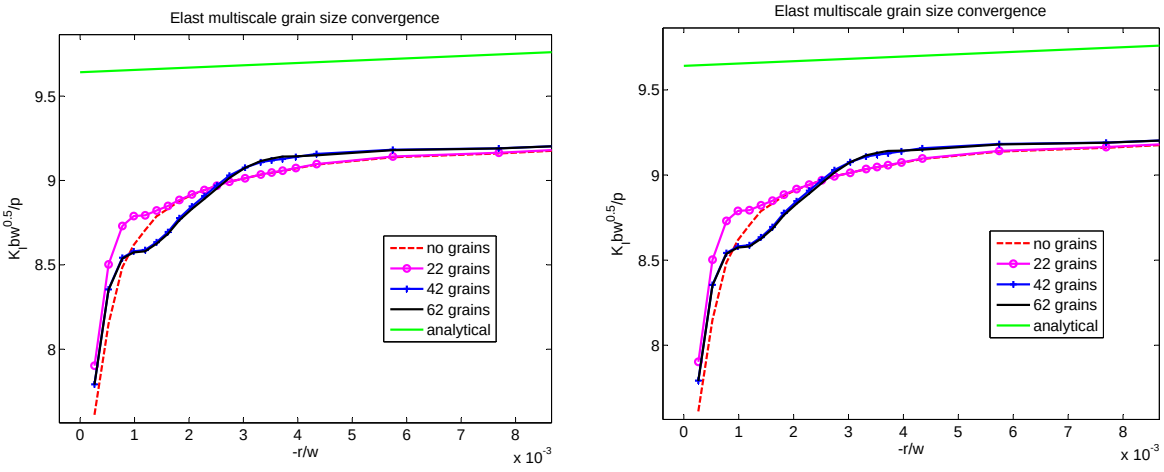

Figure 3.6: *Size convergence test with* 0,22,42,62 *grains. (a) Non-dimensional* K_I *from displacement method. (b) Non-dimensional* K_I *from stress method. The results show that convergence can be achieved by more than* 42 *grains.*

3.5.2 Elasto–plastic simulations

In subsequent simulations, notch tip plasticity is turned on. All test cases are based on meshes with 835 elements and 62 grains cover notch tip area. Inclusion of notch tip plasticity leads to a larger displacement at the crack tip (and also smaller stress near the crack tip). This is seen in Fig. 3.9 where the displacements and stresses are directly compared to the elastic case. These results are subsequently shown in terms of the non–dimensional stress intensity factor in Fig. 3.10. Note that on the

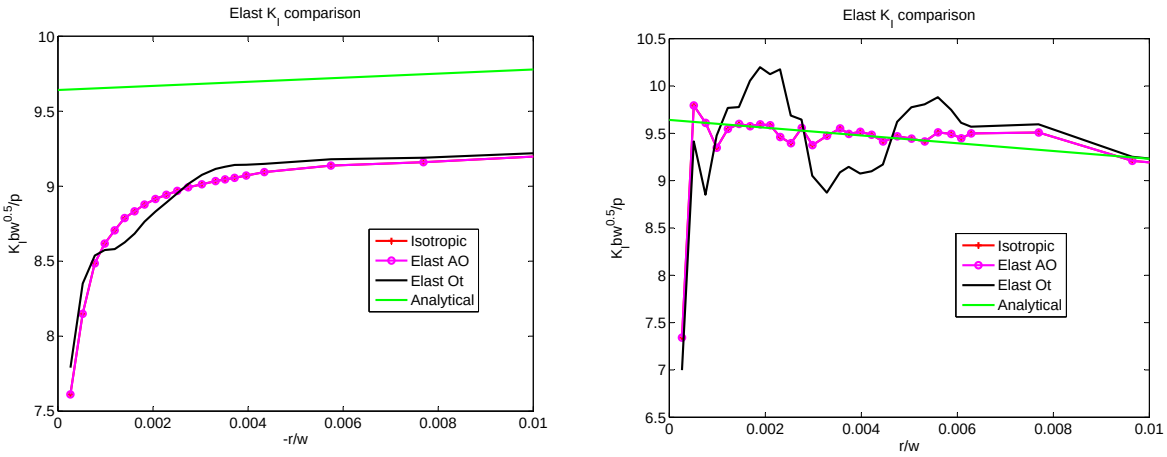

Figure 3.7: *Elastic K_I comparison between isotropic, elastic model with orientations and elastic model with ODF in all elements. Elastic all ODF and isotropic model return the exact same value. Elastic model with microstructure has more prominent oscillation values around crack tip.*

$\theta = \pi$ plane, the stress intensity factor Eq. 3.7 as computed from the elasticity–based formula will be larger in the plastic case due to larger displacement. On the other hand, the smaller stress σ_{yy} on the $\theta = 0$ plane will lead to a smaller K_I value based on the Eq. 3.8. These are simply artifacts of using a elasticity–based analytical solution to calculate the stress intensity factor. Due to the larger displacement and smaller stresses around crack tips, elasto–plastic results show altogether different K_I trends when compared to the fully elastic case in Fig. 3.7. Next, comparing an all ODF model with plasticity (zero grains) and one with microstructure explicitly modeled, the differences between these two cases (shown in Fig. 3.10) are much more pronounced than the fully elastic case (that did a similar comparison between no grains and 62 grains case, see Fig. 3.6). The inclusion of microstructure significantly affects the calculated stress intensity factor, which is important during assessment of safety factors during component design. Fig. 3.11 additionally depicts the resolved shear stress in the two slip systems for the elasto–plastic model as overlaid on the grains. This again shows significant variability in stresses from grain to grain but

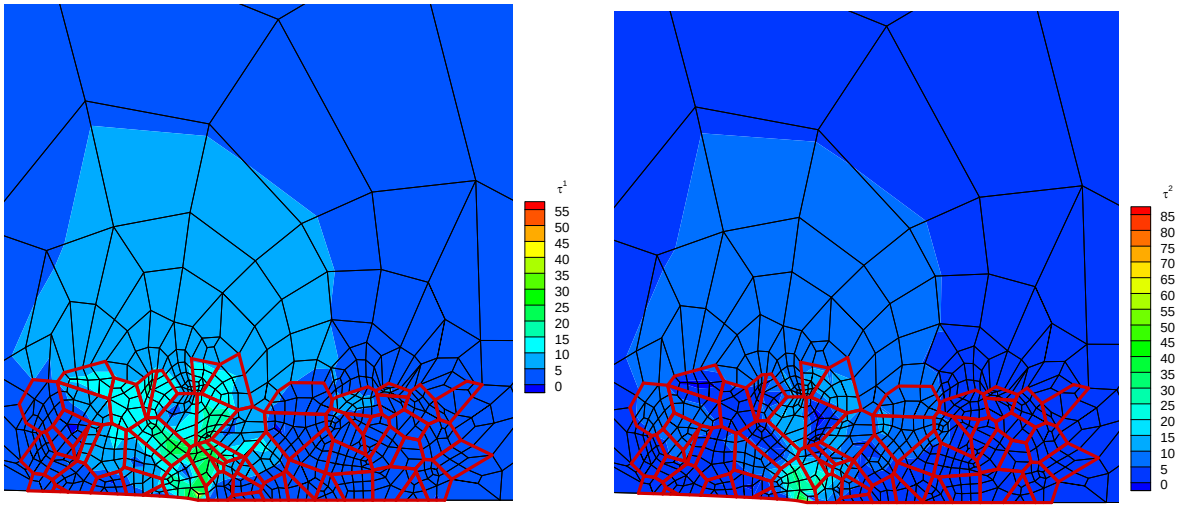

(a) (b)

Figure 3.8: *Resolved shear stress results in two slip systems for elastic model with orientations. The maximum shear stresses reach as high as* 85 *Mpa.*

stresses are smaller than the fully elastic case shown in Fig. 3.8 as expected.

3.5.3 J Integral Calculation

Five curves are drawn around crack tip to get the J integral. The inner most curve is within only one grain, while the outmost curve circumscribes all explicit modeled microstructure. Curves are shown in Fig. 3.12 and results of the J integral is in Fig. 3.13. The J integral of models with orientations are normalized with result of models with no grain. J integral value shows the same trend with Fig. 3.7 and Fig. 3.10 that model with microstructure has more prominent oscillation values around crack tip.

3.5.4 ODF Evolution

Finally, it is seen that texture evolve with the specimen deformation. The elastic ODF result will stay the same with the initial ODF values because the Jacobian in this case is simply equal to one ($J_F(\boldsymbol{r}_o, t|\boldsymbol{g}) = \det(\boldsymbol{F}^p(\boldsymbol{g}, t)) = 1$. Here only ODF

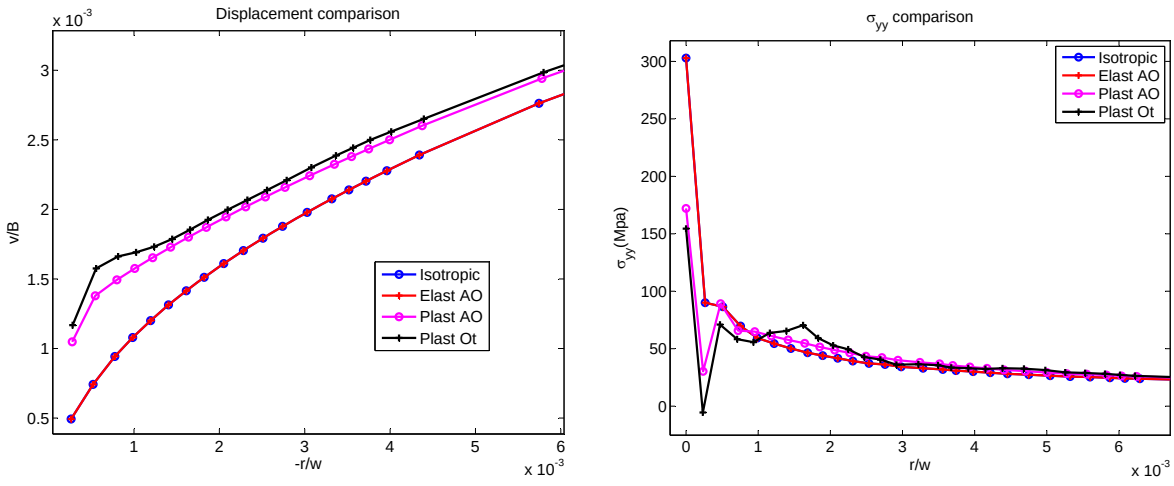

(a) (b)

Figure 3.9: *Displacement and σ_{yy} comparison between isotropic, elastic and plastic models with* 835 *elements. (a) Comparison of displacement between different models. The isotropic and elastic all ODF models return the same displacement. The plastic models have larger displacement on the $\theta = \pi$ plane due to the softer stiffness when the crack is formed. (b) Comparison of σ_{yy} between different models. The isotropic and elastic all ODF models still have the same values. The plastic models have small values around the crack tips because of the σ_{yy} reaches the yield stress. However, beyond crack tip area, the σ_{yy} of plastic models is higher than elastic models because of the larger displacement. Plastic model with microstructure shows non-smoothness because of the microstructure.*

evolution from plastic cases are shown in Fig. 3.14. Two neighboring elements' ODF have similar results due to the almost same deformation.

3.6 Conclusions

The proposed multiscale model combines the computational efficiency of statistical approaches with the accuracy of CPFE at critical regions. The approach can provide detailed stress and displacement results around critical regions such as crack tips and localized loads (eg. indentation tests) while also providing good estimates of far field stresses. As an illustrative example, we applied the multiscaling method to compute the stress intensity factor K_I around the crack tip in a wedge–opening load specimen

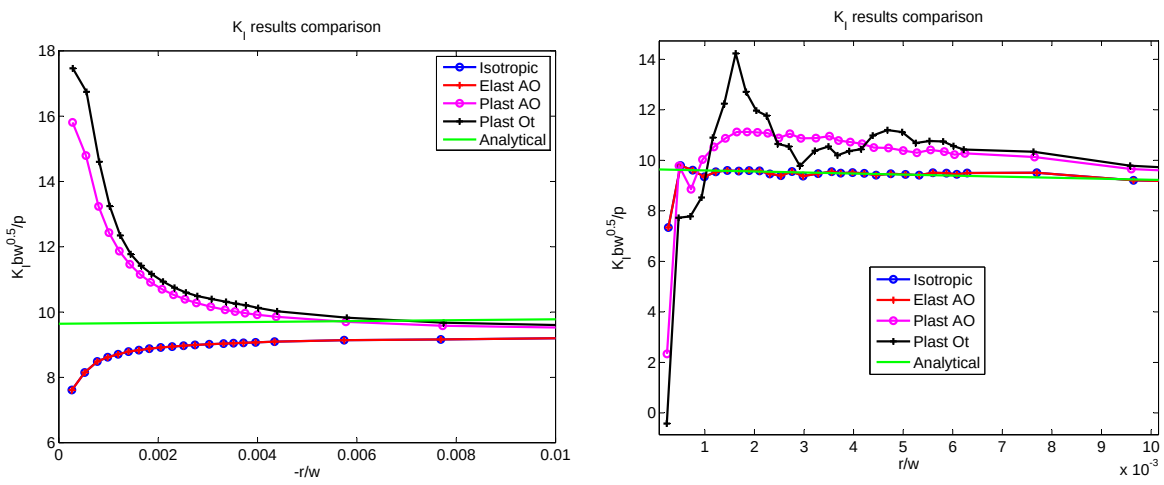

Figure 3.10: *Stress intensity factor comparisons between isotropic, elastic all ODF model , plastic model with orientations near crack tip and plastic model with ODF in all elements. Elastic all ODF and isotropic returns the exact same value. K_I calculated from plastic models return different trend when comparing with elastic models.*

[25]. The approach is verified with an analytical solution within linear elasticity and has been extended to allow modeling of crack tip plasticity. This framework is extended to allow modeling of arbitrary crack paths at critical regions within the multiscale approach. This is described in the next chapter.

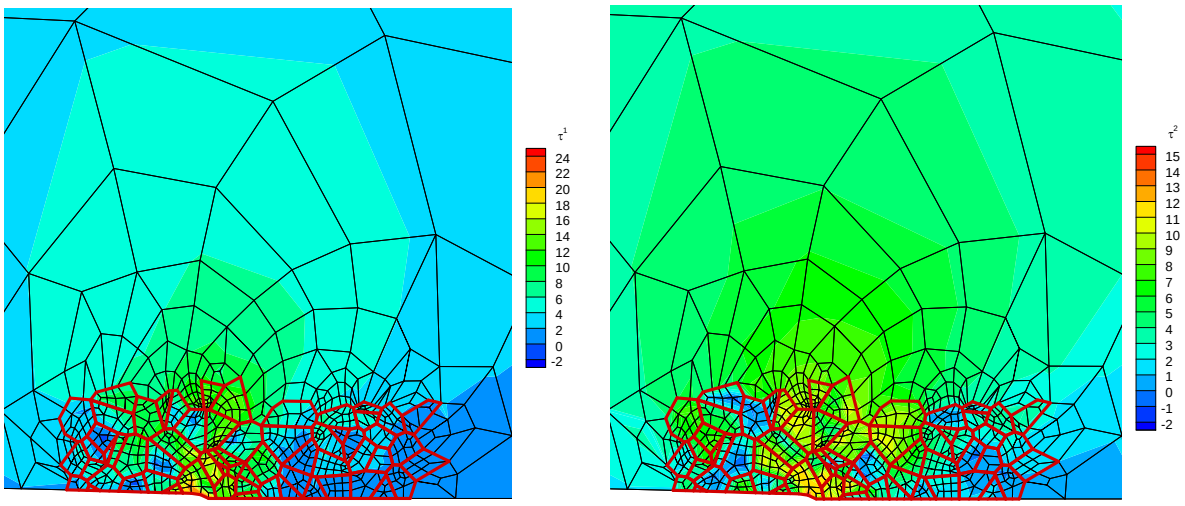

(a) (b)

Figure 3.11: *Resolved shear stress results in two slip systems for plastic model with orientations. Due to the plasticity, the maximum shear stress only reaches* 16 *Mpa.*

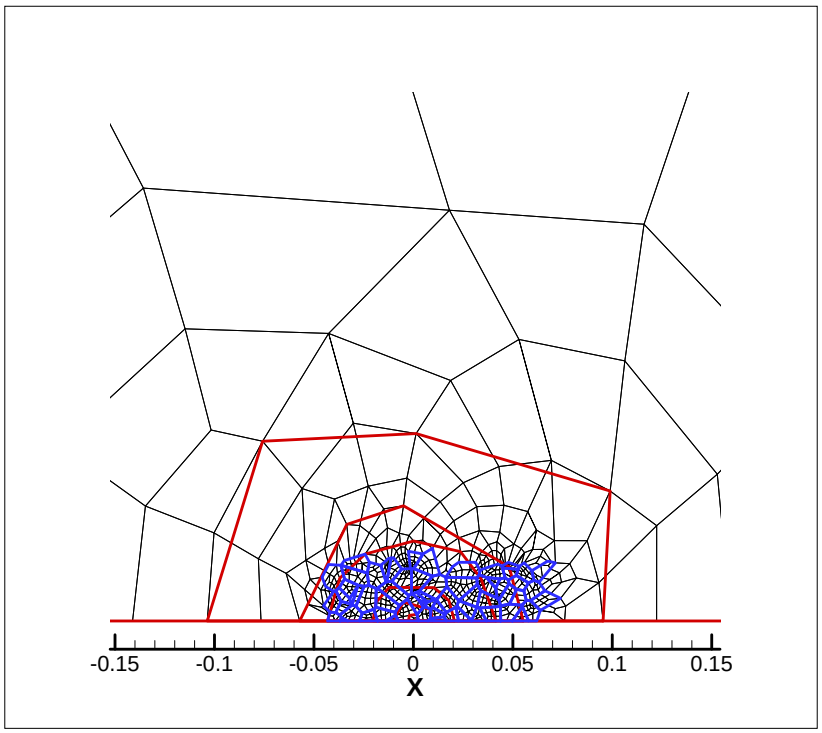

Figure 3.12: *J integral curves around the crack tip, the red lines are curves, blue lines are crystals and black ones are FE elements. The innermost curve is only within one crystal. Other curves cover larger areas. Each edge of the curve is divided into* 10 *parts. It means that if the curve has* 5 *edges, there are* 50 *points are integrated to get J value.*

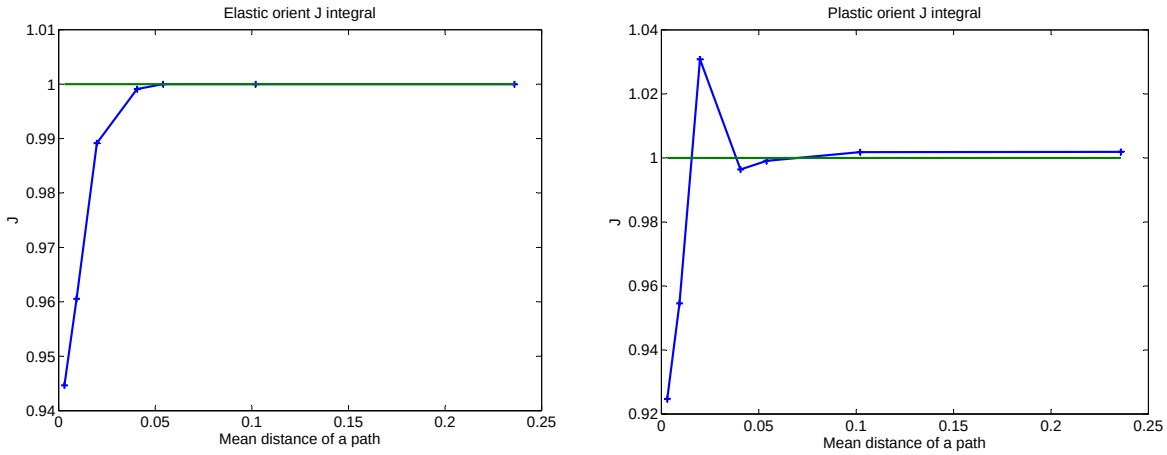

(a) (b)

Figure 3.13: *J integral comparison. The x coordinate is the mean distance values of all integration points on different integral curves. (a) J values of elastic model with microstructure is normalized with elastic all ODF model. The elastic model with microstructure has lower J values at the crack tip, but converges to all ODF model at far field. (b) J integral of plastic model with microstructure normalized with plastic all ODF model. Plastic model with microstructure converges to the plastic all ODF model at far field. The near field plastic J values oscillate because of the influence of the crystals.*

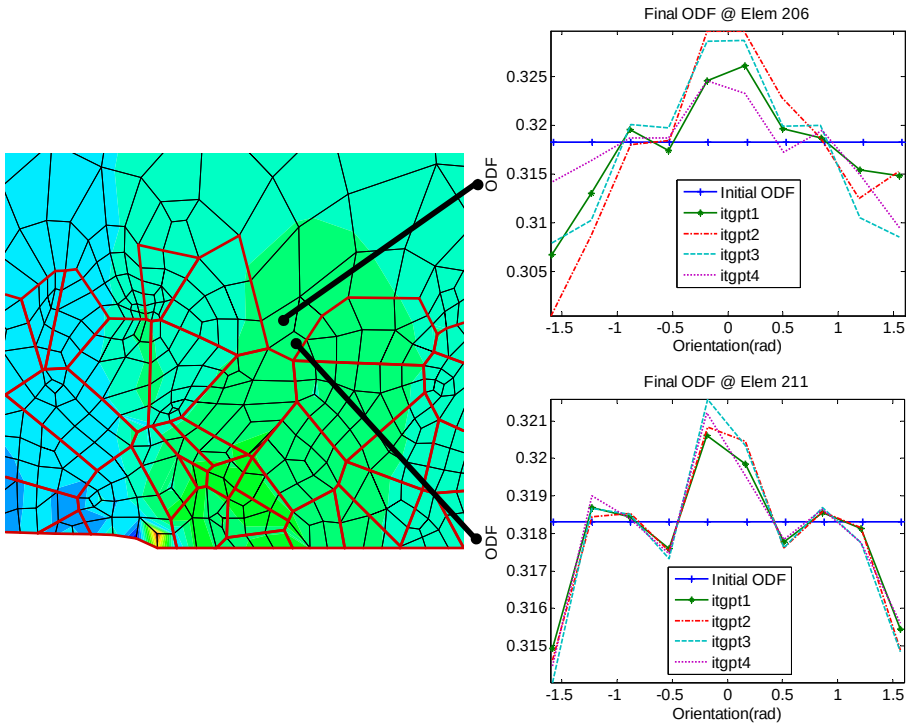

Figure 3.14: *The final texture returned from elasto-plastic model at macroscale elements. Evolution of ODF at different integration point is different, but for the elastic result, ODF evolution at difference integration point is the same.*

CHAPTER IV

Modeling Crack Propagation in Polycrystalline Alloys using Variational Multiscale Cohesive Method

[1]In this chapter, the variational multiscale method (VMM) (Garikipati 1998, 2002 [41, 42]) which can be seen as the development from Embedded Elements (EFEM) is used to embed the cohesive elements selectively in critical regions. In this approach, the displacement discontinuities are represented over unstructured meshes using specially constructed element shape functions that are discontinuous. Here it is uesed to embed the cohesive zone models within an element to allow simulating arbitrary crack path that include both intergranular and transgranular failure in polycrystals.

Rudraraju [43, 44, 69] have recently develop the use of VMM to Variation Multiscale Cohesive Method (VMCM) for prediction of crack propagation in laminated fiber reinforced composites and shown good correlation with experiments. In this work, VMCM is extended to polycrystalline microstructures. In order to efficiently calculate the crack in the grain level, the multiscale model in Chapter III is used. The entire computational region is divided into two levels: macroscale and microscale. At the microscale level where microstructure crack might exist, aggregates of grains are

[1]Reproduced from S. Sun and V. Sundararaghavan. "Modeling Crack Propagation in Polycrystalline Alloys using Variational Multiscale Cohesive Method", Computational Mechanics, in review. 2014. [68]

explicitly modeled. During deformation, the microstructure evolution at the macroscale is captured by evolving the Orientation Distribution Function (ODF). The evolution of ODF $\mathcal{A}$ was described in Section 2.2.

The chapter is organized as follows. In Section 4.1, VMCM scheme is briefly introduced. Section 4.2 and Section 4.3 briefly reiterate the constitutive modeling of single crystal at the microscale level and macroscale level of the multiscale model which is discussed in Chapter III. Section 4.4 presents the details of VMCM implementation using the finite element method. Simulations of convergence tests and transgranular and intergranular crack propagation cases are provided in this section, while concluding remarks are presented in Section 4.5.

4.1 Introduction of VMCM

The kinematic problem for the two–dimensional microstructure deformation problem employs an updated Lagrangian framework. Let $\boldsymbol{F}_n = \nabla_0 \tilde{\boldsymbol{x}}(\boldsymbol{X}_0, t_n)$ refer to the total deformation gradient in the reference configuration (Ω_n) at time t_n with respect to the initial undeformed configuration (Ω_0) at time $t = 0$. Similarly, the total deformation gradient in the current configuration (Ω_{n+1}) at time $t = t_{n+1}$ is written as $\boldsymbol{F}_{n+1} = \nabla_0 \tilde{\boldsymbol{x}}(\boldsymbol{X}_0, t_{n+1})$. Let $\boldsymbol{F}_r$ denote the relative deformation gradient between the two configurations, i.e.,

$$\boldsymbol{F}_r = \boldsymbol{F}_{n+1}(\boldsymbol{F}_n)^{-1} \tag{4.1}$$

A crack at time step n in a cohesive formulation is represented as a surface Γ_n^c. The displacement jump at the crack is denoted as $[\![\boldsymbol{u}]\!]$. The crack surface in this configuration has a normal direction $\boldsymbol{n}$ and tangential direction $\boldsymbol{m}$ as shown in Fig. 4.1.

Standard finite element procedure for deformation problems involve solving for the displacements $\boldsymbol{d}$ at nodes in the finite element mesh. In the variational multiscale

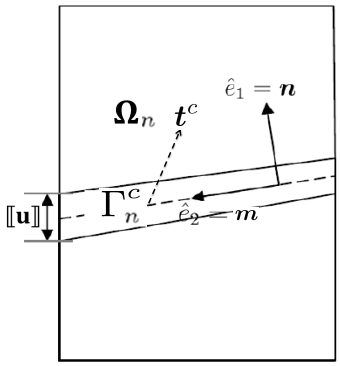

Figure 4.1: *Representation of crack opening* $[\![\boldsymbol{u}]\!]$*, domain* Ω_n *and crack surface* Γ_n^c*. Crack surface has normal direction* $\boldsymbol{n}$ *and tangent direction* $\boldsymbol{m}$*. Nominal traction on the crack surface is denoted as* $\boldsymbol{t}^c$*.*

approach, $\boldsymbol{d}$ is regarded as a coarse scale unknown and an additional degree of freedom $[\![\boldsymbol{u}]\!]$ is introduced as a fine–scale unknown within cracked elements such that the overall corrected displacement is $\boldsymbol{u} = \boldsymbol{d} - [\![\boldsymbol{u}]\!]$. The finite element equations for the coarse and fine scale are described next.

4.1.1 Fine scale equations

Traction continuity on the crack surface is given by:

$$\boldsymbol{t}^c = \boldsymbol{P}_r \boldsymbol{n} = T_n^c \boldsymbol{n} + T_m^c \boldsymbol{m} \tag{4.2}$$

where $\boldsymbol{t}^c$ is the nominal traction vector on the crack surface and (T_n^c, T_m^c) are the normal and tangential components of the nominal traction in the reference configuration. Here, the nominal stress $\boldsymbol{P}_r$ in the reference configuration at time t_n is expressed in terms of the Cauchy stress $\boldsymbol{\sigma}$ in the current configuration at time t_{n+1} as $\boldsymbol{P}_r = (\det \boldsymbol{F}_r)\boldsymbol{\sigma}\boldsymbol{F}_r^{-T}$.

The traction components are assumed to be linearly related to the components of

the crack displacement $[\![\boldsymbol{u}]\!]$ in the reference configuration via the softening moduli $\mathcal{H}$:

$$T_n^c = T_{n0}^c - \mathcal{H}_n[\![\boldsymbol{u}]\!] \cdot \boldsymbol{n}, T_m^c = T_{m0}^c - \mathcal{H}_m[\![\boldsymbol{u}]\!] \cdot \boldsymbol{m} \tag{4.3}$$

where $\mathcal{H}_n, \mathcal{H}_m$ are the softening moduli for the mode–I and mode–II crack, T_{n0}^c, T_{m0}^c are the critical values of normal and tangential nominal tractions that lead to the formation of a new crack. The linear tractionseparation law is shown in Fig. 4.2.

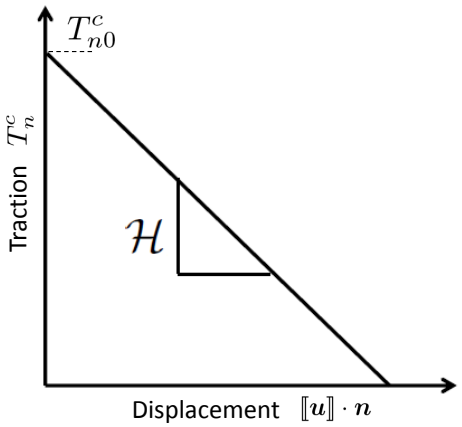

Figure 4.2: *Linear traction separation law for mode I failure.* T_{n0}^c *is the cohesive strength for the fracture mode and* $\mathcal{H}$ *is the softening moduli.*

Substituting Eq. 4.3 in Eq. 4.2, the fine scale residual $\boldsymbol{r}$ is obtained as:

$$\boldsymbol{r} \equiv (T_{n0}^c - \mathcal{H}_n([\![\boldsymbol{u}]\!] \cdot \boldsymbol{n}))\boldsymbol{n} + (T_{m0}^c - (\mathcal{H}_m[\![\boldsymbol{u}]\!] \cdot \boldsymbol{m}))\boldsymbol{m} - \boldsymbol{P}_r\boldsymbol{n} = 0 \tag{4.4}$$

Linearizing the residual with respect to the displacement unknown gives:

$$\begin{aligned}&(T_{n0}^c - \mathcal{H}_n([\![\boldsymbol{u}]\!] \cdot \boldsymbol{n}))\boldsymbol{n} + (T_{m0}^c - (\mathcal{H}_m[\![\boldsymbol{u}]\!] \cdot \boldsymbol{m}))\boldsymbol{m} - \boldsymbol{P}_r\boldsymbol{n} \\ &- \mathcal{H}_n(\delta[\![\boldsymbol{u}]\!] \cdot \boldsymbol{n})\boldsymbol{n} - \mathcal{H}_m(\delta[\![\boldsymbol{u}]\!] \cdot \boldsymbol{m})\boldsymbol{m} - (\delta\boldsymbol{P}_r)\boldsymbol{n} = 0\end{aligned} \tag{4.5}$$

Here, $\delta\boldsymbol{P}_r = \delta(\det\boldsymbol{F}_r\boldsymbol{\sigma}\boldsymbol{F}_r^{-T})$ is the increment in the nominal stress which can be

simplified as:

$$\delta \boldsymbol{P}_r = \det \boldsymbol{F}_r (tr(\delta \boldsymbol{F}_r \boldsymbol{F}_r^{-1})\boldsymbol{\sigma} + \delta\boldsymbol{\sigma} - \boldsymbol{\sigma}(\delta \boldsymbol{F}_r \boldsymbol{F}_r^{-1})^T)\boldsymbol{F}_r^{-T} \tag{4.6}$$

The increment in the Cauchy stress can be computed in an implicit form $\delta\boldsymbol{\sigma} = \mathcal{C}[\delta \boldsymbol{F}_r]$ using the crystal plasticity constitutive model as shown in appendix B. Note that the increment in deformation gradient is of the form $\delta \boldsymbol{F}_r = (\nabla_n \delta \boldsymbol{d} - \nabla_n \delta [\![\boldsymbol{u}]\!])$ which can be substituted in Eq. 4.6 such that Eq. 4.5 is obtained in terms of the unknown displacement increments. Note that $\delta \boldsymbol{d}$ is a coarse scale unknown and thus, the fine scale equation (Eq. 4.5) is solved in a coupled manner with the coarse scale equations (explained next).

Remark : The traction separation law can also be written in terms of the true traction vector $\boldsymbol{t}^{c*} = \boldsymbol{\sigma}\boldsymbol{n}^* = T^c_{n*}\boldsymbol{n}^* + T^c_{m*}\boldsymbol{m}^*$, where $\boldsymbol{n}^*$ and $\boldsymbol{m}^*$ are the crack normal and tangential directions in the current configuration. In this case, the true traction components are assumed to be linearly related to the components of the crack displacement $[\![\boldsymbol{u}]\!]$ in the current configuration. Using the relationship $\boldsymbol{n}^* = \boldsymbol{F}_r^{-T}\boldsymbol{n}$ and $\boldsymbol{m}^* = \boldsymbol{F}_r\boldsymbol{m}$ leads to several additional geometric terms (in terms of $\delta\boldsymbol{F}_r$) in the linearized residual [42]. In this work, we express the cohesive law in terms of the nominal tractions (eg. Ref. [70, 71]) to avoid this additional complexity.

4.1.2 Coarse scale equations

For any kinematically admissible test function $\tilde{\boldsymbol{u}}$, the weak form of the coarse scale virtual work equation for displacement–controlled problems in the absence of body forces is of the form:

$$\mathcal{G} \equiv \int_{\Omega_n} \boldsymbol{P}_r \cdot \nabla_n \tilde{\boldsymbol{u}} dV = 0 \tag{4.7}$$

The Newton-Raphson iterative scheme is employed to solve the above equation. The increment $d\mathcal{G}$ due to infinitesimal changes in the displacements is computed as:

$$d\mathcal{G} = \int_{\Omega_n} d\boldsymbol{P}_r \cdot \nabla_n \tilde{\boldsymbol{u}} dV \tag{4.8}$$

Note that the test function is written in terms of the coarse scale variable, $\nabla_n \tilde{\boldsymbol{u}} = \nabla_n \tilde{\boldsymbol{d}}$. In addition, the increment in the nominal stress can be written in an implicit form $d\boldsymbol{P}_r = \mathcal{C}^*[\delta \boldsymbol{F}_r] = \mathcal{C}^*[\nabla_n \delta \boldsymbol{d} - \nabla_n \delta [\![\boldsymbol{u}]\!]]$ using equation 4.6. Thus, the linearized coarse scale equation reduces to:

$$\int_{\Omega_n} \boldsymbol{P}_r \cdot \nabla_n \tilde{\boldsymbol{d}} dV + \int_{\Omega_n} \mathcal{C}^*[\nabla_n \delta \boldsymbol{d} - \nabla_n \delta [\![\boldsymbol{u}]\!]] \cdot \nabla_n \tilde{\boldsymbol{d}} dV = 0 \tag{4.9}$$

4.1.3 Coupled solution procedure

Let $\boldsymbol{u}_{n+1}^k$ be the displacement field at the k^{th} iteration, then the linearized equations are solved for the increments $\delta \boldsymbol{u} = \boldsymbol{u}_{n+1}^{k+1} - \boldsymbol{u}_{n+1}^k$. The analysis procedure involves the solution of two coupled equations for the increments in coarse scale $\delta \boldsymbol{d}$ and the fine scale displacement $\delta [\![\boldsymbol{u}]\!]$.

Let $\nabla_n \tilde{\boldsymbol{d}} = \boldsymbol{B_d}\{\tilde{\boldsymbol{d}}\}$, $\nabla_n \delta \boldsymbol{d} = \boldsymbol{B_d}\{\delta \boldsymbol{d}\}$ and $\nabla_n \delta [\![\boldsymbol{u}]\!] = \boldsymbol{G}\{\delta [\![\boldsymbol{u}]\!]\}$ denote the gradients in terms of finite element matrices ($\boldsymbol{B_d}$ and $\boldsymbol{G}$) and the nodal unknowns. Each NR step involves solving for increments $\boldsymbol{\delta d}, \boldsymbol{\delta [\![u]\!]}$ using the system of equations given below:

$$\begin{bmatrix} \boldsymbol{K}_{\bar{u}\bar{u}} & \boldsymbol{K}_{\bar{u}u'} \\ \boldsymbol{K}_{u'\bar{u}} & \boldsymbol{K}_{u'u'} \end{bmatrix} \begin{bmatrix} \delta \boldsymbol{d} \\ \delta [\![\boldsymbol{u}]\!] \end{bmatrix} = \begin{bmatrix} -\mathcal{G} \\ \boldsymbol{r} \end{bmatrix} \tag{4.10}$$

where,

$$\boldsymbol{K}_{\bar{u}\bar{u}} = \int_{\Omega_n} \boldsymbol{B_d}^T \mathcal{C}^* \boldsymbol{B_d} dV \tag{4.11}$$

$$\boldsymbol{K}_{\bar{u}u'} = -\int_{\Omega_n} \boldsymbol{B_d}^T \mathcal{C}^* \boldsymbol{G} dV \tag{4.12}$$

$$\boldsymbol{K}_{u'\bar{u}} = \boldsymbol{H}^T \mathcal{C}^* \boldsymbol{B_d} \tag{4.13}$$

$$\boldsymbol{K}_{u'u'} = -\boldsymbol{H}^T \mathcal{C}^* \boldsymbol{G} + \mathcal{H}_n \boldsymbol{n} \otimes \boldsymbol{n} + \mathcal{H}_m \boldsymbol{m} \otimes \boldsymbol{m} \tag{4.14}$$

where, $\boldsymbol{H}$ is a matrix computed by rearranging the component of the crack normal $\boldsymbol{n}$. In our implementation, for example, $\boldsymbol{H} = \begin{bmatrix} n_x & 0 \\ n_y & 0 \\ 0 & n_x \\ 0 & n_y \end{bmatrix}$, where n_x and n_y are the components of the crack normal $\boldsymbol{n}$.

4.1.4 Finite element representation of cracks

The present implementation employs three noded triangular elements. The coarse scale displacement $\boldsymbol{d}$ is interpolated using the usual linear shape functions $[N^1, N^2, N^3]$ for the triangle element. The fine scale unknown $[\![\boldsymbol{u}]\!]$ is interpolated using a specially constructed shape function that ensures that the displacement jump is localized to the element. The fine scale shape function can be considered to be the difference between a linear shape function and a heaviside jump function centered at the crack. Two possible cases of such a shape function are shown in Fig. 4.3. One of these two shape functions are chosen by comparing the outward normal direction of the element edge not intersected by the crack and the normal direction of the discontinuity within the

element. In the first case shown in Fig 4.3(a), $\boldsymbol{n}$ and $\boldsymbol{n}^1$ point in the same direction and the shape function is the difference between N_1 and a heaviside function. The second case in Fig. 4.3(b), $\boldsymbol{n}$ and $\boldsymbol{n}^1$ point in the opposite directions and the shape function is the difference between $(1 - N_1)$ and a heaviside function.

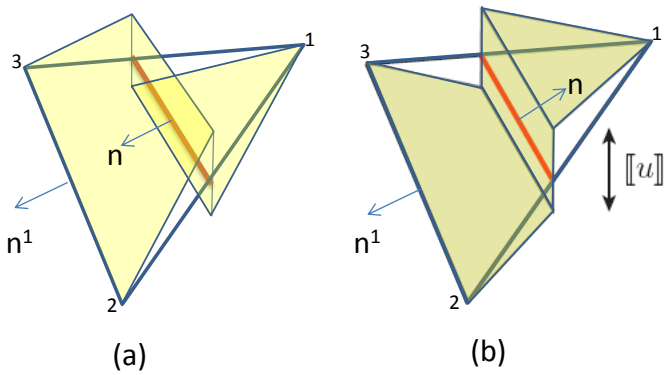

Figure 4.3: *Shape functions for fine scale interpolation: Two cases are possible by comparing the outward normal direction of the element edge not intersected by the crack and the normal direction of the discontinuity within the element. (a)* $\boldsymbol{n}$ *and* $\boldsymbol{n}^1$ *point in the same direction: The shape function is the difference between* N_1 *and a heaviside function centered at the crack. (b)* $\boldsymbol{n}$ *and* $\boldsymbol{n}^1$ *point in the opposite directions: The shape function is the difference between* $(1-N_1)$ *and a heaviside function centered at the crack.*

When using this description, the gradient of the fine scale displacement (written in a vector format) is written using the finite element shape functions as,

$$\nabla_n \delta[\![\boldsymbol{u}]\!] = \pm \underbrace{\begin{bmatrix} \frac{dN^i}{dx} & 0 \\ \frac{dN^i}{dy} & 0 \\ 0 & \frac{dN^i}{dx} \\ 0 & \frac{dN^i}{dy} \end{bmatrix}}_{\boldsymbol{G}} \{\delta[\![\boldsymbol{u}]\!]\} \tag{4.15}$$

where, $\{\delta[\![\boldsymbol{u}]\!]\}$ is a 2×1 unknown vector for each cracked element. In this equation, index i corresponds to the node common to the element edges intersected by the crack. The correct sign of $\boldsymbol{G}$ is determined by the choice of one of the two shape

functions shown in Fig. 4.3. When using the shape function shown in Fig 4.3(a), a positive sign is used for $\boldsymbol{G}$. If the shape function defined in Fig 4.3(b) is used, a negative sign is employed. In addition, the crack normals ($\boldsymbol{n}$) in all the elements forming a contiguous crack are aligned to the same side of the crack path so that the discontinuity is consistent across these elements.

4.2 Constitutive modeling of single crystal response

A rate independent crystal plasticity theory ([72]) which is the same as Section 2.3 and Section 3.2 is used to model deformation response of particles within each grain. The algorithm for computing the plastic shear increment $\Delta\gamma^{\beta}$ from this model be found in the appendix A. Finally, the tangent modulus $\frac{\partial \boldsymbol{\sigma}}{\partial \boldsymbol{F}}$ for use in the weak form is computed using a fully implicit algorithm described in appendix B.

4.3 Constitutive model in macroscopic regions

Microstructural effects become important at regions of stress concentrators such as notches, cracks and contact surfaces. A multiscale model the same as Chapter III is employed that efficiently captures microstructural details at such critical regions. The approach is based on a multiresolution mesh that includes an explicit microstructure representation at critical regions where stresses are localized. At regions farther away from the stress concentration, a reduced order model that statistically captures the effect of microstructure is employed. The configuration of the multiscale model is shown in Fig. 4.4.

4.4 Numerical examples

We consider planar polycrystals characterized by a two dimensional rotation $\boldsymbol{R}$ that relates the local crystal lattice frame to the reference sample frame. A parametriza-

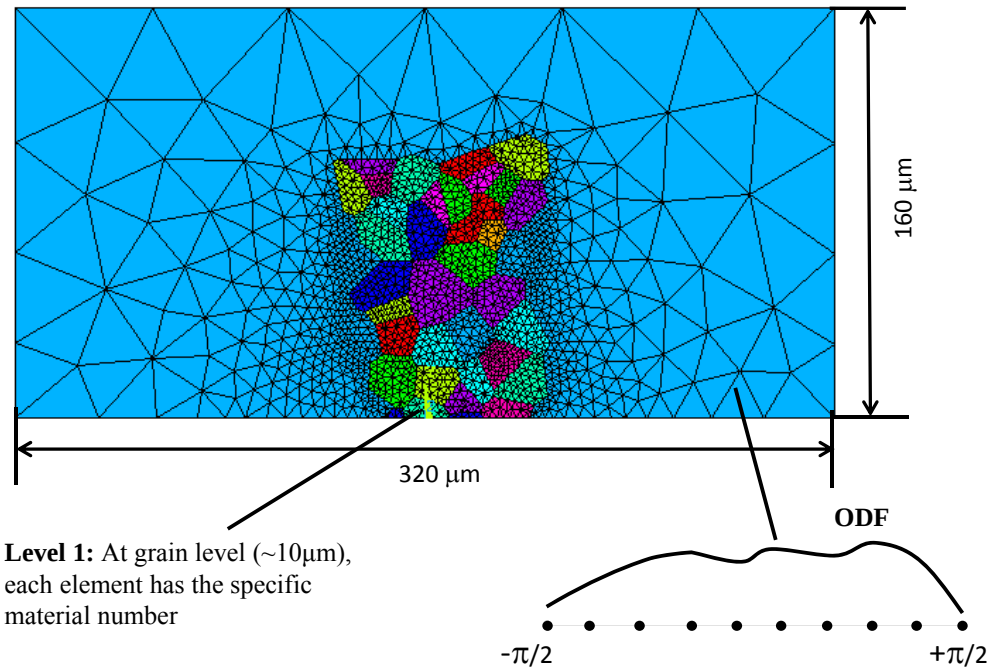

Figure 4.4: *The configuration of multiscale model. The model is divided into two scales. Microscale is a critical area where crack propagates. It contains explicit representation of crystals with assigned orientations. Macroscale element has an underlying ODF in each of the integration points that probabilistically represents hundreds of crystals.*

tion of the associated rotation group is,

$$\boldsymbol{R} = \boldsymbol{I}cos(g) - \boldsymbol{E}sin(g) \tag{4.16}$$

where g is the angle between the crystal and sample axes, $\boldsymbol{E}$ is the two dimensional alternator ($E_{11} = E_{22} = 0, E_{12} = -E_{21} = 1$), and $\boldsymbol{I}$ is the identity tensor. A general planar crystal with symmetry under rotations through π is considered here. Under the symmetry, crystal orientations can be described uniquely by parameters drawn from a simply connected fundamental region $(0, \pi)$. Due to symmetry, the orientation 0 is exactly the same as orientation π. During the peristatic simulation, the crystal reorientation velocity ($\boldsymbol{v} = \frac{\partial \boldsymbol{g}}{\partial t}$) is obtained by taking a derivative of relation Eq.

5.10:

$$\boldsymbol{v} = \frac{1}{2} E.\Omega \tag{4.17}$$

where $\boldsymbol{\Omega}$ is the spin tensor defined as $\boldsymbol{\Omega} = \dot{\boldsymbol{R}}^e \boldsymbol{R}^{eT}$. Here, $\boldsymbol{R}^e$ is evaluated through the polar decomposition of the elastic deformation gradient $\boldsymbol{F}^e$ as $\boldsymbol{F}^e = \boldsymbol{R}^e \boldsymbol{U}^e$. The texturing of the polycrystal is tracked by computing the change in orientation $\Delta \boldsymbol{g} = \boldsymbol{v} \Delta t$ of crystals at each time step. Using $\Delta \boldsymbol{g}$, the Jacobian J_F can be computed for evolving the ODF in Eq. 2.6.

For modeling the single crystal response, two slip systems at orientations $-\pi/6$ and $+\pi/6$ were considered. The values in the elastic stiffness matrix are taken as $\mathbb{C}_{11} = 2\ GPa$ and $\mathbb{C}_{12} = \mathbb{C}_{44} = 1\ GPa$. The particular hardening law in Eq. 3.1 was chosen as follows:

$$h^{\alpha\beta} = h_o^\beta (q + (1-q)\delta^{\alpha\beta})(1 - \frac{s^\beta(t)}{s_s^\beta})^a \text{ (no sum on } \beta) \tag{4.18}$$

The slip system hardening term ($h^{\alpha\beta}$) includes latent hardening through parameter q. In this term, h_o^β is the hardening coefficient and s_s^β is the saturation resistance of slip system β. The values for the slip hardening parameters are taken to be identical for both slip systems and are listed below:

$$h_o = 20 \text{ MPa}, s_s = 200 \text{ MPa}, a = 2, \tau_0 = 20 \text{ MPa}, q = 1.4 \tag{4.19}$$

In order to find the direction of crack growth, we assume that the crack grows perpendicular to the direction of maximum tensile stress motivated by recent micro–scale experiments in [73]. However, instead of searching for the maximum tensile stress direction in the immediate vicinity of the crack tip, a non–local criteria is employed [69]. This involves finding the angle along which the 'averaged' tensile stress over a finite distance ahead of the crack tip is the largest. Since VMCM is an element–

based method, we search across multiple elements ahead of the crack tip. The search is performed along the same angle but from start points at the center of each element edge encountered along the path as shown in Fig. 4.5. Once the direction of maximum tensile stress is found, all elements along this path whose tensile stress exceeds the critical normal tractions are chosen and the fine–scale variable $[\![\boldsymbol{u}]\!]$ is augmented. Subsequently, both the normal and shear tractions in these elements are controlled using the traction separation laws in Eq. 4.3. The loading displacement is maintained at the same value and the system is re–equilibrated. After re–equilibration, the direction of crack propagation is again searched from the location of the new crack tip, without increasing the loading displacement. More crack elements are assigned on elements whose tensile stress exceeds the critical normal traction. The next loading step is applied only after no more cracks can form in the previous loading stage. In the case of failure of elasto–plastic elements, we assume that once the crack has formed, we assume that the element begins to unload following an elastic unloading curve with the initial elastic modulus as shown in Fig. 4.5(b).

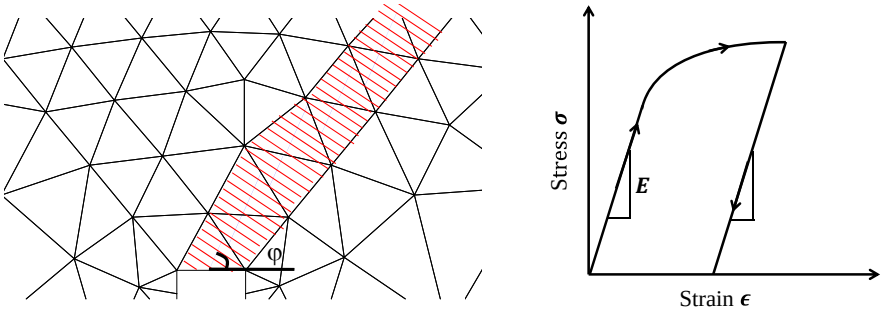

Figure 4.5: *Aspects of the numerical implementation (a) The crack path searching method employed involves searching over a finite distance ahead of the crack tip for the angle along which the average tensile stress is the largest. In the implementation, the search is done across several elements ahead of the crack tip in the same direction but from start points at the center of the element edge. (b) After the crack is formed in an elastoplastic element, the unloading is assumed to be elastic following the initial elastic modulus.*

4.4.1 Isotropic Model Tests

In the numerical examples, we consider the case of a homogeneous material (without explicit representation of grains) to study mesh convergence and to compare with results published in literature. To model the isotropic material, an uniform ODF corresponding to a random microstructure, with all orientations equally weighted, is employed.

A tensile linear elastic specimen is first simulated to test the convergence of the approach (in mode–I) as shown in Fig. 4.6(a). Plasticity is switched off by assigning a very high critical resolved shear stress for activation of slip systems. A loading displacement in the x–direction is imposed on the right edge. Isotropic stiffness matrix constants corresponding to the random ODF are $C_{11} = 2.25\ GPa$ and $C_{12} = C_{44} = 0.75\ GPa$. The cohesive strength T^c_{n0} is taken as 10 MPa and 10 MPa and $\mathcal{H}_n$ is 0.25 GPa/mm. Figure 4.6 shows the plane stress problem and the resulting crack paths for different mesh densities – for unstructured grids with 442, 700, 930 and 2500 elements respectively. The corresponding elastic load displacement curve is in Fig. 4.6(b). In order to compare with Ref. [44], the P and Δ have been normalized with $P_o = 20MPa$ and $\Delta_o = 0.2mm$. The result in Fig. 4.6(b) indicates that the load–displacement response does not show any significant mesh dependency for the two cases considered and the result is indeed identical to that published in literature [44]. Fig. 4.6(c,d) shows the crack paths for the two meshes used. The displacement contours are also plotted. It can be seen that the right half carries all the displacements at this point while the displacement varies along the crack path.

In order to verify that the approach indeed gives the correct crack trajectory for an *elasto–plastic* case, a three point bending test was employed as shown in Fig. 4.7(a). Plasticity was switched on using an initial critical resolved shear stress of $\tau_0 = 20$ MPa for both slip systems. Two cases were simulated, the first one involves a centrally located loading (Fig. 4.7(a)) and the other, an eccentric loading at the

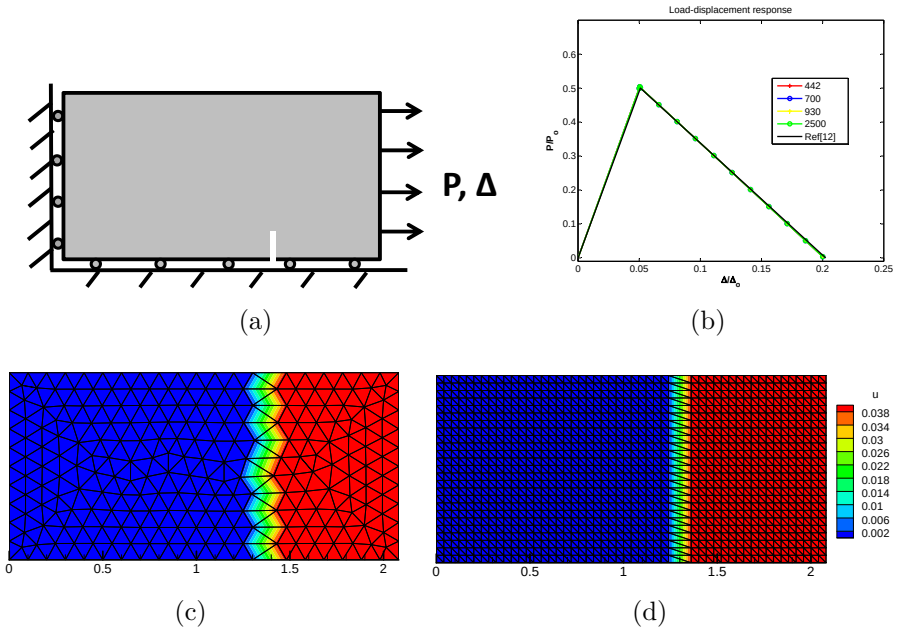

Figure 4.6: *(a) Simple tension test configuration (b)Load–displacement response of the straight crack propagation, the y axis load P, the δ is the displacement. The P and Δ values have been normalized with fixed reference values P_o and Δ_o. (c)Displacement magnitude contour for 442 unstructured meshes. (d) Displacement magnitude contour for 2500 structured meshes. It can be seen the left half of the model has no displacement, while the right half has the identical displacement. Displacement varies along the crack path.*

top surface (Fig. 4.7(b)). An initial notch was specified at the center bottom surface in order to nucleate the crack. In the case of three–point bending, the crack is expected to propagate towards the point of application of force at the top surface of the specimen. As seen from Fig. 4.7(c,d), the overall crack direction is indeed predicted as moving towards the point of application of the loading in both cases. Note that for a better visualization of the crack path, the crack path elements are removed from the simulation images shown in Fig. 4.7(c,d).

4.4.2 Polycrystals: Tensile test with intergranular failure mode

Here, the entire computational region is divided into two levels: macro-scale (ODF–based) and micro-scale. At the micro-scale, aggregates of grains are explicitly modeled to track propagation of cracks. A voronoi tessellation approach was used

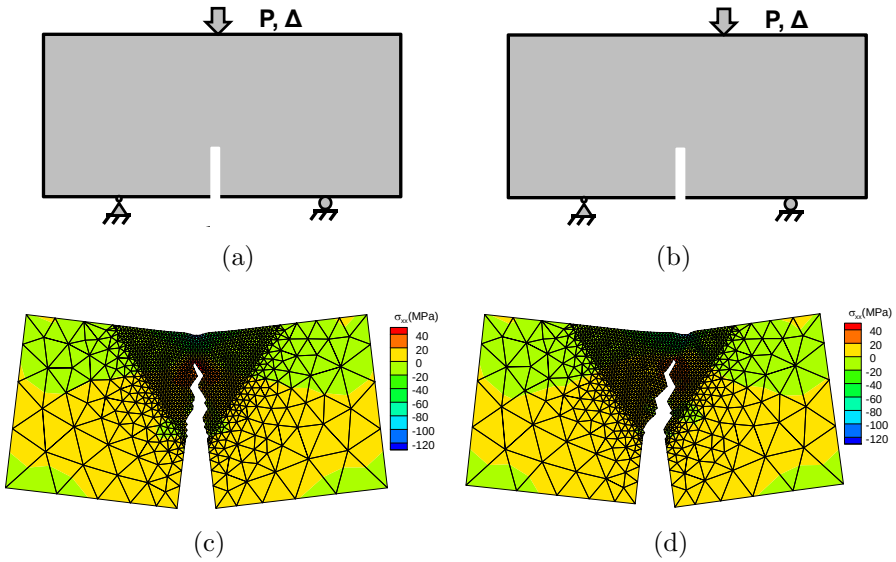

Figure 4.7: *(a) 3 points configuration with central loading (b) Central 3 points elasto-plastic bending for 2226 elements (c) 3 points configuration with eccentric loading (d) Eccentric 3 points elasto-plastic bending for 2226 elements*

to build a polycrystalline microstructure and random orientations were assigned to each crystal. The mesh used in this work is shown in Fig. 4.8(a) with the color of each grain mapping to a particular crystal orientation from 0 to π radians. There is a gradual transition of mesh density from microscale to the macroscale wherein the far field elements are much bigger than the microscale elements. The loading and boundary conditions used in these examples are same as those shown in Fig. 4.6 and Fig. 4.7 corresponding to a tensile test and a three point bending test respectively.

In these simulations, the crack is initiated by specifying a starting element along a grain boundary. The crack is advanced in the microstructural region and the simulation is stopped when the crack reaches the macro–scale element. Since VMCM is an element–based method and there are no special interface elements involved, the grain boundaries are represented by choosing elements to one side of the grain boundary with the crack normals assigned to be parallel to the grain boundary normal. The values of critical traction components for the grain boundary elements T^c_{n0} and T^c_{m0} were picked as 30 MPa and 5 MPa and softening moduli for normal and tangential

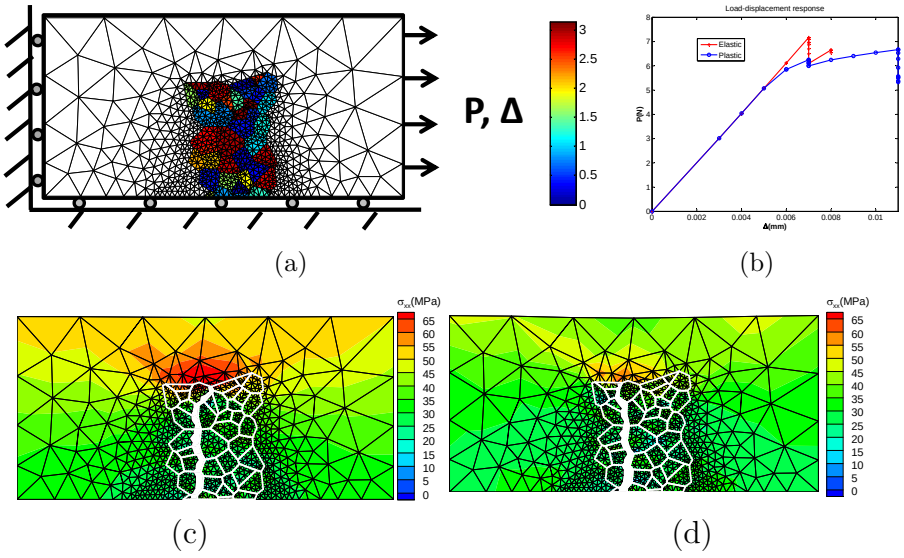

Figure 4.8: *Tensile convergence test for polycrystalline crack propagation. (a) boundary condition of loaded specimen, (b) Load displacement response (c) σ_{xx} contours for elastic (d) plastic simulations. The crack path of plastic is different at the end of the crack path. This happens due to different response of elastic and plastic calculation.*

directions are 30 GPa/mm and 2.5 GPa/mm to ensure that the crack forms at a critical displacement of $1\mu m$. The critical stresses for the grain interior elements are much higher such that only the grain boundary elements fail. The simulation stops when the crack reaches the macroscale element.

The critical normal stress employed is the same for both the elastic and the elasto–plastic case. The P–Δ response for the tensile test case in Fig. 4.8(b) shows that the elastic case failed earlier than the plastic case and the crack grew in two discrete increments. In the elastic case shown in Fig. 4.8(c), the crack propagation continued at the same loading step (displacement corresponding to the first large drop in the P–Δ response) until the triple junction is reached. At the triple junction, the crack paused until the next loading step wherein the stresses exceed the critical normal traction in one of the grain boundaries leading to the next large drop in the P–Δ response. The elastoplastic case (Fig. 4.8(d)) follows the identical crack trajectory until the triple junction, beyond which another grain boundary branch is chosen. In

the elastoplastic case, the specimen can be loaded to a much larger displacement for the same crack length. The progression of cracking is slower and only a few grain boundaries fail when the critical stress is first reached at the same critical displacement as the elastic case. Subsequently, the specimen takes up a large displacement loading following an elasto–plastic loading curve until all the grain boundaries fail in the final loading step when the critical stresses are again achieved leading to a sharp drop in the P–Δ response.

VMCM approach gives us the ability to simulate arbitrary crack paths within the polycrystal. This ranges from intergranular cracks following the grain boundaries to transgranular cracks following the interior of the grains. In addition, features like crack branching can be simulated. In the above example, when the crack reaches a triple junction along one of the grain boundaries, tensile stresses of elements along the other two grain boundaries are compared. If normal traction along one direction is much higher than those along the other direction, the former boundary is chosen for the crack to advance. Fig. 4.9(b) shows a case where both grain boundaries at a triple junction exceed the critical stress level in which case, the method simulates crack branching. In addition, by giving comparable critical stresses to grain boundaries as well as the elements in the grain interior, one can expect a transition to transgranular failure mode as shown in the next example.

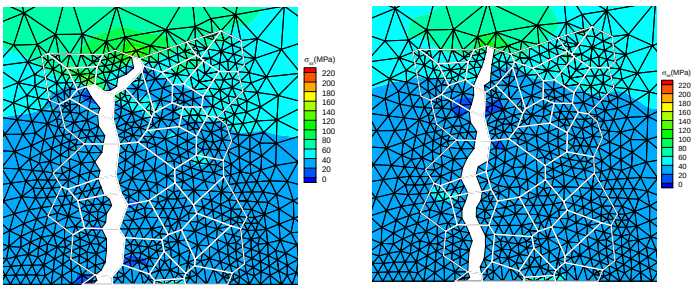

(a) (b)

Figure 4.9: *(a) Branching of a crack at a triple junction. (b) Intergranular to transgranular crack transition.*

4.4.3 Polycrystals: Three point bending test with intergranular to transgranular transition

In this example, a three–point bending test was chosen with the same mesh as in the previous example. Two simulations were performed. In the first case, the critical stresses for the grain interior elements are much higher such that only the grain boundary elements fail. In the second case, elements in the grain interior were given critical traction values comparable with those for the grain boundary elements to test conditions when the crack transitions from intergranular to transgranular mode.

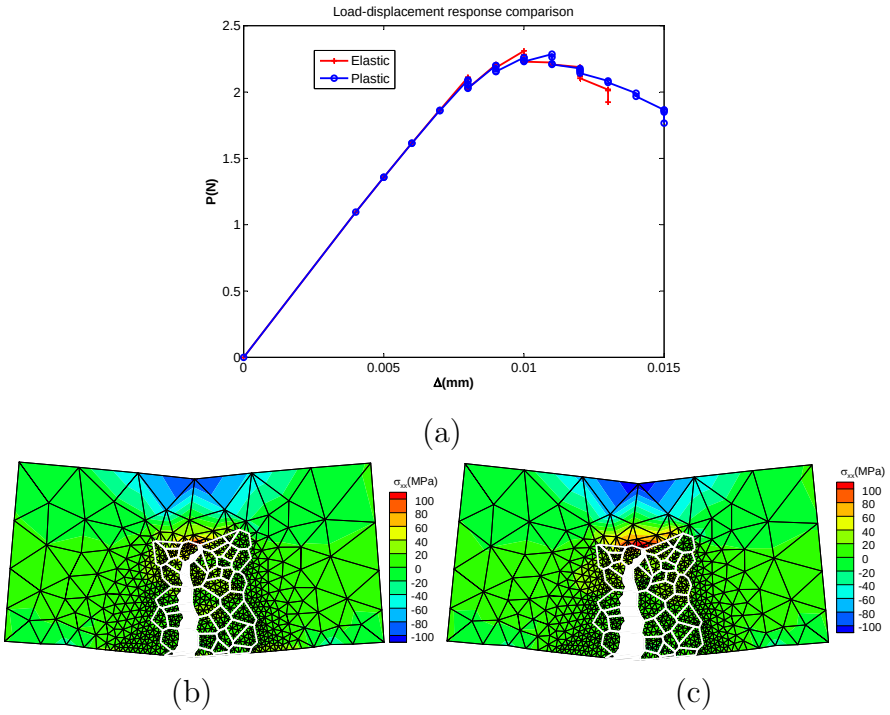

Figure 4.10: *Three point bending simulations for polycrystalline intergranular crack propagation. Figures are (a) force displacement curve (b,c) σ_{xx} contours for elastic and plastic response.*

A crack in the three point bending case was initiated by assigning a start element at the bottom edge of the bar. The P–Δ response for the three–point bending test in the intergranular failure mode is shown in Fig. 4.10(a) and shows more softening and progressive failure response compared to the tensile test case in Fig. 4.8(b). Fig.

4.10(b,c) shows the intergranular failure mode in the elastic and elastoplastic case respectively. Compared to the elastic case, the elastoplastic failure tends to show a larger fracture toughness and a larger displacement to failure as expected. There was no crack branching observed in either case.

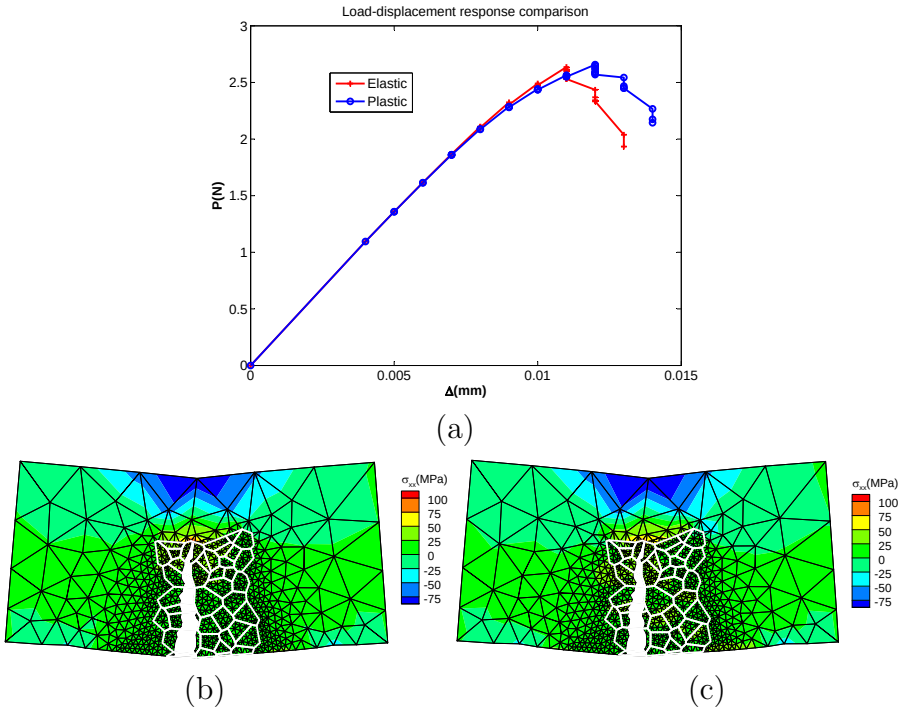

Figure 4.11: *Three point bending simulations for inter and transgranular polycrystalline crack propagation. (a) force displacement curve (b) σ_{xx} contours for elastic (c) plastic response.*

The second case that allows transition from intergranular to transgranular crack is illustrated in Fig. 4.11(b,c). The critical values T^c_{n0} and T^c_{m0} for elements in the grain interior were picked as 40 MPa and 10 MPa. These values were higher than the grain boundaries, which implies that the crack starts in the intergranular failure mode. However, as the crack reaches a triple junction, it is seen that the transgranular mode becomes favorable. In the transgranular mode of crack propagation, the crack propagated perpendicular to the direction of maximum normal traction. When the transgranular crack reached another grain boundary with an easier propensity to form

a crack, the crack transitioned back to intergranular mode. The crack paths in the elastic and elastoplastic cases were different. In the elastic case, the crack showed an increasing tendency to follow the grain boundary. The P–Δ response in Fig. 4.11(a) again shows that the crack is formed at a slower rate in the plastic case but the increments in the crack length were similar in both the elastic and elastoplastic cases.

A comparison of the P–Δ response of a purely intergranular mode in Fig. 4.8(a) and a combination of inter– and trans–granular modes in Fig. 4.11(a) in the elasto–plastic case reveals several interesting features. The failure is faster when transgranular paths are available for the crack even though the critical stresses for these paths were higher. Further, the crack tends to form in fewer steps and more abruptly when transgranular modes are available. This aspect is especially seen when a crack reaches a triple junction, where a transgranular mode becomes more favorable for the crack to propagate to the next grain boundary rather than wait for the stresses to exceed the critical tractions in the grain boundaries of the triple junction.

4.5 Conclusions

Modeling failure at microstructural scales is valuable for predictive modeling of component life, and ensuring structural integrity in aerospace structures. In this paper, the recently developed variational multiscale cohesive method (VMCM) is used to model crack propagation in polycrystalline materials. In this approach, the discontinuous displacement field in the crack is regarded as a fine scale degree of freedom and is added to elements that exceed the critical values of normal or tangential traction during loading. This additional degree of freedom is represented within the cracked element using a special discontinuous shape function that ensures that the displacement jump is localized to that particular element. The finite element formulation and code implementation details were presented. Compared to traditional cohesive zone modeling approaches, the method does not require the use of any special interface

elements in the microstructure.

Since failure is usually localized at regions of stress concentrators such as notches, cracks and contact surfaces, a multiscale model is developed in this work which is based on a multiresolution mesh. The model includes an explicit microstructure representation at critical regions, while at regions farther away from the stress concentration, a reduced order model that statistically captures the effect of microstructure is employed. To demonstrate applicability of the methodology, a polycrystalline grain structure was monotonically loaded in tension and three–point bending modes. The primary contribution in this work is to demonstrate the use of the methodology in predicting crack growth paths that are arbitrary (transitions from intergranular to transgranular paths and vice versa). In VMCM method, the crack path is computed on the fly during the simulation and thus, arbitrary crack paths can be simulated. Both elastic and elastoplastic cases were compared, and the inclusion of crystal plasticity leads to increased fracture toughness and more progressive failure over a larger number of loading steps compared to the elastic case. By controlling the critical normal stress for the grain boundary elements and the elements in the grain interior, transitions from intergranular to transgranular failure modes can be simulated.

CHAPTER V

A Peristatic Implementation of Crystal Plasticity

[1]In this chapter, a implicit quasi–static implementation of the theory termed 'peristatics' is introduced. Unlike peridynamics [55], peristatics does not include inertial terms and the solution procedure uses Newton–Raphson iterations similar to a non–linear finite element implementation. Thus, peristatic results can be quantitatively compared to conventional quasi–static crystal plasticity finite element simulations. The governing equations of the peristatic theory and peristatic results for shear band localization in a polycrystal in tension and shear modes were compared in this Chapter. Section 5.1 and Section 5.2 of this chapter provide the governing equations of the peristatic theory and its numerical implementation. In Section 5.3, the method is compared with crystal plasticity finite element simulations and demonstrate the ability of peristatic model to capture fine shear bands in grains. In the final section, conclusion is discussed.

5.1 Peristatic theory

In peristatic theory, a material point $\boldsymbol{x}$ in the reference configuration $\mathcal{B}$ is assumed to interact with neighboring points $\boldsymbol{x'}$ located within a finite radius δ. The position of

[1]Reproduced from S. Sun and V. Sundararaghavan. "A Peristatic Implementation of Crystal Plasticity", International Journal of Solids and Structures, in review. 2014. [74]

particle $\boldsymbol{x}$ in the current configuration is denoted by $\boldsymbol{y} = \boldsymbol{x} + \boldsymbol{u_x}$, where $\boldsymbol{u_x}$ denotes the displacement of particle $\boldsymbol{x}$. The kinematics of peristatic theory is shown in Fig. 5.1.

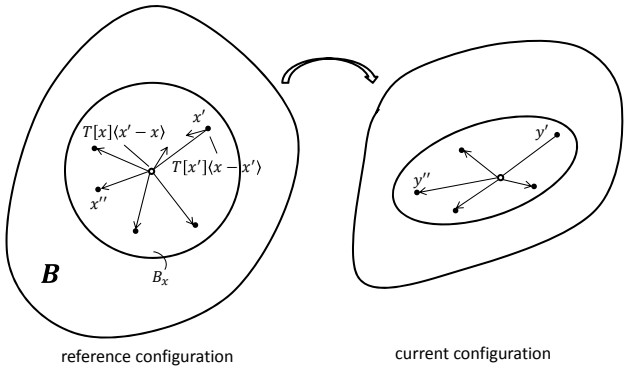

Figure 5.1: *Kinematics of peristatic theory: Particle $\boldsymbol{x}$ is bonded to all particles within a region $\mathcal{B}_x$. Particle $\boldsymbol{x}$ maps to particle $\boldsymbol{y}$ in the deformed configuration. An averaged deformation gradient tensor can be defined that maps the bonds in the reference configuration to the deformed configuration. This quantity is used in the crystal plasticity constitutive model. The stresses obtained from the constitutive model can be mapped to bond force states $\boldsymbol{T}\left[\boldsymbol{x}\right]\left\langle \boldsymbol{x}' - \boldsymbol{x}\right\rangle$ in the reference configuration.*

The peristatic equation of balance of linear momentum at time t for the point $\boldsymbol{x}$ is given by ([55])

$$\begin{aligned} \boldsymbol{L}(\boldsymbol{x}) + \boldsymbol{b}(\boldsymbol{x}) = 0 \quad \forall x \in \mathcal{B}, \\ \boldsymbol{L}(\boldsymbol{x}) = \int_{\mathcal{B}_x} \left\{ \boldsymbol{T}\left[\boldsymbol{x}\right]\left\langle \boldsymbol{x}' - \boldsymbol{x}\right\rangle - \boldsymbol{T}\left[\boldsymbol{x}'\right]\left\langle \boldsymbol{x} - \boldsymbol{x}'\right\rangle \right\} dV_{x'} \end{aligned} \tag{5.1}$$

where $\boldsymbol{b}$ is the body force, $\mathcal{B}_x$ is a spherical neighborhood of radius δ centered at $\boldsymbol{x}$ at time $t = 0$. The term $\boldsymbol{T}\left[\boldsymbol{x}\right]\left\langle \boldsymbol{x}' - \boldsymbol{x}\right\rangle$ denotes the force (per unit volume squared) on material point $\boldsymbol{x}$ operating on the bond $\boldsymbol{x}' - \boldsymbol{x}$. The value of $\boldsymbol{T}$ can be obtained from the first Piola-Kirchhoff stress, $\boldsymbol{P}$, computed at point $\boldsymbol{x}$ from any conventional constitutive model (eg. of the form $\boldsymbol{P} = \mathcal{F}(\boldsymbol{F})$, where $\boldsymbol{F}$ is the deformation gradient)

as follows ([55]):

$$\boldsymbol{T}\left[\boldsymbol{x}\right]\left\langle \boldsymbol{x'}-\boldsymbol{x}\right\rangle =\omega\boldsymbol{P}\boldsymbol{K}^{-1}(\boldsymbol{x'}-\boldsymbol{x}) \tag{5.2}$$

where, ω is an *influence function* defined at particle $\boldsymbol{x}$ which weights the contribution from each neighbor $\boldsymbol{x'}$ (for eg. based upon the initial bond length $\omega=\hat{\omega}(|\boldsymbol{x}-\boldsymbol{x'}|)$) and $\boldsymbol{K}$ denotes a symmetric *shape tensor*, defined as

$$\boldsymbol{K}=\int_{\mathcal{B}_x}\omega(\boldsymbol{x'}-\boldsymbol{x})\otimes(\boldsymbol{x'}-\boldsymbol{x})dV_{x'} \tag{5.3}$$

The deformation gradient $\boldsymbol{F}$ (defined with respect to $\mathcal{B}$) at time t as needed in the constitutive models can be computed from the deformation of bonds attached to material point $\boldsymbol{x}$ as follows (Silling 2007b [55]):

$$\boldsymbol{F}=\left(\int_{\mathcal{B}_x}\omega(\boldsymbol{y'}-\boldsymbol{y})\otimes(\boldsymbol{x'}-\boldsymbol{x})dV_{x'}\right)\boldsymbol{K}^{-1} \tag{5.4}$$

The derivation of equations 5.2 and 5.4 can be found in Section 18 of [55] where it is also shown that these definitions ensure the balance of angular momentum.

5.2 Numerical implementation

By dividing the body $\mathcal{B}$ into numbers of cells, each represented by a particle, the integral expressions can be rewritten as a summation of discrete equations. For example, Eq. 5.1 is written as (neglecting body forces $\boldsymbol{b}$):

$$\boldsymbol{L}(\boldsymbol{x})=\sum_{i=1}^{N}\left\{\boldsymbol{T}\left[\boldsymbol{x}\right]\left\langle \boldsymbol{x}_i'-\boldsymbol{x}\right\rangle -\boldsymbol{T}\left[\boldsymbol{x}_i'\right]\left\langle \boldsymbol{x}-\boldsymbol{x'}_i\right\rangle \right\}\Delta V_{x_i'}=0 \tag{5.5}$$

where N is the number of the neighbor particles of material point $\boldsymbol{x}$ and the volume occupied by each particle is $\Delta V_{x_i'}$. To solve non-linear equation $\boldsymbol{L}\left(\boldsymbol{x}\right)=\boldsymbol{0}$, a Newton

Raphson iterative scheme is employed that solves for the increment in the particle displacements ($\delta \boldsymbol{u}_p$) using the following equation:

$$\mathcal{J}\delta \boldsymbol{u}_p = -\boldsymbol{L}(\boldsymbol{x}) \tag{5.6}$$

where, the right hand side is the residual vector and the Jacobian matrix $\mathcal{J} = \frac{\partial \boldsymbol{L}}{\partial \boldsymbol{u}_p}$ is defined implicitly by taking a derivative of Eq. 5.5 with respect to the vector of particle displacements:

$$d\boldsymbol{L}\left(\boldsymbol{x}\right) = \left[\sum_{i=1}^{N}\left(\frac{\partial \boldsymbol{T}\left[\boldsymbol{x}\right]\langle \boldsymbol{x}_i' - \boldsymbol{x}\rangle}{\partial \boldsymbol{u}_p} - \frac{\partial \boldsymbol{T}\left[\boldsymbol{x}_i'\right]\langle \boldsymbol{x} - \boldsymbol{x}_i'\rangle}{\partial \boldsymbol{u}_p}\right)\Delta V_{x_i'}\right]\delta \boldsymbol{u}_p = \mathcal{J}\delta \boldsymbol{u}_p \tag{5.7}$$

Using the tangent modulus $\frac{\partial \boldsymbol{P}}{\partial \boldsymbol{F}}$ obtained from a constitutive model (eg. crystal plasticity), the derivative of $\boldsymbol{T}$ can be written using Eq. 5.2 as:

$$\frac{\partial \boldsymbol{T}[\boldsymbol{x}]\langle \boldsymbol{x'} - \boldsymbol{x}\rangle}{\partial \boldsymbol{u}_p} = \frac{\partial \boldsymbol{T}[\boldsymbol{x}]\langle \boldsymbol{x'} - \boldsymbol{x}\rangle}{\partial \boldsymbol{F}}\frac{\partial \boldsymbol{F}}{\partial \boldsymbol{u}_p} = \omega \frac{\partial \boldsymbol{P}}{\partial \boldsymbol{F}}\frac{\partial \boldsymbol{F}}{\partial \boldsymbol{u}_p}\boldsymbol{K}^{-1}(\boldsymbol{x'} - \boldsymbol{x}) \tag{5.8}$$

Using the above expression and the definition for $\boldsymbol{F}$ from Eq. 5.4, $d\boldsymbol{L}\left(\boldsymbol{x}\right)$ can be written as follows:

$$\begin{aligned} d\boldsymbol{L}\left(\boldsymbol{x}\right) = &\sum_{i=1}^{N}\left[\left(\omega_i \frac{\partial \boldsymbol{P}}{\partial \boldsymbol{F}}\left(\sum_{j=1}^{N}\omega_j(\delta \boldsymbol{u}_{x_j'} - \delta \boldsymbol{u}_x)\otimes(\boldsymbol{x}_j' - \boldsymbol{x})\boldsymbol{K}^{-1}\Delta V_{x_j'}\right)\right)\boldsymbol{K}^{-1}(\boldsymbol{x}_i' - \boldsymbol{x})\Delta V_{x_i'}\right] \\ -\sum_{i=1}^{N}&\left[\left(\omega_i' \frac{\partial \boldsymbol{P}'}{\partial \boldsymbol{F}'}\left(\sum_{j=1}^{N'}\omega_j'(\delta \boldsymbol{u}_{(x_i')_j'} - \delta \boldsymbol{u}_{x_i'})\otimes((\boldsymbol{x}_i')_j' - \boldsymbol{x}_i')\boldsymbol{K'}^{-1}\Delta V_{(x_i')_j'}\right)\right)\boldsymbol{K'}^{-1}(\boldsymbol{x} - \boldsymbol{x}_i')\Delta V_{x_i'}\right] \end{aligned} \tag{5.9}$$

The following notation is used in the above equation:

1. $\boldsymbol{x}_i'$ is the i^{th} neighbor particle of $\boldsymbol{x}$

2. $(\boldsymbol{x}_i')_j'$ is the j^{th} neighbor particle of $\boldsymbol{x}_i'$

3. $\delta \boldsymbol{u}_{x'_j}$ is the displacement of particle $\boldsymbol{x}'_j$, etc.

4. N,K,$\frac{\partial \boldsymbol{P}}{\partial \boldsymbol{F}}$ are the number of neighboring particles, the shape tensor and the tangent moduli, respectively, of particle $\boldsymbol{x}$; N',K',$\frac{\partial \boldsymbol{P}'}{\partial \boldsymbol{F}'}$ are the corresponding quantities for particle $\boldsymbol{x}'_i$

5. ω_i and ω_j are the influence functions for the bonds $(\boldsymbol{x}'_i - \boldsymbol{x})$ and $(\boldsymbol{x}'_j - \boldsymbol{x})$ respectively; ω'_i and ω'_j are defined for bonds $(\boldsymbol{x} - \boldsymbol{x}'_i)$ and $((\boldsymbol{x}'_i)'_j - \boldsymbol{x}'_i)$.

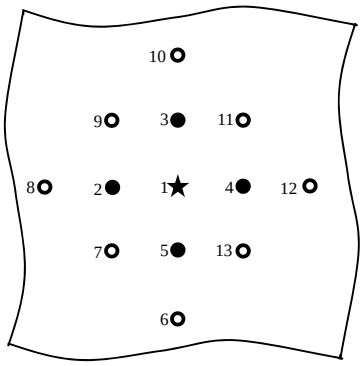

Figure 5.2: *Illustration of one particle interaction for a peristatic model with nearest neighbor interactions. Here, particles $i = 2, 3, 4, 5$ (denoted as $\boldsymbol{x}'_i$) are neighbors of the particle 1 (denoted as $\boldsymbol{x}$). Particles $j = 1, 7, 8, 9$ (denoted as $(\boldsymbol{x}'_2)'_j$) represent the neighbors of particle 2 ($\boldsymbol{x}'_2$). In this case, the row of Jacobian $\mathcal{J}$ corresponding to particle 1 will include entries from all 13 particles shown here.*

The above equation for $d\boldsymbol{L}(\boldsymbol{x})$ leads to an implicit form for the Jacobian $\mathcal{J}$ for use in Eq. 5.6. For a 2D problem, the global matrix is $2N_{total} \times 2N_{total}$ where N_{total} is the total number of particles in the simulation. The sparseness of the matrix depends on the radius of influence δ, and varies from sparsely populated for a small cutoff that only includes nearest neighbor interactions (Fig. 5.2) to a fully populated matrix for a large cutoff (a highly non–local system). The system of equations are

iteratively solved until $||\delta \boldsymbol{u}_p|| < \epsilon_1$, where $\epsilon_1 = 10^{-6}$, a small numerical cut–off. The crystal plasticity formulation uses displacement boundary conditions that are directly enforced on the boundary particles ($\boldsymbol{u}_x = (\exp(\boldsymbol{L}_{macro}t) - \boldsymbol{I})\boldsymbol{x}$) ([8]) based on a macroscopic velocity gradient $\boldsymbol{L}_{macro} = \dot{\boldsymbol{F}}\boldsymbol{F}^{-1}$, time t and identity matrix $\boldsymbol{I}$. After solving the system, the inner particle displacements are incremented by $\delta \boldsymbol{u}_p$. The history–dependent variables in the constitutive equations are then updated for use in the next loading step. The constitutive model is the same as Section 2.3.

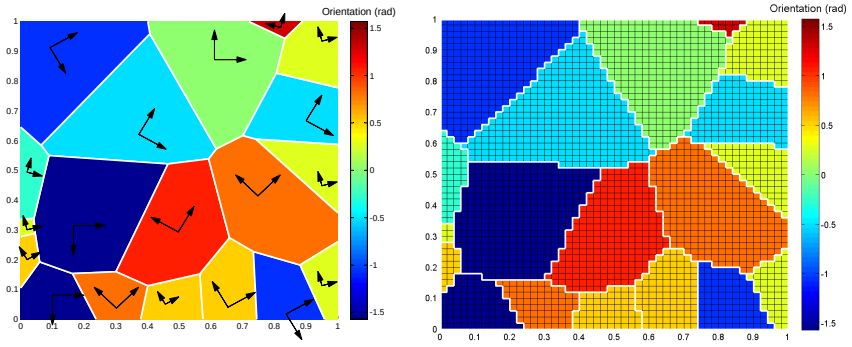

(a) (b)

Figure 5.3: *(a) Initial microstructure represented by 19 planar grains with the crystal coordinate system indicated (b) Pixel–based grid is used to represent the microstructure in finite element calculations.*

5.3 Examples of peristatic crystal plasticity constitutive model

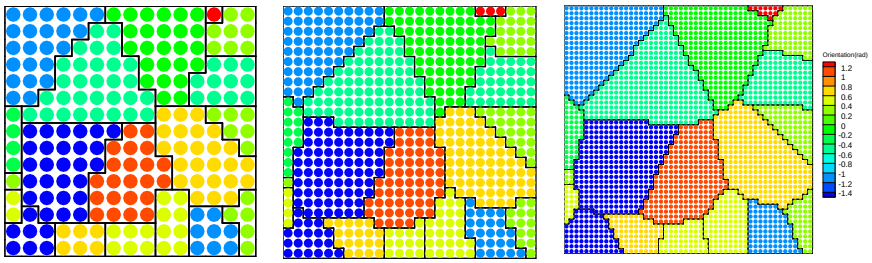

(a) (b) (c)

Figure 5.4: *Peristatic particle grids employed in this work, the particles are located at the centers of elements in pixel–based grids (a) 225 particles (b) 625 particles (c) 2500 particles.*

Considering planar polycrystals characterized by a two dimensional rotation $\boldsymbol{R}$ that relates the local crystal lattice frame to the reference sample frame. A parametrization of the associated rotation group is,

$$\boldsymbol{R} = \boldsymbol{I}cos(g) - \boldsymbol{E}sin(g) \tag{5.10}$$

where g is the angle between the crystal and sample axes, $\boldsymbol{E}$ is the two dimensional alternator ($E_{11} = E_{22} = 0, E_{12} = -E_{21} = 1$), and $\boldsymbol{I}$ is the identity tensor. A general planar crystal with symmetry under rotations through π is considered here. Under the symmetry, crystal orientations can be described uniquely by parameters drawn from a simply connected fundamental region $(-\pi/2, \pi/2)$. Due to symmetry, the orientation $\pi/2$ is exactly the same as orientation $-\pi/2$. During the peristatic simulation, the crystal reorientation velocity ($\boldsymbol{v} = \frac{\partial \boldsymbol{g}}{\partial t}$) is obtained by taking a derivative of relation Eq. 5.10:

$$\boldsymbol{v} = \frac{1}{2} E.\Omega \tag{5.11}$$

where $\boldsymbol{\Omega}$ is the spin tensor defined as $\boldsymbol{\Omega} = \dot{\boldsymbol{R}}^e \boldsymbol{R}^{eT}$. Here, $\boldsymbol{R}^e$ is evaluated through the polar decomposition of the elastic deformation gradient $\boldsymbol{F}^e$ as $\boldsymbol{F}^e = \boldsymbol{R}^e \boldsymbol{U}^e$. The texturing of the polycrystal is tracked by computing the change in orientation $\Delta \boldsymbol{g} = \boldsymbol{v} \Delta t$ of particles at each time step.

A $1 \times 1\ mm^2$ microstructure with a total of 19 grains was computationally generated using Voronoi construction as shown in Fig. 5.3(a). The microstructure is subjected to plane strain compression with the imposed macroscopic velocity gradient $\boldsymbol{L}$ given as:

$$\boldsymbol{L} = \eta \begin{bmatrix} 1 & 0 \\ 0 & -1 \end{bmatrix} \tag{5.12}$$

where $\eta = 0.0020$. The simulations were performed over 30 steps with this velocity gradient, leading to a final strain of about 0.06.

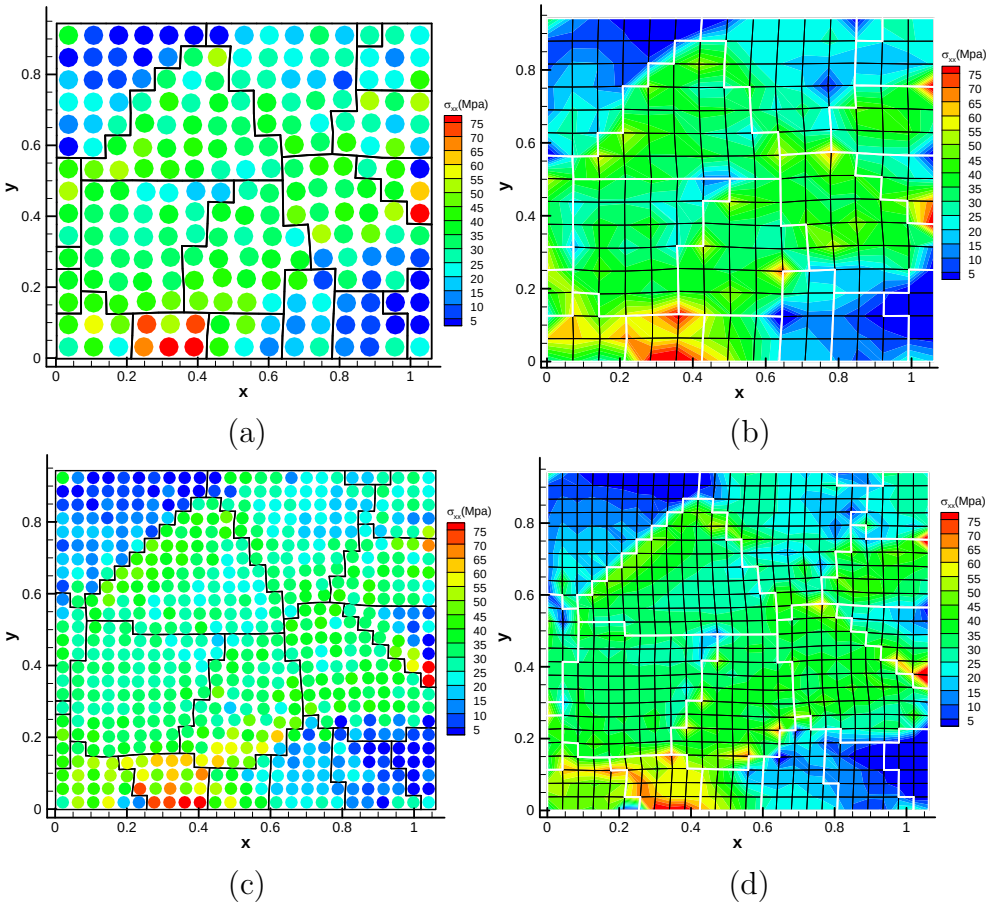

Figure 5.5: *Comparison of σ_{xx} from peristatics and CPFE model for a 225 particle/element mesh in (a,b) and a 625 element mesh in (c,d)*

Twelve different orientations from within the interval $(-\pi/2, \pi/2)$ (step size of $\pi/12$) were distributed among the grains. Two slip systems at orientations $-\pi/6$ and $+\pi/6$ were considered. The values in the elastic stiffness matrix are taken as $\mathbb{C}_{11} = 2\ GPa$ and $\mathbb{C}_{12} = \mathbb{C}_{44} = 1\ GPa$. The particular hardening law in Eq. 3.1 was chosen as follows:

$$h^{\alpha\beta} = h_o^{\beta}(q + (1-q)\delta^{\alpha\beta})(1 - \frac{s^{\beta}(t)}{s_s^{\beta}})^a \text{ (no sum on } \beta) \tag{5.13}$$

The slip system hardening term ($h^{\alpha\beta}$) includes latent hardening through parameter q. In this term, h_o^{β} is the hardening coefficient and s_s^{β} is the saturation resistance of

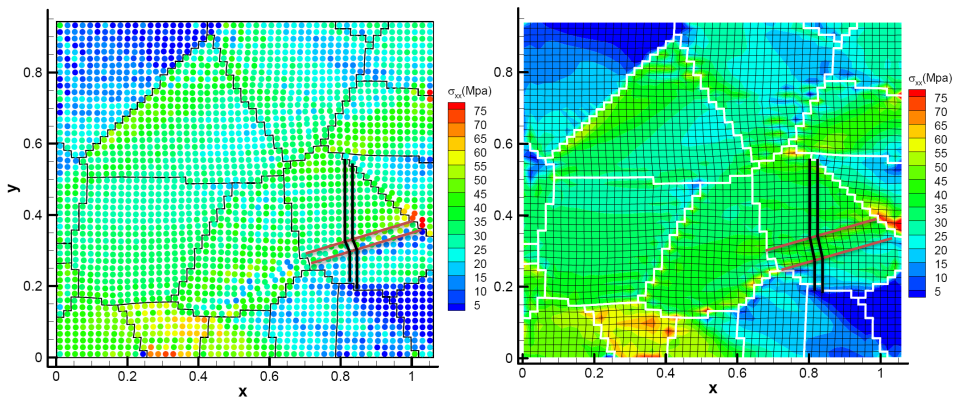

(a) (b)

Figure 5.6: *Comparison of σ_{xx} between peristatic and FE results (a) 2500 particle peristatics (b) 2500 element CPFE model. The width of a shear band is compared.*

slip system β. The values for the slip hardening parameters are taken to be identical for both slip systems and are listed below:

$$h_o = 10 \text{ MPa}, s_s = 200 \text{ MPa}, a = 2, \tau_0 = 10 \text{ MPa}, q = 1.4 \tag{5.14}$$

Results from the peristatic model are compared with a crystal plasticity finite element (CPFE) model (from [58]). While the underlying constitutive equations for both peristatic and CPFE models are the same, differences emerge from the governing equation (linear momentum conservation). The governing equations for peristatic theory is of the non–local (integral) form that includes long range interactions while the corresponding CPFE equations are of the localized (differential) form. A quantitative comparison of these theories can be enabled if the non–locality of the peristatic theory is kept to a minimum by using the lowest possible radius of interaction for the particles, and using similar meshes. This involves including just the nearest neighbor interactions by bonding of each particle to its four nearest neighbors similar to an Ising model ([75])[2]. The influence function ω was taken to be a constant ($\omega = 1$) to

[2]Note that the non–locality of peristatic theory implies that there is an implicit interaction of

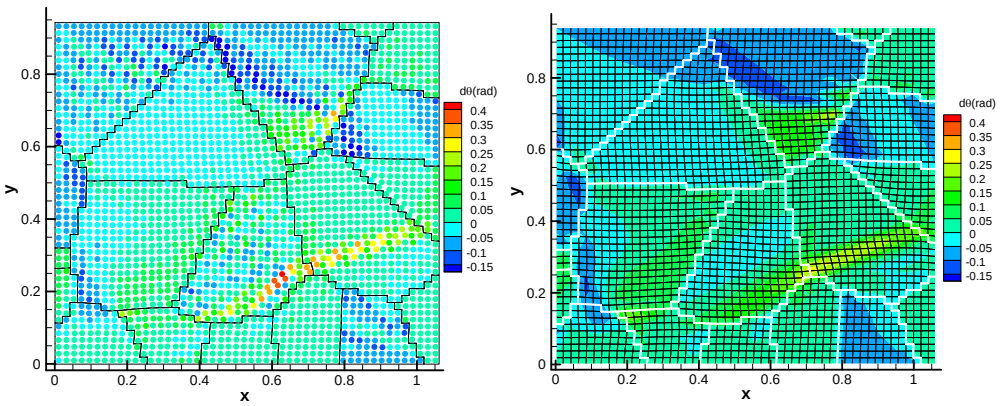

(a) (b)

Figure 5.7: *(a) Orientation change for 2500 particles from peristatics (b) CPFE result.*

circumvent the issue of fitting an influence function ([55]). The finite element mesh used the same number of elements as the number of particles in the peristatic case. The model is discretized using a pixel mesh (four noded square elements) as shown in Fig. 5.3(b). The particles in the peristatic simulations were located at the center of these elements. Each particle occupies a constant volume in the reference configuration equal to the area of the enclosing finite element. Three cases were considered with 225, 625 and 2500 particles, respectively, as shown in Fig. 5.4.

The particles in the peristatic simulation are colored using field values in order to compare with finite element contours obtained from the CPFE model. The same contour levels were used and the figures are best compared in color (in the electronic version of the manuscript). In Fig. 5.5, the x–stress σ_{xx} contours of peristatics and CPFE model are compared at the final strain. Results for a 225 element and a 625 element simulation are shown. Although the overall stress distribution and the locations of maximum and minimum stresses are similar between these two models, certain differences are seen that become more pronounced at a higher mesh refinement. For example, Fig. 5.6 shows the comparison of the x–stress contours for a 2500

field quantities over 13 particles (as illustrated in Fig. 5.2).

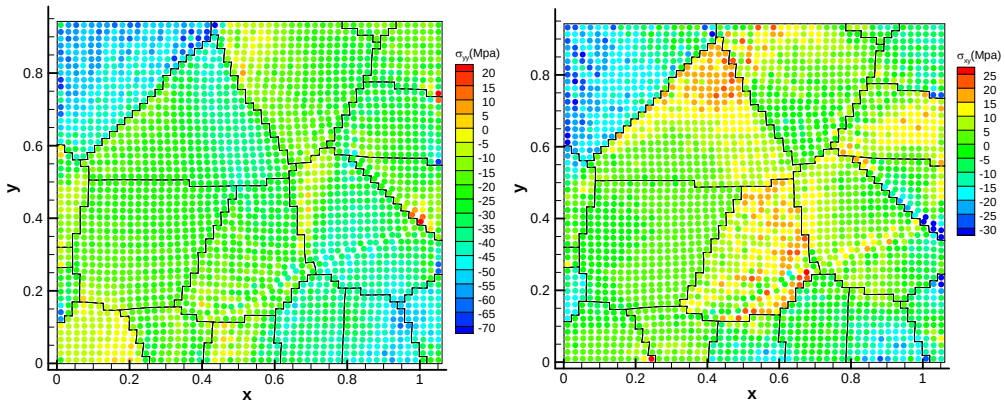

Figure 5.8: *Comparison of components of stress tensor from peristatics simulation (a) σ_{yy} (b) σ_{xy}*

element mesh. The differences seen pertain to the emergence of shear bands in the microstructure. Although the locations and orientations of shear bands are identical, the bands seen from FE simulations are comparatively more diffuse. As an example, the width of a shear band at the same location in both models are shown using lines superposed on a grain in Fig. 5.6. Two key differences are seen when comparing the two models. Firstly, FE results show thicker shear bands that can be attributed to lack of an internal length scale; an issue that is well studied in literature (eg. [48]). Peristatic models do include an explicit length scale in the form of a radius of interaction and lead to finer shear bands, qualitatively closer to those seen in experiments [76]. Secondly, the nature of shearing within the band is heterogeneous in the peristatic case; as seen from the irregular positions of particles within the shear band in a peristatic case versus a more uniform distribution of shear strain across the band in the CPFE case. Such inhomogenieties within a shear band have also been measured experimentally (EBSD results from [76]) in the form of (almost periodic) changes in orientation within a shear band.

To test this aspect, the reorientation map predicted by the peristatic and CPFE models are compared in Fig. 5.7. The overall contours predicted by CPFE and peri-

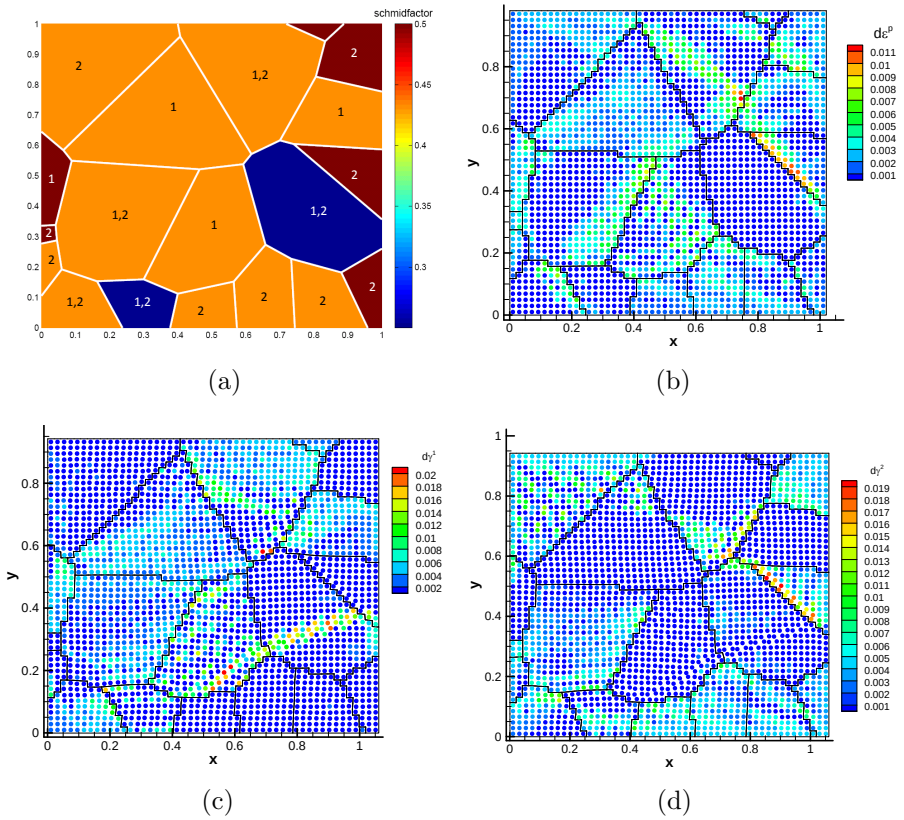

Figure 5.9: *(a) Maximum Schmid factors of grains, the slip system corresponding the maximum Schmid factor is marked on the grains (b)Contours of equivalent plastic strain increment at low strains ($\epsilon = 0.02$) show no slip activity on grains with the lowest Schmid factor (c) Plastic shear increments for slip system 1 (largely occur on grains marked '1' in the Schmid factor plot). (d) Plastic shear increments of slip system 2 (largely occur on grains marked '2' in the Schmid factor plot).*

static models are similar. Significant reorientation is seen within shear bands in both models, although the CPFE results are more diffuse and weaker in intensity compared to the peristatic simulation. Interestingly, the orientation changes within the shear band indicated in Fig. 5.6 show periodic behavior seen from recent experiments ([76]). Other components of the stress tensor (y–stress and xy–shear stress) predicted by peristatics are shown in Fig 5.8. These stresses display localization in regions that are different from those seen in the x–stress contours. For example, the grain with the shear band indicated in Fig. 5.6 also has a band of high y– and xy– stresses lying along the grain boundary to the left, adjacent to a grain with high shear stresses.

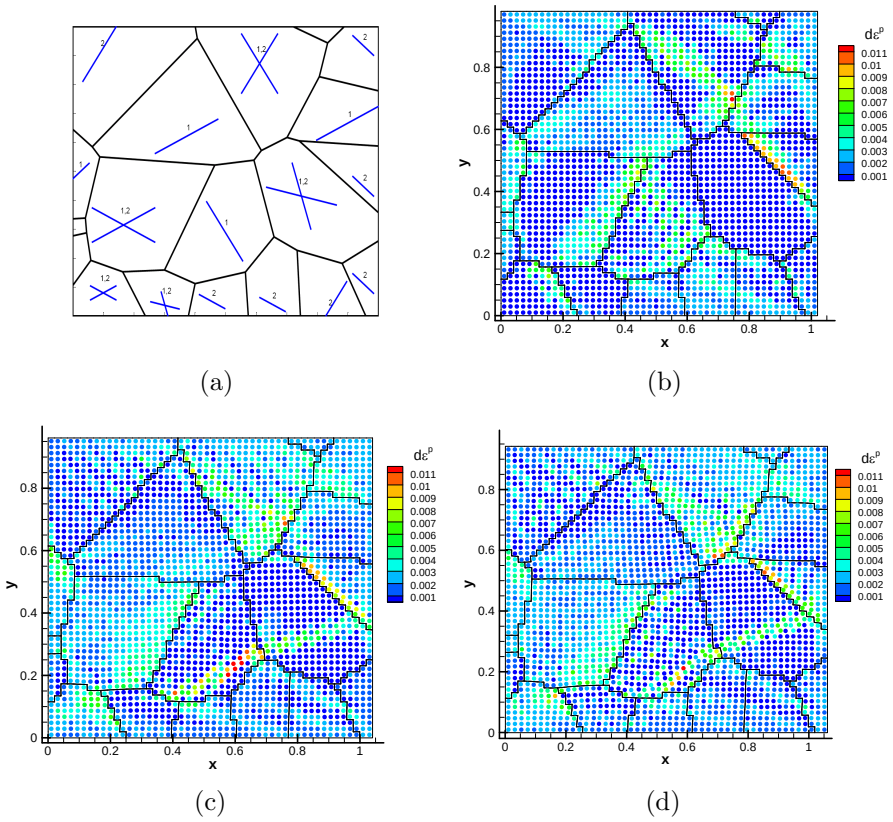

Figure 5.10: *(a) Active slip systems identified using a simple Schmid factor analysis (b) Contours of equivalent plastic strain increment at* $\epsilon = 0.02$ *(c) Contours at* $\epsilon = 0.04$ *(d)Contours at* $\epsilon = 0.06$.

The shear band indicated in Fig. 5.6 extends into the grain to the left, and this band is seen to have lower shear stresses compared to the surrounding grain.

The origin of shear bands is studied next through analysis of time evolution of the microstructure during loading. Firstly, the potential active slip systems were identified using a rudimentary Schmid factor analysis. To compute the maximum Schmid factor for each grain, the loading axis is represented in the crystal frame of reference as $v_c = \boldsymbol{R}^T v_s$ where v_s is the loading axis in the sample reference frame (here, $v_s = [1; 0]$). The Schmid factor for each slip system was identified as $\mathbb{S}^\alpha = |(m_0^{\alpha^T} * v_c)(n_0^{\alpha^T} * v_c)|$ and the slip system with the maximum Schmid factor was marked as the active system. Fig. 5.9(a) shows a plot of the maximum Schmid factor in each grain. Each grain is marked with the slip system number (α) that gives the

maximum Schmid factor. If the Schmid factor for both slip systems are equal within a grain, both the systems are marked. The equivalent plastic strain increment[3] at an effective strain of 0.02 is shown in Fig. 5.9(b). A comparison of these two figures (Fig. 5.9(a,b)) shows that the deformation processes primarily occur in grains with a high Schmid factor. Little plasticity, if any, is seen in the grains with the lowest Schmid factor. The plastic shearing increments ($\Delta\gamma^1$ and $\Delta\gamma^2$) on slip systems 1 and 2 are shown in Fig 5.9(c) and (d) respectively at an effective strain of 0.06. The shear increments for slip system 1 shown in Fig. 5.9(c) largely occur on grains marked '1' in Fig. 5.9(a). Similarly, the shear increments of slip system 2 shown in Fig. 5.9(d) largely occur on grains marked '2' in Fig. 5.9(a). On grains where both slip systems have the same Schmid factor, the grain is seen to be partitioned into sections where one of the two slip systems are active. As seen previously in Fig. 5.7, these grain sections have different reorientation angles that eventually partition the grain into two or more orientations. Interestingly, shear bands become active in low Schmid factor grains at larger strains (eg. the grain marked in Fig. 5.6 was a low Schmid factor grain), indicating that this is a possible deformation mechanism in grains that are not favorably oriented for slip activity. Finally, the shear increments are seen to form a laminated pattern in several grains. The evolution of this lamellae and shear bands were studied as a function of strain to identify relationships, if any, between these features and the slip geometry.

Fig. 5.10(a) shows the orientation of active slip systems for each grain as identified using the Schmid factor analysis. The evolution of the effective plastic strain increments are shown in Fig. 5.10(b,c,d) as a function of increasing applied strain. The shear band seen in the grain shown in Fig. 5.6 does not form along any particular slip direction. As the microstructure is loaded, strain localization progresses in the form of a laminated pattern. While some lamellae do bear a relationship with slip direction,

[3]The equivalent plastic strain increment is defined as ([46]) $d\epsilon^p = \frac{\sum_\alpha \tau^\alpha \Delta\gamma^\alpha}{\sigma_{eff}}$ where, σ_{eff} is the von Mises stress.

in general, lamellae appear to align with directions along which shear bands eventually form. Recent experiments (based on digital image correlation, [77]) also indicate that shear banding initiates in the form of lamellae of localized strain that eventually merge to form a larger shear band. These shear bands move into neighboring grains and the process repeats through formation of new lamellar structures.

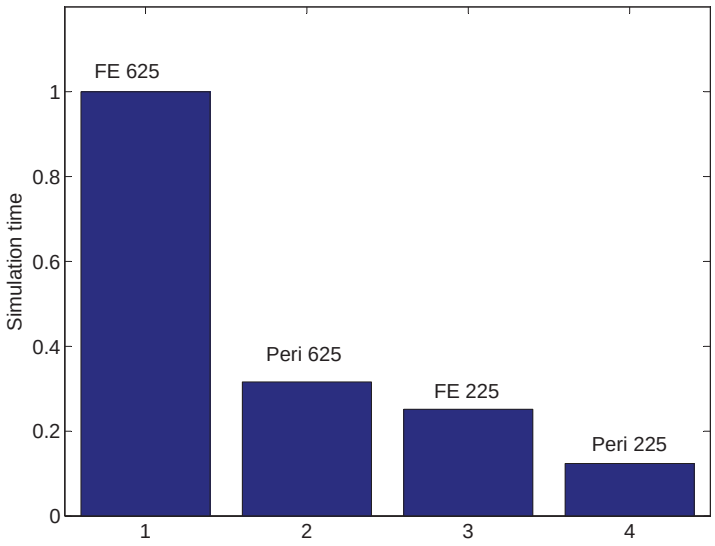

Figure 5.11: *Comparison of simulation times (normalized) for two methods.*

Finally, a comparison of simulation times for the CPFE and peristatic models is shown for different mesh sizes in Fig. 5.11. Both CPFE and peristatic simulations are fully parallel and utilize eight (3 GHz) processors on a HP workstation. The simulation times were computed based on the first ten time steps ($\Delta t = 0.1$ sec) of each method and normalized with respect to the simulation time for the most expensive approach. CPFE was the more expensive approach for all three meshes. This is primarily due to the fact that FE simulations employ four integration points per element, which increases both the number of calculations and quadruples the amount of storage (of constitutive model parameters such as elastic and plastic deformation gradients) versus a peristatic case. On the other hand, peristatic model does have a less sparse global matrix and thus, the solution time is comparatively higher.

However, for the nearest neighbor interactions modeled in this work, the sparseness issue did not seem to increase the computational time as much. Both the assembly and solution time to increase significantly are expected with increase in the radius of influence (δ) making FE simulations faster when including longer range interactions.

5.4 Conclusions

The primary contribution of this work is a fully implicit numerical implementation of crystal plasticity within a peristatic framework. A state–based theory of peridynamics is used ([55]) where the the bond forces are described using second-order stress tensors computed using a standard crystal plasticity constitutive model. The deformation gradient at the particle is computed using the motion of the collection of particles within a radius of influence. The highlight of this approach is that the model is fully non–local, without the need to make any change to the underlying constitutive model. A Newton–Raphson implementation of peristatics is developed here that allows solution of a general non–linear, finite deformation crystal plasticity problem. The peristatic results were compared against crystal plasticity finite element (CPFE) analysis for the problem of plane strain compression of a planar polycrystal. The stress, strain and texture fields predicted by CPFE and peristatics were found to be largely similar. One particular feature of peristatics is its ability to model fine shear bands that occur naturally in deforming polycrystalline aggregates. The particles within a shear band show inhomogeneity in plastic deformation and reorientation. Peristatic simulations were used to study the origin and evolution of these shear bands as a function of strain and slip geometry. It is seen that the shear band formation is a favorable deformation mode in grains with a low Schmid factor. Shear bands are found to originate in the form of lamellar structures that merge to form a single shear band. The orientation of the shear band, by itself, are not aligned with the slip directions.

CHAPTER VI

Future Work

The current landscape of materials science features increased use of high performance computational simulation tools and the use of information technologies for analysis of microstructure-dependent material properties. However, efficient multi–scale modeling tools are still required to model critical aspects such as fracture and fatigue bahavior of advanced structural alloys. Integrated Computational Materials Engineering (ICME) ([78]) is an emerging paradigm that emphasizes integration of micro–scale material models with engineering analysis of products and processes so as to enable design of microstructurally tailored materials. Towards this end, this work has provided new theories to efficiently model polycrystalline microstructures, a novel multi-scale model that combines probabilistic descriptors of microstructure with crystal plasticity finite element method, a new multi-scale method to simulate crack propagation in elasto–plastic polycrystals and an altogether new simulation approach, peristatics, which offers great potential for modeling shear localization. The work points towards several interesting future directions as listed below.

6.1 Higher order descriptors for multiscale modeling

Multi-scale model was developed using the ODF representation in Chapter III. GSODF in Chapter II can also be combined with the multi-scale model. This will

provide more accurate information to the multi-scale model to facilitate engineering analysis when considering the effect of grain size such as the Hall–Petch effect. Other higher order descriptor like COCF [1] can also be used to achieve higher accuracy by including aspects of interaction of grains with its neighbors. In addition, the formulation needs to be extended to study 3D crystal structures (eg. FCC Aluminum).

6.2 Enhancements to VMCM

VMCM in Chapter IV is a powerful method for isotropic and polycrystalline material crack propagation in the monotonic loading mode. One aspect that can be pursued in future work is to extend the method for the simulation of fatigue crack propagation under cyclic loading. The model of a cycle dependent cohesive failure law (Maiti(2005) [79]) can used for fatigue fracture problems. VMCM in Chapter IV needs to be extended to 3D problems. The theory to that end has not yet been developed and should be a near–term goal. In addition, the VMCM approach should be developed for elements such as six–noded triangles or higher order quadrilateral elements in order to effectively implement the method for large strain deformation problems in which volumetric locking may be an issue. In addition, identification of the correct parameters in the cohesive model is of great interest. This includes identification of critical tractions, the fracture energy and a criteria for identification of crack growth direction in elasto–plastic crystals. In-situ fracture experiments within an scanning electron microscope should be targeted for accomplishing these goals.

6.3 Nonlinear peristatics

Peristatic is a new method which has great potential to be further developed in following directions.

6.3.1 Improvements to peristatics

Current implementations in this work only contain hundreds of particles. Parallel scheme in cluster solvers can be done to include millions of particles for large scale problems. Future work can also be focused on extending the formulation to study 3D crystal structures (eg. FCC Aluminum). There is also value in performing a parametric study of the effect of misorientation distribution, crystal structure and deformation on the activation and propagation of shear bands in these materials. Validation of crystal plasticity models developed in this work with strain maps from micro–scale digital image correlation (DIC) experiments [2] should be a near–term goal.

6.3.2 Crack simulations using peristatics

Recently, bond-based peridynamics have been widely used to simulate crack propagation and crack branching. It has a great advantage to capture progressive material damage with bond-failure criterion, so it does not require criteria for crack propagation or crack branching. Youn Doh Ha [80] used peridynamics to model and simulate dynamic fracture, crack branching in brittle materials. State based peridynamics developed by Sillings [55] formulates the forces between particles based on stress tensors obtained from continuum formulations (eg. crystal plasticity). This method can directly model sharp displacement discontinuities ([56]). However, either bond based or state based peridynamics requires significant simulation time to achieve correct quasistatic stress distribution due to its dynamic framework. Peristatics can provide an option to simulate fracture in a similar way but with increased efficiency in stress predication. The Fig 6.1 shown below demonstrates the use peristatics to study simple tension crack with initial crack introduced. It has great convergence ability and can be applied directly on surface of discontinuity as the peridynamics model.

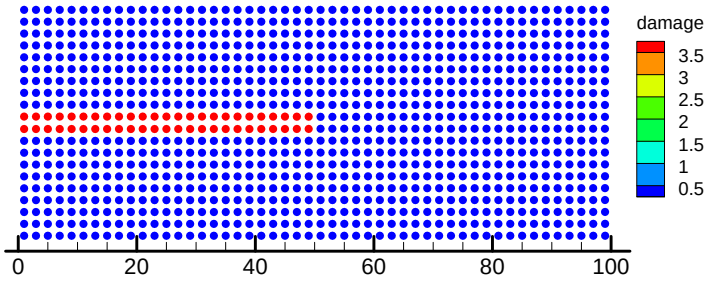

(a)

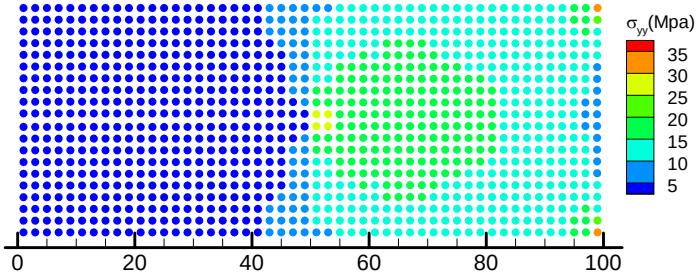

(b)

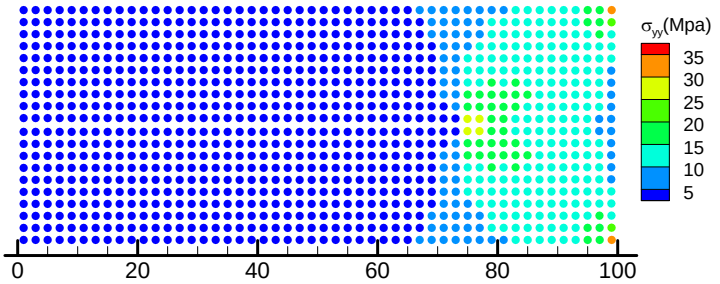

(c)

Figure 6.1: *(a) Initial 1000 particles with a crack from left boundary to the middle of the specimen (b) σ_{yy} distribution before crack propagates (c) σ_{yy} distribution after crack being formed to location $x = 74$.*

6.3.3 Address dynamic problems

One future work is to model dynamic loading (eg. ballistic loading) in metals using peridynamics[81]. Shown in following Fig. 6.2 is the stress distribution comparison between dynamic finite element analysis and peridynamics analysis from our simulation code. Extension of the approach to modeling dynamic events or wave propagation in polycrystals is also a near–term goal.

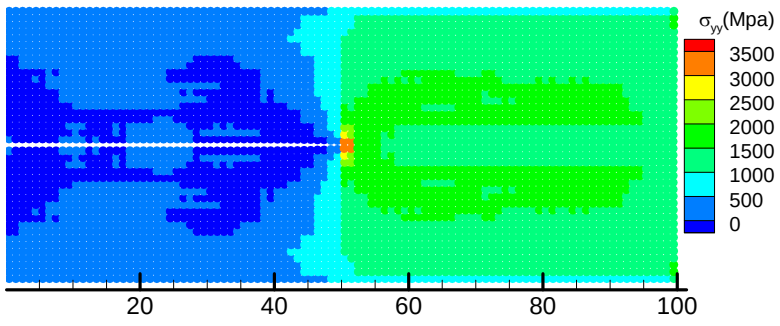

(a)

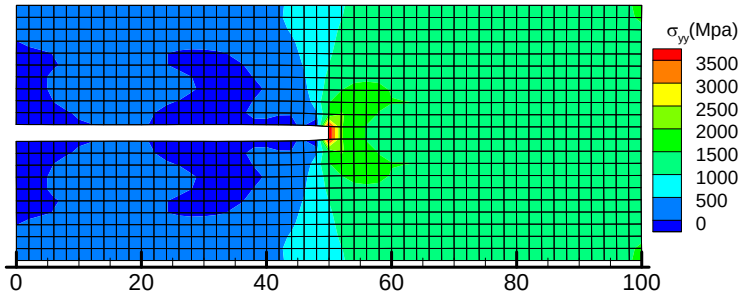

(b)

Figure 6.2: *(a) Peridynamic σ_{yy} distribution after displacement loading at the top boundary with 1000 particles. (b) σ_{yy} distribution from dynamic FE calculation with 1000 elements .*

APPENDICES

APPENDIX A

Constitutive update scheme

The quantities at the current time step are denoted by subscript $(n+1)$. The deformation gradient $\boldsymbol{F}_{n+1}$ is known at the current time step and the update procedure given here is used to compute the PK-I stress $\boldsymbol{P} = \mathcal{F}(\boldsymbol{F}_{n+1})$ where $\mathcal{F}$ is the constitutive model described in section 2.3.

An Euler-backward time integration procedure for equation 2.9 leads to the following approximation:

$$\boldsymbol{F}^p \;=\; \exp(\Delta t \sum_\alpha \dot{\gamma}^\alpha \boldsymbol{S}_0^\alpha sign(\tau^\alpha))\boldsymbol{F}_n^p \;\approx\; (\boldsymbol{I} + \sum_\alpha \Delta\gamma^\alpha \boldsymbol{S}_0^\alpha sign(\tau^\alpha))\boldsymbol{F}_n^p \qquad \text{(A.1)}$$

Substituting Eq. (A.1) into the multiplicative decomposition $\boldsymbol{F} = \boldsymbol{F}^e\ \boldsymbol{F}^p$ results in the following:

$$\boldsymbol{F}^e \;=\; \boldsymbol{F}^e_{trial}(\boldsymbol{I} - \sum_\alpha \Delta\gamma^\alpha \boldsymbol{S}_0^\alpha sign(\tau^\alpha)) \qquad \text{(A.2)}$$

where $\boldsymbol{F}^e_{trial}$ is the trial elastic deformation gradient and is given as $\boldsymbol{F}_{n+1}(\boldsymbol{F}_n^p)^{-1}$.

The Green elastic strain measure is computed using Eq. (A.2) as

$$\begin{aligned} \bar{\boldsymbol{E}}^e &= \frac{1}{2}\left(\boldsymbol{F}^{eT}\boldsymbol{F}^e - \boldsymbol{I}\right) \\ &= \bar{\boldsymbol{E}}^e_{trial} - \frac{1}{2}\sum_\alpha sign(\tau^\alpha)\Delta\gamma^\alpha \boldsymbol{B}^\alpha \end{aligned} \qquad \text{(A.3)}$$

where $\bar{\boldsymbol{E}}^e_{trial}$ and $\boldsymbol{B}^\alpha$ are defined as

$$\begin{aligned} \bar{\boldsymbol{E}}^e_{trial} &= \frac{1}{2}\left((\boldsymbol{F}^e_{trial})^T\boldsymbol{F}^e_{trial} - \boldsymbol{I}\right) \\ \boldsymbol{B}^\alpha &= (\boldsymbol{S}^\alpha_0)^T(\boldsymbol{F}^e_{trial})^T\boldsymbol{F}^e_{trial} + (\boldsymbol{F}^e_{trial})^T\boldsymbol{F}^e_{trial}\boldsymbol{S}^\alpha_0 \end{aligned} \tag{A.4}$$

Using Eq. A.3 in the constitutive relation for stress $\bar{\boldsymbol{T}} = \boldsymbol{\mathcal{C}}^e\left[\bar{\boldsymbol{E}}^e\right]$ leads to the following

$$\bar{\boldsymbol{T}} = \bar{\boldsymbol{T}}_{trial} - \frac{1}{2}\sum_\beta \Delta\gamma^\beta \boldsymbol{\mathcal{C}}^e\left[\boldsymbol{B}^\beta\right] sign(\boldsymbol{\tau}^\beta_{trial}) \tag{A.5}$$

where $\bar{\boldsymbol{T}}_{trial} = \boldsymbol{\mathcal{C}}^e\left[\bar{\boldsymbol{E}}^e_{trial}\right]$.

A trial resolved shear stress $\boldsymbol{\tau}^\alpha_{trial} = \bar{\boldsymbol{T}}_{trial}\cdot\boldsymbol{S}^\alpha_0$ is then computed. A potentially active set $\mathcal{PA}$ of slip systems can be identified based on the trial resolved stress as the systems with $|\boldsymbol{\tau}^\alpha_{trial}| - s^\alpha > 0$.

During plastic flow, the active systems are assumed to follow the consistency condition: $|\tau^\alpha| = s^\alpha$. Increment in shearing rates $\Delta\gamma^\beta$ at each time step is obtained by solving the following equation obtained by resolving Eq. (A.5) along slip directions:

$$|\tau^\alpha| = s^\alpha = |\tau^\alpha_{trial}| - \frac{1}{2}\sum_\beta sign(\tau^\alpha_{trial})sign(\tau^\beta_{trial})\Delta\gamma^\beta \boldsymbol{\mathcal{C}}^e\left[\boldsymbol{B}^\beta\right]\cdot\boldsymbol{S}^\alpha_0 \tag{A.6}$$

where, $\alpha, \beta \in \mathcal{PA}$.

A system of equations is obtained of the following form,

$$\sum_{\beta\in\mathcal{PA}} A^{\alpha\beta}\Delta\gamma^\beta = b^\alpha \tag{A.7}$$

where,

$$A^{\alpha\beta} = h^{\alpha\beta} + \frac{1}{2} sign(\boldsymbol{\tau}^{\alpha}_{trial}) sign(\boldsymbol{\tau}^{\beta}_{trial}) \boldsymbol{\mathcal{C}}^{e} \left[\boldsymbol{B}^{\beta}\right] \cdot \boldsymbol{S}^{\alpha}_{0}$$
$$b^{\alpha} = |\tau^{\alpha}_{trial}| - s^{\alpha} \tag{A.8}$$

If for any system $\Delta\gamma^{\beta} \leq 0$, then this system is removed from the set of potentially active systems. The system is repeatedly solved until for all systems $\Delta\gamma^{\beta} > 0$.

APPENDIX B

Implicit computation of tangent moduli

The linearization process of PK–I stress is given by:

$$\delta \boldsymbol{P} = \delta((\det \boldsymbol{F})\boldsymbol{\sigma}\boldsymbol{F}^{-T}) = \det \boldsymbol{F}\left(\mathrm{tr}(\delta \boldsymbol{F}\boldsymbol{F}^{-1})\boldsymbol{\sigma} - \boldsymbol{\sigma}(\delta \boldsymbol{F}\boldsymbol{F}^{-1})^T + \delta\boldsymbol{\sigma}\right)\boldsymbol{F}^{-T} \tag{B.1}$$

$\delta\boldsymbol{\sigma}$ can be expressed as:

$$\begin{aligned}\delta\boldsymbol{\sigma} &= \delta\left(\frac{1}{\det \boldsymbol{F}^e}\boldsymbol{F}^e\bar{\boldsymbol{T}}(\boldsymbol{F}^e)^T\right)\\ &= -tr(\boldsymbol{F}^{-1}\delta\boldsymbol{F})\boldsymbol{\sigma} + \delta\boldsymbol{F}^e(\boldsymbol{F}^e)^{-T}\boldsymbol{\sigma} + \boldsymbol{\sigma}(\boldsymbol{F}^e)^{-1}\delta(\boldsymbol{F}^e)^T + \frac{1}{\det \boldsymbol{F}^e}\boldsymbol{F}^e\delta\bar{\boldsymbol{T}}(\boldsymbol{F}^e)^T\end{aligned} \tag{B.2}$$

The above expression requires the evaluation of $\delta\boldsymbol{F}^e$ and $\delta\bar{\boldsymbol{T}}$ using the constitutive model. In order to obtain $\delta\bar{\boldsymbol{T}}$, we consider the linearization of Equation (A.5) to obtain:

$$\begin{aligned}\delta\bar{\boldsymbol{T}} \;=\; & \boldsymbol{\mathcal{C}}^e\left[\delta\bar{\boldsymbol{E}}^e_{trial}\right] - \frac{1}{2}\sum_\beta \mathrm{sgn}(\tau^\beta_{trial})\delta(\Delta\gamma^\beta)\boldsymbol{\mathcal{C}}^e\left[\boldsymbol{B}^\beta\right]\\ & - \sum_\beta \mathrm{sgn}(\tau^\beta_{trial})\Delta\gamma^\beta\boldsymbol{\mathcal{C}}^e\left[\boldsymbol{S}_0^{\beta T}\delta\bar{\boldsymbol{E}}^e_{trial} + \delta\bar{\boldsymbol{E}}^e_{trial}\boldsymbol{S}_0^\beta\right]\end{aligned} \tag{B.3}$$

This computation of $\delta\bar{\boldsymbol{T}}$ requires the evaluation of $\delta(\Delta\gamma^\beta)$, obtained by linearization given by:

$$\delta(\Delta\gamma^\beta) \;=\; (A^{\alpha\beta})^{-1}(\delta b^\alpha - \delta A^{\alpha\beta}\Delta\gamma^\beta) \tag{B.4}$$

$$\delta b^\alpha = \mathrm{sgn}(\tau^\alpha_{trial})\boldsymbol{\mathcal{C}}^e\left[\delta\bar{\boldsymbol{E}}^e_{trial}\right]\cdot\boldsymbol{S}^\alpha_0 \tag{B.5}$$

$$\delta A^{\alpha\beta} = \mathrm{sgn}(\tau^\alpha_{trial})\mathrm{sgn}(\tau^\beta_{trial})\boldsymbol{S}^\alpha_0\cdot\boldsymbol{\mathcal{C}}^e\left[\boldsymbol{S}^{\beta T}_0\delta\bar{\boldsymbol{E}}^e_{trial} + \delta\bar{\boldsymbol{E}}^e_{trial}\boldsymbol{S}^\beta_0\right] \tag{B.6}$$

Using the definition of $\delta\bar{\boldsymbol{E}}^e_{trial} = \mathrm{sym}(\boldsymbol{F}^{eT}_{trial}\delta\boldsymbol{F}\boldsymbol{F}^{p^{-1}}_n)$, the above set of equation yield an implicit form $\delta(\Delta\gamma^\beta) \;=\; \boldsymbol{m}^\beta\cdot\delta\boldsymbol{F}$ for use in Eq. (B.3). Next, $\delta\boldsymbol{F}^e$ is obtained from:

$$\delta(\boldsymbol{F}^e) \;=\; \delta\boldsymbol{F}(\boldsymbol{F}^p)^{-1} - \boldsymbol{F}^e_{trial}\sum_\beta \mathrm{sgn}(\tau^\beta_{trial})\delta(\Delta\gamma^\beta)\boldsymbol{S}^\beta_0 \tag{B.7}$$

BIBLIOGRAPHY

BIBLIOGRAPHY

[1] V. Sundararaghavan and A. Kumar. Probabilistic modeling of microstructure evolution using finite element representation of statistical correlation functions. *Int. J. Plast.*, 30–31:62–80, 2012.

[2] A.D. Kammers and S. Daly. Digital image correlation under scanning electron microscopy: Methodology and validation. *Experimental Mechanics*, 53(9):1743–1761, 2013.

[3] S.V. Harren and R.J. Asaro. Nonuniform deformations in polycrystals and aspects of the validity of the taylor model. *J. Mech. Phys. Solids*, 37(2):191 – 232, 1989.

[4] C. A. Bronkhorst, S. R. Kalidindi, and L. Anand. Polycrystalline plasticity and the evolution of crystallographic texture in fcc metals. *Philos. Trans. R. Soc. Lond. A*, 341(1662):443–477, 1992.

[5] R. Becker and S. Panchanadeeswaran. Effects of grain interactions on deformation and local texture in polycrystals. *Acta Metall. Mater*, 43(7):2701–2719, 1995.

[6] A. J. Beaudoin, H. Mecking, and U. F. Kocks. Development of localized orientation gradients in fcc polycrystals. *Philos. Mag. A*, 73(6):1503–1517, 1996.

[7] G.B. Sarma, B. Radhakrishnan, and P.R. Dawson. Mesoscale modeling of microstructure and texture evolution during deformation processing of metals. *Adv. Eng. Mater.*, 4(7):509–514, 2002.

[8] Veera Sundararaghavan and Nicholas Zabaras. Design of microstructure-sensitive properties in elasto-viscoplastic polycrystals using multi-scale homogenization. *Int. J. Plast.*, 22(10):1799 – 1824, 2006.

[9] A. Clement. Prediction of deformation texture using a physical principle of conservation. *Mater. Sci. Eng.*, 55:203–210, 1982.

[10] G.I. Taylor. Plastic strain in metals. *J. Inst. Metals.*, 62:307–325, 1938.

[11] U.F. Kocks, C.N. Tomé, and H.R. Wenk. *Texture and anisotropy - Preferred orientations in polycrystals and their effect on materials properties*. Cambridge University Press., Cambridge, UK, 2000.

[12] Hans J Bunge and Peter R Morris. *Texture Analysis in Materials Science*. Butterworths, London, 1982.

[13] R. Armstrong, I Codd, R.M. Douthwaite, and N.J. Petch. The plastic deformation of polycrystalline aggregates. *Philos. Mag.*, 7:45–58, 1962.

[14] G.J. Weng. A micromechanical theory of grain–size dependence in metal plasticity. *J. Mech. Phys. Solids.*, 31(3):193–203, 1983.

[15] N. Nicaise, S. Berbenni, F. Wagner, M. Berveiller, and X. Lemoine. Coupled effects of grain size distributions and crystallographic textures on the plastic behaviour of IF steels. *Int. J. Plast.*, 27:232–249, 2011.

[16] B. Raeisinia, C.W. Sinclair, W.J. Poole, and C.N. Tom. On the impact of grain size distribution on the plastic behaviour of polycrystalline metals. *Modell. Simul. Mater. Sci. Eng.*, 16:1–15, 2008.

[17] J.Y. Shu and N.A. Fleck. Strain gradient crystal plasticity: size-dependent deformation of bicrystals. *J. Mech. Phys. Solids.*, 47:297–324, 1999.

[18] A. Acharya and A.J. Beaudoin. Grain-size effect in viscoplastic polycrystals at moderate strains. *J. Mech. Phys. Solids.*, 48:2213–2230, 2000.

[19] W.A. Counts, M.V. Braginsky, C.C. Battaile, and E.A. Holm. Predicting the Hall–Petch effect in fcc metals using non-local crystal plasticity. *Int. J. Plast.*, 24(7):1243–1263, 2008.

[20] L.P. Evers, W.A.M. Brekelmans, and M.G.D. Geers. Scale dependent crystal plasticity framework with dislocation density and grain boundary effects. *Int. J. Solids. Struct.*, 41:5209–5230, 2004.

[21] H.J. Bunge, F. Wagner, P.I. Welch, and P. van Houtte. A new way to include the grain shape in texture simulations with the Taylor model. *J. Phys. Lett.*, 46:1109–1113, 1985.

[22] F. Wagner, H.J. Bunge, and P. Van Houtte. Influence of grain size and shape on the texture formation and the anisotropy coefficient. In *Eighth international conference on textures of materials. Metall. Soc.*, pages 369–374, Warrendale, PA, 1988. Metallurgical Society.

[23] S. Tiem, M. Berveiller, and G.R. Canova. Grain shape effects on the slip system activity and on the lattice rotations. *Acta Metall.*, 34:2139–2149, 1986.

[24] B.S. Fromm, B.L. Adams, S. Ahmadi, and M. Knezevic. Grain size and orientation distributions: Application to yielding of a-titanium. *Acta Mater.*, 57:2339–2348, 2009.

[25] S.K. Chan, I.S. Tuba, and W.K. Wilson. On the finite element method in linear fracture mechanics. *Eng. Frac. Mech.*, 2(1):1 – 17, 1970.

[26] Timon Rabczuk. Computational methods for fracture in brittle and quasi-brittle solids: state-of-the-art review and future perspectives. *ISRN Applied Mathematics*, 2013, 2013.

[27] G.T. Camacho and M. Ortiz. Adaptive lagrangian modelling of ballistic penetration of metallic targets. *Comput. Methods Appl. Mech. Eng.*, 142:269–301, 1997.

[28] A. Needleman. An analysis of tensile decohesion along an interface. *J. Mech. Phys. Solids*, 38:289–324, 1990.

[29] A. Needleman. Micromechanical modeling of interfacial decohesion. *Ultramicroscopy*, 40:203–214, 1992.

[30] V. Tvergaard and J.W. Hutchinson. The influence of plasticity on mixed-mode interface toughness. *J. Mech. Phys. Solids*, 41:1119–1135, 1993.

[31] V. Tvergaard and J.W. Hutchinson. Effect of strain dependent cohesive zone model on predictions of crack growth resistance. *Int. J. Solids Struct.*, 33:3297–3308, 1996.

[32] K. Willam. Simulation issues of distributed and localized failure computations. In Mazars J.and Bazant Z.P., editor, *Cracking and Damage*, pages 363–378, New York, 1989. Elsevier.

[33] X.P. Xu and A. Needleman. Numerical simulations of fast crack growth in brittle solids. *J. Mech. Phys. Solids*, 42:1397–1434, 1994.

[34] M. Ortiz and A. Pandolfi. A class of cohesive elements for the simulation of three-dimensional crack propagation. *Int. J. Numer. Methods Eng.*, 44:1267–1282, 1999.

[35] P.D. Zavattieri and H.D. Espinosa. Grain level analysis of crack initiation and propagation in brittle materials. *Acta Mater.*, 49:4291–4311, 2001.

[36] Milan Jirásek. Comparative study on finite elements with embedded discontinuities. *Computer Methods in Applied Mechanics and Engineering*, 188(1-3):307 – 330, 2000.

[37] Nicolas Moës and Ted Belytschko. Extended finite element method for cohesive crack growth. *Engineering Fracture Mechanics*, 69(7):813 – 833, 2002.

[38] J. J. C. Remmers, R. de Borst, and A. Needleman. A cohesive segments method for the simulation of crack growth. *Computational Mechanics*, 31(1-2):69–77, 2003.

[39] Jeong-Hoon Song and Ted Belytschko. Cracking node method for dynamic fracture with finite elements. *International Journal for Numerical Methods in Engineering*, 77(3):360–385, 2009.

[40] F. Armero and K. Garikipati. An analysis of strong discontinuities in multiplicative finite strain plasticity and their relation with the numerical simulation of strain localization in solids. *Int. J. Solids Struct.*, 33(20 - 22):2863 – 2885, 1996.

[41] K. Garikipati and T.J.R. Hughes. A study of strain localization in a multiple scale framework–the one-dimensional problem. *Comput. Methods. Appl. Mech. Eng.*, 159(3–4):193–222, 1998.

[42] K. Garikipati. A variational multiscale method to embed micromechanical surface laws in the macromechanical continuum formulation. *Comput. Model. Eng. Sci.*, 3(2):175–184, 2002.

[43] S. Rudraraju, A. Salvi, K. Garikipati, and A.M. Waas. Predictions of crack propagation using a variational multiscale approach and its application to fracture in laminated fiber reinforced composites. *Composite Struct.*, 94(11):3336 – 3346, 2012.

[44] S.S. Rudraraju, A. Salvi, K. Garikipati, and A.M. Waas. In-plane fracture of laminated fiber reinforced composites with varying fracture resistance: Experimental observations and numerical crack propagation simulations. *Int. J. Solids. Struct.*, 47(7–8):901 – 911, 2010.

[45] S.V. Harren, H.E. Dve, and R.J. Asaro. Shear band formation in plane strain compression. *Acta Metall.*, 36(9):2435 – 2480, 1988.

[46] L. Anand and S.R. Kalidindi. The process of shear band formation in plane strain compression of fcc metals: Effects of crystallographic texture. *Mech. Mater.*, 17(2 - 3):223 – 243, 1994.

[47] J. Oliver. A consistent characteristic length for smeared cracking models. *Int. J. Num. Meth. Eng.*, 28(2):461–474, 1989.

[48] Esteban Samaniego and Ted Belytschko. Continuum discontinuum modelling of shear bands. *Int. J. Numer. Meth. Eng.*, 62(13):1857–1872, 2005.

[49] Z. Bazant, T. Belytschko, and T. Chang. Continuum theory for strainsoftening. *J. Eng. Mech*, 110(12):1666–1692, 1984.

[50] Susanta Ghosh, Abhishek Kumar, Veera Sundararaghavan, and Anthony M. Waas. Non-local modeling of epoxy using an atomistically-informed kernel. *International Journal of Solids and Structures*, 50(19):2837 – 2845, 2013.

[51] Susanta Ghosh, Veera Sundararaghavan, and Anthony M. Waas. Construction of multi-dimensional isotropic kernels for nonlocal elasticity based on phonon dispersion data. *International Journal of Solids and Structures*, 51(2):392 – 401, 2014.

[52] Veera Sundararaghavan and Anthony Waas. Non-local continuum modeling of carbon nanotubes: Physical interpretation of non-local kernels using atomistic simulations. *Journal of the Mechanics and Physics of Solids*, 59(6):1191 – 1203, 2011.

[53] Bernard D. Coleman and Marion L. Hodgdon. On shear bands in ductile materials. In *Analysis and Thermomechanics*, pages 227–255. Springer Berlin Heidelberg, 1987.

[54] S.A. Silling. Reformulation of elasticity theory for discontinuities and long-range forces. *J. Mech. Phys. Solids*, 48(1):175 – 209, 2000.

[55] S.A. Silling, M. Epton, O. Weckner, J. Xu, and E. Askari. Peridynamic states and constitutive modeling. *J. Elast.*, 88(2):151–184, 2007.

[56] Abigail Agwai, Ibrahim Guven, and Erdogan Madenci. Predicting crack propagation with peridynamics: a comparative study. *International Journal of Fracture*, 171(1):65–78, 2011.

[57] Thomas L. Warren, Stewart A. Silling, Abe Askari, Olaf Weckner, Michael A. Epton, and Jifeng Xu. A non-ordinary state-based peridynamic method to model solid material deformation and fracture. *Int. J. Solids Struct.*, 46(5):1186 – 1195, 2009.

[58] Shang Sun and Veera Sundararaghavan. A probabilistic crystal plasticity model for modeling grain shape effects based on slip geometry. *Acta Materialia*, 60(13–14):5233–5244, 2012.

[59] A. Kumar and P.R. Dawson. The simulation of texture evolution using finite elements over orientation space. I. Development. *Comput. Methods. App. Mech. Eng.*, 130:227–246, 1996.

[60] A. Kumar and P.R. Dawson. The simulation of texture evolution using finite elements over orientation space. II. Application to planar crystals. *Comput. Methods. App. Mech. Eng.*, 130:247–261, 1996.

[61] B.L. Adams, J.P. Boehler, M. Guidi, and E.T. Onat. Group theory and representation of microstructure and mechanical behavior of polycrystals. *J. Mech. Phys. Solids.*, 40:723–737, 1992.

[62] S.R. Kalidindi and H.K. Duvvuru. Spectral methods for capturing crystallographic texture evolution during large plastic strains in metals. *Acta Mater.*, 53(13):3613–3623, 2005.

[63] G.F. Vander Voort. *Metallography: principles and practice*. McGraw–Hill Book Company, New York, 1984.

[64] R.J. Asaro and A. Needleman. Texture development and strain hardening in rate dependent polycrystals. *Acta Mater.*, 33:923–953, 1985.

[65] O.C. Zienkiewicz and J.Z. Zhu. A simple error estimator and adaptive procedure for practical engineering analysis. *Int. J. Num. Meth. .Eng.*, 24(2):337–357, 1987.

[66] Veera Sundararaghavan and Nicholas Zabaras. A multi-length scale sensitivity analysis for the control of texture-dependent properties in deformation processing. *Int. J. Plast.*, 24(9):1581 – 1605, 2008.

[67] B. Gross, J.E. Srawley, and W.F. Brown. Stress-intensity factors for a single-edge-notch tension specimen by boundary collocation of a stress function. Technical report, NASA, 1964.

[68] Shang Sun and Veera Sundararaghavan. Modeling crack propagation in polycrystalline alloys using variational multiscale cohesive method. *Computational Mechanics, in review*, 2014.

[69] Shiva Rudraraju, Amit Salvi, Krishna Garikipati, and Anthony M. Waas. Predictions of crack propagation using a variational multiscale approach and its application to fracture in laminated fiber reinforced composites. *Composite Structures*, 94(11):3336 – 3346, 2012.

[70] A finite element analysis of quasistatic crack growth in a pressure sensitive constrained ductile layer. *Engineering Fracture Mechanics*, 66(6):551 – 571, 2000.

[71] S.Roy Chowdhury and R. Narasimhan. A cohesive finite element formulation for modelling fracture and delamination in solids. *Sadhana*, 25(6):561–587, 2000.

[72] L. Anand and M. Kothari. A computational procedure for rate-independent crystal plasticity. *Journal of the Mechanics and Physics of Solids*, 44(4):525 – 558, 1996.

[73] F. Dunne, L. Fielding, R. Allen, and A. Manonukul. Experimental and computational polycrystal studies of fatigue damage and crack initiation. In *proceedings of the XIth international conference on fracture*, Turin, Italy, March 2005.

[74] Shang Sun and Veera Sundararaghavan. A peristatic implementation of crystal plasticity. *International Journal of Solids and Structures, in reivew*, 2014.

[75] E. Ising. Beitrag zur theorie des ferromagnetismus. *Zeitschrift Physik*, 31:253–258, 1925.

[76] Olga Dmitrieva, Patrick W. Dondl, Stefan Mller, and Dierk Raabe. Lamination microstructure in shear deformed copper single crystals. *Acta Materialia*, 57(12):3439 – 3449, 2009.

[77] Rongtao Zhu, Jianqiu Zhou, Hua Jiang, and Dongsheng Zhang. Evolution of shear banding in fully dense nanocrystalline ni sheet. *Mechanics of Materials*, 51(0):29 – 42, 2012.

[78] John Allison, Dan Backman, and Leo Christodoulou. Integrated computational materials engineering: A new paradigm for the global materials profession. *J. Minerals. Metals. Mater. Soc.*, 58(11):25–27, 2006.

[79] Spandan Maiti and Philippe H. Geubelle. A cohesive model for fatigue failure of polymers. *Engineering Fracture Mechanics*, 72(5):691 – 708, 2005.

[80] Youn Doh Ha and Florin Bobaru. Studies of dynamic crack propagation and crack branching with peridynamics. *International Journal of Fracture*, 162(1-2):229–244, 2010.

[81] David John Littlewood, Kyran D Mish, and Kendall H Pierson. Quasi-statics modal analysis and structural health monitoring within the peridynamic framework. Technical report, Sandia National Laboratories, 2012.